Imperial College London

Imperial College London
Department of Mechanical Engineering

Simulation and Feedback Control of Simplified Vehicle Flows

Olga Evstafyeva

Submitted for the degree of Doctor of Philosophy

Statement of Originality

I hereby declare that the research presented in this thesis is my own, except where otherwise stated in the text. The results reported in this thesis have been presented at several conferences and published in the Rapids section of Journal of Fluid Mechanics [31]. The copyright of this thesis rests with the author and is made available under a Creative Commons Attribution Non-Commercial No Derivatives licence. Researchers are free to copy, distribute or transmit the thesis on the condition that they attribute it, that they do not use it for commercial purposes and that they do not alter, transform or build upon it. For any reuse or redistribution, researchers must make clear to others the licence terms of this work.

Publications

Evstafyeva O., Morgans A. & Dalla Longa L. 2017 Simulation and feedback control of the Ahmed body flow exhibiting symmetry breaking behaviour. *Journal of Fluid Mechanics.* **817**, R2

Conferences and Workshops

68th American Physical Society's Division of Fluid Dynamics Meeting in Boston, MA, USA 2015

AEROVEHICLES 2 in Götenburg, Sweden 2015

ERCOFTAC Montestigliano Spring School on Reduced-order models for non-linear dynamics in fluid flows, Italy, 2016

UK Fluids Conference, Imperial College London, UK, 2016

69th American Physical Society's Division of Fluid Dynamics Meeting, Portland OR, USA, 2016

52nd 3AF International Applied Aerodynamics Conference - Progress in Flow Control, Lyon, France, 2017

UK Fluids Conference, University of Leeds, UK, 2017

Acknowledgements

I would like to express my profound gratitude to my supervisor - Professor Aimee Morgans, for her patient guidance, support and encouragement over the past four years. I have been extremely lucky to have a supervisor who cared so much about my work, helped me find funding and gave me so many opportunities. All of this has made this PhD a truly exciting learning experience. I am also thankful to Professor Sergei Chernyshenko, for his advice when I was searching for a doctoral placement and help with finding the right project.

I would also like to formally thank the UK Engineering and Physical Sciences Research Council for financial support. This project would also not have been possible without access to the UK National Supercomputing Service ARCHER and Imperial College HPC clusters. I would also like to acknowledge the support from the UK Turbulence Consortium in the form of last-minute computational resources.

Thank you also to all of my Imperial friends for all the fun times we shared. Among some of the highlights from the past four years are: wondering why my disk tray comes out whenever I open my terminal, the Italian karaoke and brunch the next day, existential conversations in New York taxis, locking down the MJ Thriller moves and taking badminton and foosball a little bit too seriously. Thanks, guys, for making last four years so memorable.

И конечно же огромное спасибо моим родителями, Аркадию и Ирине, которым я обязана всем! Мне невероятно повезло - всю жизнь меня окружала забота моих родителей, которые всегда меня поддерживали и создавали благо-

приятные условия для всех моих затей! Мне с вами - море по колено.

Вообще, когда я задумываюсь, какие именно обстоятельства привели меня к данному моменту, я понимаю насколько много вдохновения я постоянно получаю от всей моей разнообразной семьи. Спасибо моим сестрам Лене и Томе, за поддержку вдали от дома и за то, что постоянно держат меня в тонусе своими шуточками и неожиданными вопросами. Спасибо дедушке Юре за то, что развивал мою фантазию умными сказками и стихами. Спасибо бабушке Наташе, за то что с детства приучала думать критически с помощью стратегических игр в "дурака". Спасибо дедушке Славе, за то что с детства учил меня арифметики, через игру "21". Спасибо бабушке Тамаре, за то что развивала мое любопытство, обучая меня о растениях. Спасибо Наде, моей двоюродной сестре, за наше совместное детство и приключения в деревне. И спасибо Дяде Мише, за то что когда я приезжаю в Саратов он меня всегда встречает по-русски!

And to my husband Alexander Bate - thank you for always encouraging me to do new things, for challenging me to be better and do better and never letting me give up. Last four years have been made much easier by your unwavering support, encouragement and occasional enforcement of life-work balance. Thank you for accompanying me on this journey and I look forward to our next one.

Abstract

The present doctoral work investigates wake flow behind a square-back Ahmed body at laminar and turbulent Reynolds numbers. At low Reynolds numbers the Ahmed body wake undergoes a series of bifurcations towards symmetry breaking state. Using Large Eddy Simulations, which resolve the boundary layer down to the wall, the sequence of symmetry breaking bifurcations is captured numerically for the first time. Large Eddy Simulations are then used to investigate the reflectional symmetry breaking behaviour in the turbulent regime, where it manifests as slow and random bi-modal switching between the asymmetric states. The bi-modal switch from one state to the other is captured for the first time numerically, allowing to study the effects of wake displacement on the instantaneous wake structures.

A linear feedback control strategy, designed to attenuate base pressure force fluctuations is tested on the Ahmed body flow. At low Reynolds numbers the strategy is successful; a moderate base pressure recovery and a concomitant drag reduction are achieved and the wake is re-symmetrised. A similar control approach is also benchmarked at higher Reynolds numbers, where the flow exhibits turbulent separation. The preliminary results suggest that the controller is unlikely to reduce drag and other actuation/sensing arrangements need to be investigated. This work motivates future attempts to develop a linear feedback controller based on the strategy described herein, but with better selected actuation and sensing. Further work is also required to better understand the physical mechanism behind bi-modal switching in the wake.

Contents

1 Introduction **23**

1.1 Motivation 23

1.2 The Ahmed body flow 25

1.2.1 Averaged and Dynamic Flow Features 27

1.2.2 Recent Findings on the Instantaneous Flow 30

1.2.3 Real-life Vehicles 33

1.3 Flow Control 35

1.3.1 Passive Control 35

1.3.2 Active Open-Loop Control 36

1.3.3 Active Closed-Loop Control 37

1.4 Final Remarks 42

2 Numerical Methods **44**

2.1 Large Eddy Simulations 46

2.1.1 Governing LES Equations 46

2.1.2 Subgrid-Scale Modelling 47

2.1.3 LES Solver 48

2.2 Pre-Processing 54

2.3 Control Strategy 56

2.4 Modal analysis . . . 62
2.4.1 Proper Orthogonal Decomposition . . . 62
2.4.2 Dynamic Mode Decomposition . . . 65

3 Laminar Ahmed Body Flow 68

3.1 The Test-Case . . . 70
3.2 Unforced Flow . . . 74
3.2.1 Topologies of the Laminar Wake . . . 74
3.2.2 Dynamics of the Laminar Wake . . . 78
3.2.3 Ground Effects . . . 81
3.3 Open-Loop Forcing . . . 86
3.3.1 Effects of the Open-Loop Forcing . . . 89
3.3.2 System identification . . . 91
3.4 Feedback Control . . . 92
3.4.1 Wake Mode Analysis . . . 96
3.5 Final Remarks . . . 99

4 Turbulent Ahmed Body Flow 101

4.1 The test-case . . . 102
4.1.1 Computational Domain . . . 102
4.1.2 Computational Mesh . . . 105
4.2 Unforced Flow . . . 108
4.2.1 Time-Averaged flow . . . 109
4.2.2 Instantaneous flow . . . 109
4.2.3 Modal Analysis . . . 112
4.2.4 Dynamic Mode Decomposition of the Turbulent Ahmed Body Wake . . . 112

4.2.5 Proper Orthogonal Decomposition of the Turbulent Ahmed Body Wake 116
4.3 Open Loop Forcing 119
4.3.1 Effects of the Open-Loop Forcing 119
4.4 Final Remarks 123

5 Conclusion **124**
5.1 Outlook 127

Bibliography **128**

A Linear Transfinite Interpolation **143**

List of Tables

3.1 Grid comparison for simulations at $Re_H = 435$ 71

3.2 Drag and lift coefficients at different symmetry-breaking states 78

3.3 Drag and lift coefficients in simulations with no ground and moving ground, compared to the nominal test case with stationary ground (in bold). 86

3.4 Momentum coefficients reported in other studies using active flow control on blunt bluff bodies All these studies actuated the flow using synthetic jets angled at 45° degrees to the downstream flow. 89

3.5 Dominant frequencies St_H of the base pressure signal spectrum from the simulations with open-loop forcing at amplitude $A_j = 0.1$ and forcing frequencies St_f ranging between $0.04 \leq St_f \leq 0.5$ 90

4.1 Grid comparison for simulations at $Re_H = 33,000$. 105

4.2 Grid comparison for simulations at $Re_H = 25,000$. 106

List of Figures

1.1 a) Greenhouse gas emissions by sector for 2015 b) change in GHG by sector from 2014 to 2015 [86]. 24

1.2 Schematic of the Ahmed body as introduced by Ahmed et. al. [2] . . 27

1.3 Wake topology as reported by *a)* Roumeas et. al. [101] and *b)* Krajnovic et. al. [62]. The authors both reported on the existence of the time-averaged vortex-ring of a turbulent wake, recirculation region in the near wake and large counter-rotating vortices in the far wake. . . 28

1.4 Domains of the instabilities measured from the experiments (a) and predicted by the model (b) as reported by Grandemange et. al. The yellow star shows where the conventional Ahmed Body would be on the diagram. [45]. 29

1.5 Open-loop control schematic 36

1.6 Closed-loop control schematic. 37

2.1 Data structure requirement for the grid blocks. 53

2.2 Generation of the rounded nose surface, where red (R) and blue (B) surfaces are used to generate the curved purple (P) surface using the relation $\frac{B+R}{2} = P$ 54

2.3 Generation of the rounded nose surface. *a)* red lines show the surface onto which the edges of the initial curved surface are projected. *b)* resulting mesh with emphasis on the discretisation of the corner. . . . 55

2.4 Structure of the mesh, where green area is populated using linear transfinite interpolation from the orange boundary towards the inlet and blue area is populated using an O-grid algorithm. 57

2.5 Dynamically linear model for feedback control: s denotes Laplace transform variable. 58

2.6 Sensor and actuation arrangement for blunt bluff body feedback control as implemented by *a)* Dahan. et. al [23] with the sensor measuring the pressure integrated over the base (dark blue) and two separate actuation locations U_{j_1} and U_{j_2}, *b)* Dalla Longa et.al. [24] with anti-symmetric sensor measurement of base pressure (light and dark blue) and out-of-phase forcing at the separation edges, and *c)* Flinois [34] with sensor measuring the pressure integrated over the base (dark blue) and uniform forcing along the separation edges. In all graphs the red arrows indicate the position and directions of the oscillating jets. 61

3.1 Flow visualizations at the Reynolds numbers *a)* $Re_H = 310$, *b)* and *c)* $Re_H = 365$, and *d)* $Re_H = 415$ from the experimental study by Grandemange et. al. [44]. For each Reynolds number: Top picture, top view; bottom picture, side view; right picture, rear view. The flow comes from the left for both top and side views. 69

3.2 Schematic of square-back Ahmed body: (a) side view ; (b) rear view. For this test case $H^* = \frac{H}{W} = 0.73$ and $C^* = \frac{C}{W} = 0.44$. 71

3.3 Regions of bi-modality (defined by the pressure gradient) as a function of ground clearance $C^* = \frac{H}{W}$ and aspect ratio $H^* = \frac{H}{W}$. The yellow star indicates the behaviour expected to be observed for the current test-case. 72

3.4 Structured grid used in the computations. Left: Grid in the vicinity of the nose (red) and around the body (blue). Right: horizontal and vertical slices through the domain, showing every 4^{th} node. 72

3.5 y^+ along the centerline of the south and north sides of the Ahmed body 73

3.6 Bifurcation scenario of changes in the mean position of the wake in the z-direction (Z_w) as the Reynolds number is varied between $310 \leq Re_H \leq 435$. LES results (red circles) are compared to experimental results from [44] (blue crosses). Black and grey lines show steady and unsteady regimes respectively. Z_w was measured as the point where the averaged streamlines met in the far wake to create a trail. 74

3.7 Visualisations of Ahmed Body flow at Reynolds numbers (a) $Re_H = 310$, (b) and (c) $Re_H = 415$, (d) $Re_H = 435$. For each Re_H the top and bottom left pictures show side view and top view respectively of a 2D slice with streamlines projected onto it; the right picture shows 3D streamlines in the wake. 75

3.8 Q-criterion iso-contour of Ahmed Body flow at Reynolds number $Re_H = 435$ when the wake is (a) unsteady symmetric wake, (b) unsteady asymmetric wake, where the asymmetry is locked to one preferred position, no switch between the two asymmetric states was observed. For each regime, the top and bottom left pictures show side view and top view respectively; the right picture shows the diagonal view from the top. The same positive Q-criterion iso-contour is plotted with opaque and transparent parts to reveal the internal structure of the vortex ring in the wake. 78

3.9 Amplitude of base pressure force spectrum for the Ahmed body flow at *a)* $Re_H = 310$ - steady symmetric wake, *b)* $Re_H = 415$ - unsteady symmetric wake, *c)* $Re_H = 415$ - steady asymmetric wake, and *d)* $Re_H = 435$ - unsteady asymmetric wake. 79

3.10 The a) horizontal and *b)* vertical pressure gradients: $\frac{\partial C_p}{\partial z}$ and $\frac{\partial C_p}{\partial y}$ respectively, are computed by recording separate base pressure signals averaged over blue and red regions and computing their difference. . . 80

3.11 Right: Base pressure gradients for the Ahmed body flow at $Re_H = 435$. Left: Probability Density of the base pressure gradient signal. . . 80

3.12 Results from simulations of Ahmed body flow at $Re_H = 310$ with no ground. *a)* Horizontal (top) and vertical (bottom) 2D slices through the instantaneous velocity flow field recorded at $T^* = 588$ with streamlines projected onto the slice. *b)* Horizontal (top) and vertical (bottom) base pressure gradient 82

3.13 Results from simulations of Ahmed body flow at $Re_H = 435$ with no ground. *a)* Vertical (left) and horizontal (right) base pressure gradients. *b)* two-dimensional slices (top - horizontal; bottom - vertical) through the velocity flow field recorded at $T^* = 300$ and $T^* = 685$ with streamlines projected onto the slices. 83

3.14 Normalised base pressure force signal from simulations with stationary floor and moving floor. 84

3.15 Results from simulations of Ahmed body flow at $Re_H = 435$ with moving ground. *a)* Two-dimensional slices (top - horizontal; bottom - vertical) through the velocity flow field recorded at $T^* = 729$ with streamlines projected onto the slices. *b)* corresponding base pressure gradients. 85

3.16 iso-surface contour at $u = 0$ visualising the recirculation regions when the ground is stationary (red) and when the ground is moving (opaque grey). 85

3.17 Amplitude force spectrum of the base pressure signal of the Ahmed body flow at $Re_H = 435$ clearly revealing key frequencies at $St_H \approx 0.09$ and $St_H \approx 0.18$, matching those in the literature as per chapter 1.2.1. 87

3.18 Schematic of the control arrangement: sensor (light blue) measures the base pressure force and actuation (red) acts via synthetic jets angled at 10° away from the body pointing downstream. 87

3.19 Effect of harmonic open-loop forcing at $A_j = 0.1$ and different forcing frequencies St_f on *a)* the time-averaged base pressure coefficient and *b)* the RMS value of the base pressure fluctuations. The dashed line represents the unforced value. 88

3.20 Base pressure spectra of the flow actuated at frequencies *a)* $St_f = 0.06$ and *b)* $St_f = 0.1$. 89

3.21 Instantaneous snapshots of the flow actuated at $St_f = 0.06$, $A_j = 0.1$: *a)* vertical slice, *b)* horizontal slice. Snapshots were taken at equal intervals over one cycle. 90

3.22 Instantaneous snapshots of the flow actuated at $St_f = 0.08$, $A_j = 0.1$: *a)* vertical slice, *b)* horizontal slice. Snapshots were taken at equal intervals over one cycle. 91

3.23 Instantaneous snapshots of the unforced flow. *a)* vertical slice, *b)* horizontal slice. Snapshots were taken at equal intervals over one cycle. 92

3.24 System identification data of frequency response gain and phase from open-loop simulations at $A_j = 0.1$ and $A_j = 0.2$. 93

3.25 Frequency response gain and phase for the controller $K(s)$ and sensitivity function $S(s)$. 94

3.26 a) Comparison of converged base pressure coefficient, C_p, with (red) and without (black) feedback control. b) Corresponding actuation signal, U_{jet} 94

3.27 Base pressure signal spectrum for the Ahmed body flow at $Re_H = 435$ with and without feedback control. 95

3.28 Horizontal 2D slice coloured by velocity magnitude with streamlines projected onto it (left) and vertical 2D slice coloured by pressure (right) of the *a)* unforced and *b)* controlled instantaneous flow fields . 96

3.29 Q-criterion iso-contour of Ahmed Body flow at Reynolds number $Re_H = 435$ *a)* without and *b)* with feedback control. The top and bottom left pictures show top view and side view respectively; the right picture shows the diagonal view from the top. The same Q-criterion iso-contour is plotted with opaque and transparent parts to reveal the internal structure of the vortex ring in the wake. 97

3.30 *a)* Comparison of the base pressure coefficient, C_p, with and without feedback control implemented to the case with moving ground. *b)* Corresponding actuation signal U_{jet}. 97

3.31 DMD results for *(a)* the unforced flow and *(b)* the flow with feedback control. The top figure shows the frequencies and growth rates of the DMD modes scaled by their optimum amplitudes; bottom figure is a top-view of the spatial structure of the most dynamically represented modes (red markers on the frequency vs. growth rate figure) at *(a)* $St_H = 0.16$ for unforced flow and *(b)* $St_H = 0.13$ for the flow with feedback control. 98

4.1 Schematic of square-back Ahmed body: (a) side view ; (b) rear view. 102

4.2 Flow characteristics sampled before separation (arrow) along the horizontal centerline of the north boundary of the Ahmed body. LES data is compared to DNS channel flow data (at $Re_\theta = 1551$) from Jimenez et al. [57] (solid lines). *a)* the mean streamwise velocity profile, *b)* the root-mean-square turbulent fluctuations and Reynolds stress and *c)* sampling location. 103

4.3 *a)* Re_θ and *b)* shape factor $H = \delta^*/\theta$ along the top surface of the Ahmed body at $Re_H = 25,000$. 104

4.4 Structured grid used in the simulations of the Ahmed Body flow at Reynolds number $Re_H = 30,000$. Left: Grid in the vicinity of the body nose and discretisation around the body. Right: horizontal and vertical slices showing every 4^{th} node of the grid. 105

4.5 Regions of bi-modality as a function of ground clearance and aspect ratio. The yellow star indicates the behaviour expected to be observed for the current test-case. 106

4.6 y^+ along the centerline of the south boundary of the Ahmed body at *a)* $Re_H = 33,000$ and *(b)* $Re_H = 25,000$. 107

4.7 y^+ contours at $Re_H = 33,000$. 107

4.8 Time-averaged vortex-ring of a turbulent wake at $C_p = -0.22$ with streamlines projected onto two dimensional slices to reveal recirculation region in the near wake and large counter-rotating vortices in the far wake. 109

4.9 Time-averaged horizontal (top) and vertical (bottom) 2D slices of the wake coloured by velocity magnitude with streamlines projected onto them. 110

4.10 Base pressure gradient signal in vertical (top) and horizontal (bottom) directions 111

4.11 Instantaneous three-dimensional wake topology as proposed by *a)* Evrard et. al. [30] and *b)* Perry et. al. [93]. 111

4.12 Evolution of the position of the instantaneous vortex ring when the wake is tilted *a)* and *c)* and the wake during the flip between the two positions *b)*. The vortex visualised using pressure contours at $Cp = -0.21$ coloured by velocity in the streamwise direction 113

4.13 Horseshoe structures shed from the longest part of the wake visualised as pressure contours at $Cp = -0.16$ coloured by velocity in the streamwise direction. 113

4.14 DMD modes plotted by their growth rates and frequencies and scaled by the amplitudes. The modes at $St_H \approx 0.08$ and $St_H \approx 0.2$ are highlighted in blue. *a)* DMD modes before the flip and *b)* DMD modes after the flip. 114

4.15 2D slices (top - horizontal slice, bottom - vertical slice) of the DMD mode at $St \approx 0.08$ corresponding to bubble pumping mode *a)* when the wake is shifted to the left and *b)* after the flip when the wake is shifted to the right. 114

4.16 3D iso-contours of the DMD mode at $St \approx 0.08$ corresponding to bubble pumping mode*a)* when the wake is shifted to the left and *b)* after the flip when the wake is shifted to the right. 115

4.17 2D slices (top - horizontal slice, bottom - vertical slice) through the DMD mode at $St \approx 0.2$ corresponding to shedding mode *a)* when the wake is shifted to the left and *b)* after the flip when the wake is shifted.116

4.18 3D iso-contours of the DMD mode at $St \approx 0.2$ corresponding to shedding mode *a)* when the wake is shifted to the left and *b)* after the flip when the wake is shifted. 116

4.19 *a)* The energy of the extracted POD modes for two datasets: top - wake on the left, bottom - wake on the right. *b)* 3D iso contour (above 0) of the first and most energetic mode for the two datasets: top - wake on the left, bottom - wake on the right. 117

4.20 The next three POD modes were derived from two datasets: top - iso-contours of the POD modes when the wake on the left, bottom - iso-contours of the POD modes when wake on the right. 118

4.21 Base pressure force signal over the duration of the simulation (top) and the corresponding base pressure force spectrum (bottom). The base pressure force spectrum was computed using both fft (black) and *pwelch* (red) Matlab commands show the rich wake dynamics at the low frequencies and extract the main peaks. 120

4.22 Changes in *a)* mean base pressure and *b)* root-mean square of fluctuations about the mean of base pressure signal in response to open-loop forcing at different frequencies and amplitude $A_j = 0.1$. The black line represents the value recorded in the unforced simulations and the blue and red dotted lines represent the values recorded in simulations with open-loop forcing. 121

4.23 Changes in the mean base pressure in response to open-loop forcing via synthetic jets *a)* for a three-dimensional backward-facing step by Dahan et. al. [23] and *b)* for a three-dimensional backward-facing step with side walls by Flinois [34]. In *a)* the change in mean base pressure due to forcing along the separation line is shown for amplitudes $A_j = 0.1$ (●), $A_j = 2$ (▲) and $A_j = 0.3$ (◆) and due forcing at the base of the backward-facing step at amplitude $A_j = 0.2$ (▼). In *b)* the mean base pressure is shown at every forcing frequency compared to the mean value indicated by the dotted line. 122

Nomenclature

δ_{ij}	Kroneker delta
$\frac{\partial C_p}{\partial y}$	Pressure gradient in vertical direction
$\frac{\partial C_p}{\partial z}$	Pressure gradient in horizontal direction
$\mathbf{\Phi}$	Proper Orthogonal Decomposition modes
$\mathbf{u} = (u, v, w)$	Velocity vector and its components in $x-, y-$ and $z-$ directions
$\mathbf{V}_1^M$	Snapshot matrix
ν_t	Turbulent viscosity
$\overline{S}_{ij}$	Strain rate tensor
ϕ	Slant angle at the rear of the Ahmed body
ρ	Air density
τ_{ij}	Subgrid scale tensor
A_j	Forcing amplitude of actuation
C	Ahmed body ground clearance
C^*	Ahmed body ground clearance ratio $C^* = \frac{C}{W}$
c_μ	Momentum coefficient

C_D Drag coefficient

C_l Lift coefficient

C_p Pressure coefficient

DMD Dynamic Mode Decomposition

DNS Direct Numerical Simulations

$F_b(s)$ Base pressure force signal

$G(s)$ Plant transfer function

H Ahmed body height

H^* Ahmed body aspect ratio $H^* = \frac{H}{W}$

$K(s)$ Feedback controller

L Ahmed body length

LES Large Eddy Simulations

$N(s)$ Natural flow disturbances

p Pressure

POD Proper Orthogonal Decomposition

$RANS$ Reynolds-Averaged Navier-Stokes

Re Reynolds number

Re_Θ Reynolds number based momentum thickness

Re_H Reynolds number based on height

rms root mean square

s Laplace transform

$S(s)$ Sensitivity function

St_f Forcing frequency of actuation

St_H Strouhal number based on height

SVD Singular Value Decomposition

TFI Transfinite Interpolation

U_∞ Free stream velocity

$U_j(s)$ Actuation

$URANS$ Unsteady Reynolds-Averaged Navier-Stokes

W Ahmed body width

x, y, z Cartesian coordinates

Z_w Mean position of the wake in the z-direction

Chapter 1

Introduction

1.1 Motivation

This doctoral project is motivated by an increasing need for novel solutions that can help reduce the greenhouse gas (GHG) output of the transport sector. According to the latest available data, ground transport accounts for roughly 22% of the overall GHG emissions in the UK and remains the only major sector whose GHG emissions are still growing [86] (figure 1.1).

Cars produce GHG emissions when they burn fuel to overcome driving resistance. The main component of the overall driving resistance at motorway speeds is the aerodynamic drag. It has been estimated that at motorway speeds a 20% reduction in vehicle drag coefficient can achieve up to 6% fuel saving for large trucks and 10% for small vans [41, 29]. For square-back vehicles, the largest share of the aerodynamic drag originates at the rear of the vehicle: as the boundary layer separates over the rear edges, a complex low-pressure wake is created. The resulting pressure difference between the front and the rear of the vehicle creates the force called form-drag, which at motorway speeds has been estimated to constitute upwards of 69% of the overall aerodynamic drag [62, 117]. The large region of three-dimensional vortex separation at the rear is also an important low-frequency wind noise source

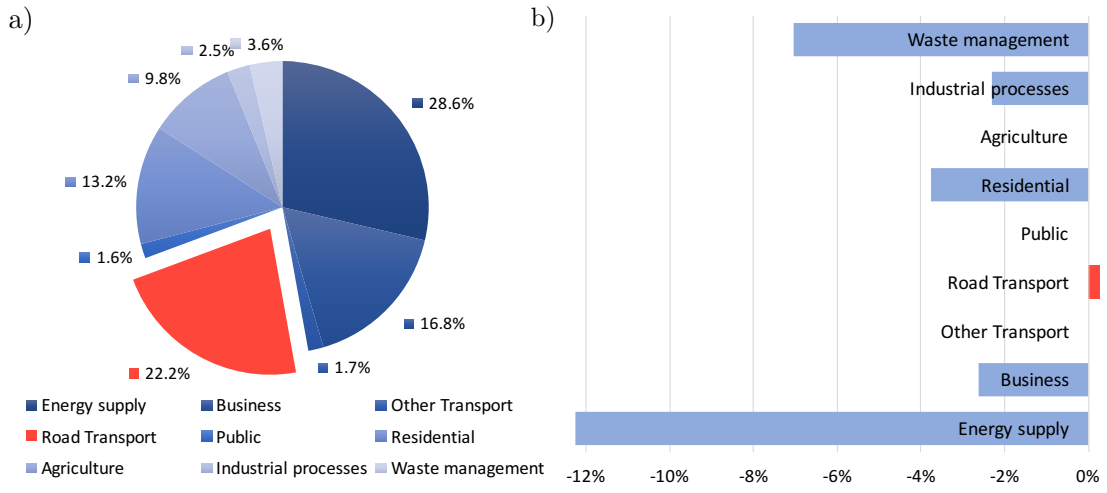


Figure 1.1: a) Greenhouse gas emissions by sector for 2015 b) change in GHG by sector from 2014 to 2015 [86].

that can significantly affect the passengers inside the vehicle [39]. Therefore reducing vehicle form-drag offers potential for significant GHG emissions savings and overall improvement of comfort. While the low drag requirement has now become one of the essential parts of vehicle design process [79], style, usability and safety are still prioritised above all else. This has created a need for solutions that improve aerodynamic efficiency without introducing prohibitive geometry changes or design features which could impede user experience.

In this doctoral work we aim to investigate further the flow past a square-back vehicle and present a practical feedback control strategy for reducing form-drag. The study is conducted numerically using Large Eddy Simulations to compute the flow past an Ahmed body - a simplified yet representative geometry for modelling vehicle flows introduced in 1984 by Ahmed et. al. [2]. The thesis first considers the flow at laminar Reynolds numbers based on height $310 \geq Re_H \geq 435$, where the onset of unsteadiness and development of symmetry breaking behaviour of the wake is analysed. Access to the full three-dimensional flow field, available through the numerical simulations, facilitates further insight into the Ahmed body wake topology, fundamental to identifying the main sources of drag and informing drag-reduction strategies.

Then a control strategy is developed with the aim of achieving a form-drag reduction. The implementation of feedback control is achieved via body mounted pressure sensors and energy-efficient Zero-Net-Mass-Flux synthetic jets. This set up requires minimal geometrical modifications and can be replicated in real-life environment. After studying the flow at laminar Reynolds numbers, the Large Eddy Simulations are used to compute Ahmed body flow at conditions for which the separating boundary layer is turbulent, notably $Re_H = 25,000$ and $Re_H = 33,000$. In particular, the simulations resolve down to the wall of the Ahmed body rather than employing wall models, with a view to capturing the bi-modal switching between states of broken symmetry (thought to be associated with increased drag) that have been observed experimentally [44, 45, 46, 63, 12], but not previously captured in simulations. We then investigate the effect of open loop forcing on the flow at $Re_H = 25,000$ using the same actuation/sensing arrangements as at laminar Reynolds numbers. This is with a view to future investigation of feedback control at turbulent Reynolds numbers. However, upon analyzing the flow response to open-loop forcing, it is concluded that a feedback controller based on current actuation/sensing shape is unlikely to achieve significant drag reduction. Constraints in computational resources mean that a more extensive investigation into actuation/sensing arrangements more likely to yield successful drag reduction is deferred for future study.

The next section now proceeds to overview the literature on flow dynamics about the Ahmed body, followed by a brief summary of flow control techniques, especially those relevant to blunt bluff body flows.

1.2 The Ahmed body flow

The Ahmed body, shown in figure 1.2, has been used as benchmark test case in vehicle aerodynamics modelling since its inception by Ahmed et. al. [2] in 1984. The authors were first to show that the rear angle ϕ of the vehicle can significantly affect

the dynamics in the wake. When the rear angle is $\phi < 10°$ or $\phi > 30°$, representing more blunt geometries, the topology of the after-body wake is characterised by a massive recirculation region. While for moderately slanted angles - between $10° < \phi < 30°$, the wake exhibits a pair of intense counter-rotating vortices that drastically reduce the pressure on the base. In the worst drag configuration (slant angle of $\phi \approx 30°$), these large structures increase the drag by up to 50% in comparison to the $\phi = 0°$ case. The drag-reduction control strategies need to vary accordingly; while the unifying goal is to recover base pressure deficit, the means of achieving that objective vary with ϕ. From the flow control point of view the slanted-back geometries can benefit from any control strategy that affects the formation of the streamwise counter-rotating vortices or reduces the amount of separated flow on the slanted face without amplifying the counter-rotating vortices (separation delay). The flow past a blunt Ahmed body case with $\phi = 0°$ is quite different. Unlike the geometries with a slanted angle, the wake of a square-back Ahmed body does not exhibit the intense streamwise vortices, but instead consists of interacting shear layers shedding from the blunt rear edges and creating a large recirculation region. The shear layers extend downstream until they meet at the stagnation point to form a low pressure envelope. As a result, the control strategies that achieved base pressure recovery of blunt Ahmed body flow were accompanied by quite different changes to the flow behaviour: either the bluntness of the geometry was modified, the recirculation length (distance between the stagnation point and the center of the base) increased or the statistical symmetry of the wake recovered. Since this project focuses on the square-back configuration, the dynamics past the blunt Ahmed body at $\phi = 0°$ will now be reviewed in further detail.

The Ahmed body geometry with the rear angle of $\phi = 0°$ has been extensively investigated over the past decade and there is good agreement within the academic community on averaged flow features and characteristic frequencies of the wake. However the instantaneous flow-field make-up, spatial organization of the

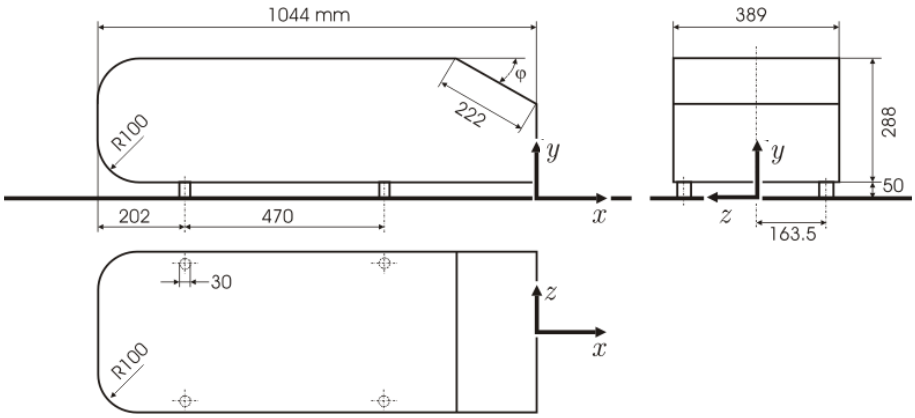


Figure 1.2: Schematic of the Ahmed body as introduced by Ahmed et. al. [2]

wake structures and their interaction remain open questions. One of the key breakthroughs in the field were the recent experimental investigations by Grandemange et. al. [44, 45, 46, 43], who conducted a detailed study into the reflectional symmetry breaking regimes of the Ahmed body wake. To explain how the understanding of the Ahmed body flow evolved we first review the well-understood averaged wake structures and wake frequencies, and then proceed to outline the more recent developments in the understanding of the instantaneous behaviour of the flow.

1.2.1 Averaged and Dynamic Flow Features

As mentioned previously the time-averaged properties of the turbulent Ahmed body flow are quite well-understood. Overall, the near-wake averages in time to a symmetric vortex ring [2, 28, 48, 62, 82, 101] as can be seen in figure 1.3. In the horizontal plane of symmetry the vortex ring corresponds to a pair of counter-rotating vortices which roll up and form a separation bubble - these can also be observed in figure 1.3 *a)* in the streamlines projected onto a two-dimensional slice immediately perpendicular to the body base. The upper structure is noticeably larger than the lower one as a consequence of the ground suppressing the amount of fluid entering the lower vortex, referred to as the ground effect.

Further downstream the wake is instantaneously composed of many unsteady

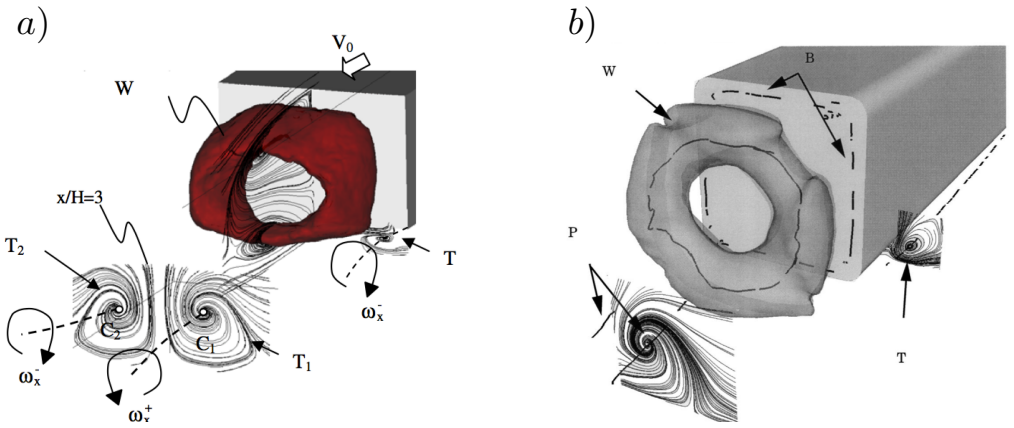


Figure 1.3: Wake topology as reported by *a)* Roumeas et. al. [101] and *b)* Krajnovic et. al. [62]. The authors both reported on the existence of the time-averaged vortex-ring of a turbulent wake, recirculation region in the near wake and large counter-rotating vortices in the far wake.

vortices, random in time and space. These structures average in time to a pair of longitudinal vortices (figure 1.3) appearing after the separation bubble [2, 28, 62, 82, 101, 8]. The inward rotation of these vortices transports the fluid in the middle towards the floor shifting the vortices down as well. This causes the vortices to deflect sideways and away from the vertical symmetry plane at $z = 0$.

The autopower spectra analysis of base pressure signals, fluctuating velocities and force measurements reveal more useful information about the nature of the flow. The dominant modes reported in the literature are presented below.

- In the near-wake the large-scale instantaneous coherent structures are axially parallel to the separation edges and correspond to a periodic pumping motion at frequency $St_H = fH/U_0 \approx 0.08$. In the literature the bubble-pumping frequency has been attributed to the interaction between the lower and upper parts of the vortex ring, causing the vortex structure to move back and forth. More recently the bubble pumping motion has been correlated with the shedding of vortices from the end of the separation bubble for a bus-shaped

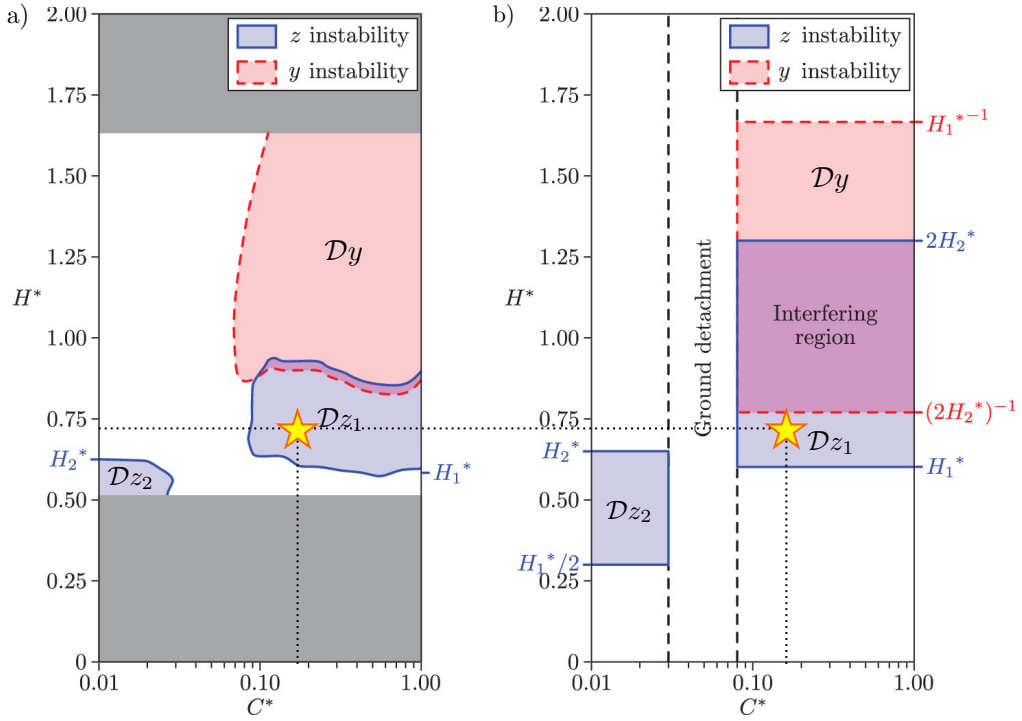


Figure 1.4: Domains of the instabilities measured from the experiments (a) and predicted by the model (b) as reported by Grandemange et. al. The yellow star shows where the conventional Ahmed Body would be on the diagram. [45].

body by Krajnovic et. al. [62]. The pumping frequency was also reported responsible for the periodic variation of the drag on the body [59].

- A characteristic shedding frequency of $St_H \approx 0.20$ has been reported by Bearman et. al. [8] for a car model. A similar frequency of $St_H = 0.22$ was also reported in [62] for a bus-shaped body and in [112] for a square-back Ahmed body, raising a possibility that this vortex shedding frequency exists uniformly across vehicle body wakes. For the square-back Ahmed body geometry Khalighi et. al [59] reports a coherent motion at $St_H = 0.17$ downstream of the recirculation region with a peak of energy particularly clear when the probe is in the plane of symmetry. This vortex shedding mode is also reported by Grandemange et. al. [46] at $St_H \approx 0.17$ and $St_H \approx 0.20$ in the vertical and horizontal planes respectively.

- A high-frequency dynamic was also observed by Duel & George [28] corresponding to the frequency $St_H = 1.16$. This result was interpreted by the authors as the shedding frequency of the mixing layer.

1.2.2 Recent Findings on the Instantaneous Flow

In addition to the modes listed above, very recent studies by Grandemange et. al. [44, 45, 46] revealed random symmetry breaking of the square-back Ahmed body wake. While the time-averaged wake flow is horizontally symmetric, the instantaneous wake flow shows horizontal asymmetry where turbulent flow fluctuations cause the wake to switch between asymmetric states with slow, random timescales resulting in bi-modality, also known as bi-stability [45, 46]. For a general square-back geometry, the direction of the bi-modal behaviour is related to the base aspect ratio and the ground clearance of the geometry, as shown by Grandemange et. al. [45]. According to figure 1.4, showing the instability regions as a function of ground clearance and aspect ratio, given a sufficiently large gap between the body and the ground, the Ahmed body with the spect ration $H^* = 0.74$ should exhibit side-to-side displacement of the wake.

The symmetry breaking behaviour has been reported for a variety of bluff bodies such as spheres, disks and axisymmetric bodies [10, 32, 100, 98, 38]. The symmetry breaking modes (SBM) begin to develop in laminar regimes: as the Reynolds number increases past criticality (known as the bifurcation point) the symmetric flow becomes unstable and starts to exhibit reflectional symmetry breaking regimes. This behaviour was predicted analytically using weakly nonlinear analysis by Meliga et. al. [80] for the laminar flow past a flat plate. Weakly nonlinear analysis is a widely method to describe non-linear evolution of the global eigenmodes. For example, Stuart-Landau amplitude equation

$$\dot{A} = \lambda A - \mu A|A|^2 \tag{1.1}$$

where A is the amplitude, λ is linear complex growth rate and μ is the complex Landau coefficient (normally fitted from experiments), has been shown to predict the oscillation amplitude and frequency of flows near the Hopf bifurcation threshold [95]. In case of flat plate,[80] the authors used multiple time scale asymptotic expansion of the Navier-Stokes equations in the proximity of the bifurcation point, which they truncated at the third order. This resulted in Landau-like equations, describing the perturbation dynamics as a superposition of spatial modes with time-dependent amplitudes. These equations predict the loss of symmetry at the bifurcation point and the subsequent symmetry-breaking behaviour. The observation from experiments that the symmetry breaking behaviour also persists in turbulent regimes motivated further analytical investigation, where the weakly nonlinear analysis was extended to turbulent flow about an axisymmetric body by Rigas et. al. [98, 99]. To include the turbulence effects the authors used the Langevin model, where the deterministic part accounts for the symmetry-breaking dynamics observed at laminar Reynolds numbers and the stochastic term accounts for the turbulent fluctuations. This model predicted the experimentally observed multi-modality: the turbulent fluctuations act as a forcing that causes all possible states of broken symmetry to be explored.

Similar to disks, flat plates and axisymmetric bodies, the Ahmed body wake first exhibits bi-modal behaviour in the laminar regime. Grandemange et. al. [44] found that at $Re_H = \frac{U_0 H}{\nu} = 365$, where H is the height of the body, the Ahmed body wake undergoes a bifurcation from a steady symmetric state to a reflectional symmetry breaking state. The authors have also shown in later studies [45, 46, 43] that as the Reynolds number increases and the flow grows turbulent and unsteady, the wake preserves its preference towards the reflectional symmetry breaking and begins to switch at random between two asymmetric preferred positions. The bi-modal behaviour at turbulent Reynolds numbers has been modelled by Brackston et. al. [12], who used a Langevin model to predict the switching in wake. Further

experimental studies by Perry et. al. [93] and Volpe et. al. [112] also confirmed and further analysed the symmetry breaking behaviour of the turbulent Ahmed body wake. Overall, two coherent behaviours have been reported: at short timescales the wake preserves weak coherent oscillations linked to interactions of the opposing shear layers; at long timescales the flow displays bi-modal behaviour, switching at random between two preferred positions.

This relatively new behaviour has generated a lot of interest within the academic community and industry, encouraging further investigation into the unsteady features of the Ahmed body flow and into the implications of the bi-modal behaviour for flow control. At present the experiments are leading the way in investigating the Ahmed body flow and the asymmetric wake modes, as it is extremely computationally intensive to accurately capture the slow-scale switching at turbulent Reynolds numbers in numerical simulations. One of the first numerical investigations at turbulent Reynolds numbers capturing the asymmetry of the wake is by Pasquetti et. al. [96]. The authors successfully observed one of the asymmetric states, but the simulations were too short to obtain a switch in the wake towards the second asymmetric state. Very recently Lucas et. a. [74] also captured wake asymmetry at turbulent Reynolds number of $Re \approx 4 \times 10^5$, but again the authors did not report on capturing a switch from one asymmetric state to the other.

It is desirable to further develop numerical tools for studying the Ahmed body wake - the access to the full three-dimensional flow field allows visualisation of variety of structures which might not be obtainable experimentally. So far, regardless of the approach, the physical mechanism behind asymmetric switching and the spatial distribution and interaction of the wake topologies are not fully understood. It is however, known, that the asymmetry of the wake and the corresponding pressure gradients have a significant effect on the forces acting on the body [30], including detrimental effects on the body drag. At present, there is a rapidly growing body of literature, documenting the effects of the bi-modality and developing novel control

strategies targeting re-symmetrisation of the wake. The most prominent examples of the control strategies targeting drag reduction of the blunt Ahmed body flows are reviewed in section 1.3.

1.2.3 Real-life Vehicles

It should be noted that the Ahmed body is an idealised and simplified test-case, usually studied without wheels, on stationary ground, with smooth underbody and without an air intake system. However these features can have significant impact on the dynamics and global body forces of the real vehicles, and thus should also be reviewed.

The importance of using a moving ground in testing and simulations largely depends on the vehicle and the purpose of the investigation. For example, in the case of investigating flow past racing cars, which have small ground clearances and are designed to maximise the downforce, large differences arise in measured aerodynamic forces when the floor is stationary compared to when it is moving. A moving ground has also been shown to have significant effects on the flow past sedans. The flow visualisations by Werle [116], reproduced by Sardou [102], show major qualitative differences in the flow dynamics about a model Citroen DS19 when the ground is moving and when it is stationary. The experimental investigation by Bearman et. al. [7] also found that for a typical $1/3^{rd}$ scale car at normal ground clearance (about 5% of the vehicle length) and no wheels, the floor movement reduced drag by about 8% and reduced lift by nearly 30% percent.

A more similar test-case to the Ahmed body was investigated experimentally by Cooper et. al. [21], who evaluated the effects of the moving ground on the flow past a blunt simplified vehicle geometry. The authors conducted experiments past a simple rectangular-block model with rounded leading edges at varying ground clearances. For this geometry the experiments showed that the downforce was nearly the same for the cases with moving and fixed grounds. However, the drag force

clearly increased for all gap distances when the ground was stationary. The authors also observed that in the presence of the moving ground the drag coefficient was less responsive to changes in ground clearance. Grandemange et. al. in [43] tested a square-back Ahmed body in a wind tunnel with a moving ground and rotating wheels, and found that the drag was higher that the one predicted in [2] with stationary floor. The difference in drag was attributed to the combination of differences in the ground clearances, the rotating wheels and the effects of moving ground.

The effects of the underbody roughness on the flow past square-back vehicles were reported by Littlewood et. al. [70]. The authors experimentally investigated the flow dynamics past a full scale Multi-Purpose Vehicle and found that fitting a flat floor to the underbody of the vehicle reduced the drag force by approximately 9% compared to a rough underbody. Similar differences in drag values between wind tunnel tests and road measurements were also reported in [65]. Howell et. al. [53] studied the Windsor model (another popular simplified vehicle geometry) with and without the underbody roughness and also observed a significant drag reduction when the underbody was flat. Similarly, Perry [92] reported that adding an underbody roughness to a Windsor model increased drag by 17% and upwards.

A recent experimental investigation by Cadot et. al. [15] possibly sheds most light on the behaviour of a real vehicle body forces compared to simplified geometries. The authors tested three real square-back vehicles and a sedan in a wind tunnel equipped with a moving ground, allowing the investigation of global body forces in close to real-life environment: with rotating wheels and an air intake system. They found that the correlation between the fluctuations in the drag force and the base pressure did not exceed -0.3 for all vehicles, indicating that in real vehicle flows the underbody roughness and the air intake system are important drag contributors. In comparison, for simplified bluff bodies the base pressure deficit is the main source of drag. Nevertheless, Ahmed body flow successfully recreates the key dynamics found in real-vehicle flows: the large complex separation region at the rear, bi-

modal behaviour and the main wake frequencies are consistent for both real vehicle and the Ahmed body flows. And most importantly, using simplified geometries, such as the Ahmed body, offers an undeniable benefit of investigating these large-scale topologies at a much lower cost.

1.3 Flow Control

Flow control is a rapidly evolving field in fluid dynamics, seeking to introduce modifications to the flow with the goal of achieving some engineering benefit: drag reduction, lift increase, mixing enhancement or noise reduction. Flow control strategies can be classified into three types: passive, active open-loop, and active closed-loop (also known as feedback control). The representative attempts in the literature of flow control for blunt bluff bodies, and specifically the Ahmed body, are reviewed below.

1.3.1 Passive Control

The simplest type of flow control is passive control which uses actuation without power to modify the flow. It is most often implemented using geometrical modifications and has been very popular in applications to square-back ground vehicles, as documented in detail in the review by Cooper et. al. [20]. Specifically boat-tails [59], base cavities [59, 27, 28], splitter plates [27, 40] and base flaps [30] have been shown to be especially effective for reducing aerodynamic drag, reporting drag reductions between 9% and 20%. These strategies, however, require fitting vehicles with quite large devices, which often go against safety, design and usability considerations. More realistic passive control approaches reported in the literature are small chamfers attached to the upper trailing edge at 12° [69] or small short rear end tapers angled at 12° [93]. These devices strongly resemble methods used by car manufacturers to reduce drag and they have been shown to be effective, producing

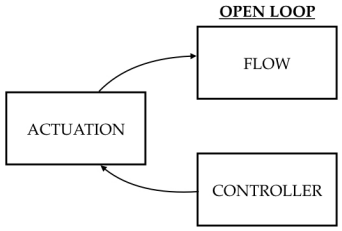


Figure 1.5: Open-loop control schematic

a drag decrease of 4.4% and 2.7% respectively.

1.3.2 Active Open-Loop Control

An approach which circumvents prohibitive geometry changes and can offer further improvement in drag reduction to small passive devices is active flow control. Active control uses powered actuation to manipulate the unforced flow towards a desired outcome. A controller dictates actuation, which in turn affects the flow - a schematic description of how open-loop control works can be seen in figure 1.5. Active control is very versatile. Firstly, there are a number of possible actuation choices including, but not limited to: steady jets, pulsed jets, moving flaps, synthetic jets and etc. Secondly, active control allows one to 'lock-in' to specific frequencies that would naturally be amplified by the flow. And lastly, the performance of passive control devices can deteriorate in off-design conditions, while active control offers the possibility of switching it on and off.

In the context of ground vehicle flows, it has been shown that high frequency forcing can significantly decrease drag for the square-back Ahmed body [6], for a truck model [14] and also for axisymmetric bodies [88]. Significant drag reduction was also achieved for the Ahmed body configurations using steady blowing jets position near the rear edges [113, 101, 71]. In many of these cases, however, the required energy input outweighs the benefits of the control for drag reduction, as highlighted in [71].

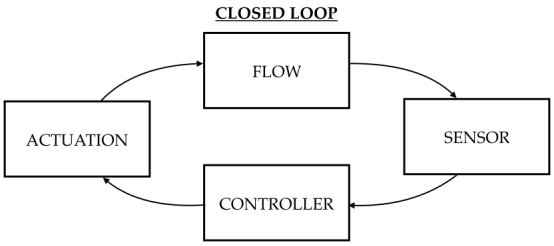


Figure 1.6: Closed-loop control schematic.

1.3.3 Active Closed-Loop Control

Finally, it is possible to reduce drag using closed-loop (feedback) active control strategies. Similar to open-loop, feedback control shapes the behaviour of the flow by introducing disturbances with the help of actuators. However, in feedback control the actuation responds to sensor measurement creating a closed-loop system, such as shown in figure 1.6. The relationship between sensing and actuation is guided by a pre-selected control law which typically relies on mathematical and conceptual models. Feedback control offers a number of advantages: it does not require geometry changes, can adapt to changing conditions and potentially can have a strong effect on the flow.

The representative attempts to reduce form drag using feedback control can be characterised using the choice of control strategy: model-independent controllers based on gradient methods, black box models linking output and input and physics-based approach based on establishing the flow model a-priori from the known flow physics. The body of literature on feedback control applied to ground vehicle-like models is limited, therefore a broader range of bluff-bodies will be covered in the present review, including D-bodies and backward-facing steps.

Physics independent controllers

Gradient-based model-independent controllers are usually extremum- or slope-seeking, i.e. searching for optimum actuation parameters. Extremum-seeking controllers can

be used to find distinct minima and maxima in the steady-state map, while slope-seeking controllers are best used when a parameter needs to return to its saturated value to optimise the controlled variable. Extremum-seeking controllers have been successfully applied to a number of blunt bluff body flows to achieve form-drag reduction. In the experimental work by Henning and King [49], the extremum-seeking controller was used to reduce the drag of the bluff body flow with a trailing edge (akin to D-body). The controller worked towards locking into the vortex shedding, resulting in an aerodynamic drag reduction of approximately 10%. Brackston et. al. in [13] presented an adaptation of extremum-seeking controller for optimisation of the frequency of a harmonic input signal, a common scenario for open-loop flow control systems. The authors then implemented the controller to an axisymmetric blunt bluff body using harmonic forcing as actuation and base mounted pressure sensors. They found that the extremum seeking controller successfully found the optimum forcing configuration, filtered the measured noise and adapted to the changing conditions. Gautier and Aider [37] also successfully implemented a slope-seeking feedback controller in their experiments, achieving a reduction in the recirculation length of the three dimensional backward-facing step flow with an infinite span in horizontal direction. In another experimental study by Pastoor et al. [90] the authors used slope-seeking control on a D-body at $Re_H = 23,000 - 70,000$, where the plant is driving the output to achieve a state on the reference-to-output map corresponding to a pre-defined reference pressure gradient value. Controller was implemented using sinusoidal zero-net-mass-flux actuation at separation and body mounted pressure sensors and yielded a 15% drag reduction. More recently, Li et. al. [68] used wind-tunnel experiments to develop and test a feedback controller for a three-dimensional square-back Ahmed body at $Re = 6 \times 10^5$. The authors applied a single edge open-loop periodic forcing and a gradient based feedback controller actuating along the lateral edges of the base in response to base mounted pressure sensor readings. The authors achieved a pressure recovery of 2% due to the net

balance between the favourable effect of wake symmetrisation and adverse effect of shear-layer mixing and vortex shedding amplification.

Physics based controllers

In physics based controllers the flow behaviour is first approximated in a model based on known flow physics and then the controller is designed. For example, Weller et. al. [115] used a reduced-order model derived from Proper Orthogonal Decomposition (POD) of the square cylinder flow to design a feedback controller for a two-dimensional square cylinder. The controller was then tested numerically using out-of-phase actuation and velocity sensors located in the wake yielding a long-term reduction in drag. In the previously mentioned experimental study by Pastoor et. al. [90] the authors also attempted closed-loop flow control using vortex modelling. The aim of the controller was set to synchronising shear layers using out-of-phase forcing at separation and base mounted pressure sensors. As a result the controller forced the flow out-of-phase with shear layer shedding, postponing vortex formation and achieving a 15% decrease in aerodynamic drag. Alam et. al. [3] used kinematic theory of unsteady separation to model the flow behaviour and design a feedback controller for a two-dimensional backward facing step flow. When the authors tested the controller in numerical simulations at $Re = 200$ they found that the reattachment parameter was successfully altered. Camarri et. al. [17] implemented feedback control based on sensitivity analysis to reduce drag over a square cylinder by stabilising the shedding mode at Reynolds numbers $90 \leq Re \leq 120$. In one of the more recent experimental studies of the turbulent Ahmed body flow, Brackston et. al. [12] designed a feedback controller using the Langevin equation to model the reflectional-symmetry breaking mode in the wake. The controller design used side flaps as actuation in response to base mounted pressure sensors. The controller achieved its aim of suppressing bi-modal dynamics in the Ahmed body wake at turbulent Reynolds numbers and reduced the drag by 2%.

Black-box controllers

Black-box models offer a compromise between completely model-independent and physics-based methods. The controller is built by using input-output data to establish a relationship between actuation and sensor information. While model identification is time consuming the resulting controller can be robust; also these schemes have fast adaptation time and good tracking capability. The literature reports many attempts to design and implement black-box controllers to modify the bluff body wake. Herve et. al. [51] reported a 90% reduction in the measurement of the total energy of the 2D backward-facing step flow at $Re = 500$ due to implementation of feedforward controller with flow-field sensors monitoring the first recirculation bubble. Juillet et. al. [58] also successfully implemented a feedforward controller over the same geometry but with two upstream sensors located ahead of the separation line and successfully reduced the flow perturbation energy. It should be noted that to guide the control strategy it is useful to consider the flow from the perspective of the stability theory. Stability theory focuses on studying the behaviour of disturbances in the flow: i.e. if some disturbance is introduced into a system and it grows with time then the system is unstable, if it decays with time then the system is stable, otherwise the system is called marginally stable. For unstable systems, the growth of the disturbance can be categorised further: if the disturbance grows at the source and spreads the flow is absolutely unstable; or if the disturbance grows but is simultaneously convected away from the source the flow is convectively unstable. According to the classification of flow behaviour introduced by Huerre and Monkewitz [54], bluff body flows can behave in two ways: flows with convective instability display amplifier behaviour and flows with regions of absolute instability display oscillator behaviour. Two-dimensional backward-facing step exhibits both behaviours: oscillator behaviour in the recirculation region and amplified behaviour in the shear layer. The control strategy in [58] targeted the flow dynamics at the separation line - where the flow amplifies all the disturbances. As a result the con-

troller performance benefitted from feed-forward sensor/actuator set-up as upstream sensor locations allows better observability of the noise sources. Becker et. al. [9] applied feedback control to reduce reattachment of the three-dimensional backward facing step flow at $Re = 4000$ experimentally and $Re = 2500$ numerically. Marrot et. al. [78] applied active control loop to turbulent three-dimensional backward facing step flow. The controller responded to flow field measurements from sensors placed in the shear layer and successfully damped oscillations caused by an acoustic excitation. The previously mentioned experimental study by Gautier and Aider [37], also implemented a Proportional Integral Derivative (PID) controller, drastically decreasing the recirculation region length of the three-dimensional backward facing step. The authors report that the black-box PID controller proved to be more effective than the slope-seeking controller. Henning and King in [50] used a multivariable closed-loop robust H_∞ controller acting through harmonic acoustic actuation at separation in response to pressure flow-field sensors to successfully reduce the span-wise reattachment length downstream of the three-dimensional backward-facing step at turbulent Reynolds number. Stalnov et. al. [107] used black-box feedback controller in their experimental study to control the wake behind a three-dimensional D-shaped bluff body at low Reynolds number. The fluidic actuators located at the separation locations forced the flow in response to body-mounted hot-film sensor. The authors successfully demonstrated a reduction of wake unsteadiness and smaller aerodynamic drag. Dahan et. al., Dalla Longa et. al. and Flinois [23, 24, 34] used system identification data to develop a black box sensitivity-based controller for a backward-facing step, D-body and a backward facing step with side walls respectively, achieving significant drag reductions. This thesis aims to build on their work and apply a similar sensitivity-based control approach to a more complex geometry - the Ahmed body. As these investigations are especially important to this thesis, they will be reviewed in more detail in section 2.3.

1.4 Final Remarks

This chapter introduced the main concepts relevant to the work presented in the thesis, such as the specifics of the Ahmed body test-case, its flow dynamics and an overview of possible control approaches suitable for bluff bodies. There is a keen interest in the academic community and industry to understand better the topology of the flow past ground vehicles and explore strategies for flow control. This provides the motivation for the thesis: we aim to study further the dynamics past the Ahmed body using numerical simulations and investigate the use of feedback control to reduce form-drag of the Ahmed body flow.

While it is challenging to capture the long time-scale bi-modal dynamics and the large unsteady wake at the rear of the Ahmed body numerically, the access to the full three-dimensional flow field allows a more detailed and comprehensive study of instantaneous and averaged flows. Also, there are still few examples of feedback controllers applied to the Ahmed body, despite the numerous advantages it offers over other control strategies. One should note, that in the present work, the control is implemented using body-mounted sensing and actuation, which is crucial for eventual application in moving body experiments. This thesis will demonstrate how Large Eddy Simulations can help further the understanding of the Ahmed body flow and how sensitivity based feedback control can be used to achieve a form-drag reduction.

The thesis is structured as follows. Chapter 2 will introduce the methods and concepts used in this thesis such as: details of the LES solver, specifics of the control strategy and the relevant low order modelling tools used to analyse the flow field. Then chapter 3 will present the results from the simulations of the Ahmed body flow at laminar Reynolds numbers based on height of $310 \leq Re_H \leq 435$. The next section 4 presents results from simulations at more representative Reynolds numbers of $Re_H = 25,000$ and $Re_H = 33,000$ with turbulent separation. The last chapter 5

then proceeds to outline the main conclusions drawn from this work.

Chapter 2

Numerical Methods

Computational Fluid Dynamics (CFD) is an established discipline of using numerical methods to solve governing equations of fluid dynamics. Thanks to the increasing computing capacity: both in speed and storage, CFD has become a widely adopted tool for studying complex flows with a wide spectrum of time- and length-scales to complement experimental and theoretical research. To obtain a CFD solution to a flow, first, the geometry and physical bounds are defined and the fluid volume is extracted. Then the fluid volume is divided into discrete cells creating a mesh. The last step is to define the physical modelling and boundary conditions and then to compute the solution. The choice of a CFD modelling scheme is especially important to obtain meaningful results, however it is largely dictated by the resources available and how the CFD is used to complement present work. Since this thesis considers an incompressible flow of a Newtonian fluid, this section will focus on numerical methods discretising and solving the Navier-Stokes equations.

Reynolds-Averaged Navier-Stokes (RANS) equations are the most computationally economical approach to turbulence modelling. The Navier-Stokes equations are ensemble-averaged, converting turbulent fluctuations into Reynolds stresses and resolving only large-scale rotational motions. This methods describes the flows in statistical sense and leads towards averaged pressure and velocity fields. Statisti-

cally unsteady flows can equally be treated within the RANS framework and are often referred to as Unsteady Reynolds-Averaged Navier-Stokes (URANS). URANS also models the turbulence, but resolves the unsteady mean flow structures - usually larger than turbulent eddies. These methods are usually challenged by flows around bluff bodies, due to massive flow separation, recirculation, shedding and existence of inherent three-dimensional flow structures and unsteady behaviour.

On the other side of the accuracy spectrum for turbulent flows is the Direct Numerical Simulations (DNS), whereby all scales are resolved. This approach, while the most accurate, is still prohibitively expensive for most realistic flows as the computational cost of DNS scales proportionately with Re^3 [94].

Large Eddy Simulations (LES) offer a compromise between computational efficiency and accuracy. While the large turbulent scales are fully resolved, the computational cost is reduced by filtering out the smallest (and most expensive to resolve) length-scales and modelling them with a subgrid-scale model. While this method requires more computational resources than RANS, it allows access to instantaneous flow fields and resolves the complete range of scales of random motion, up to the cut-off frequency of the LES filter. The smaller computational costs and ability to observe instantaneous flow structures has made LES attractive for many application from accurate tracking and description of wingtip vortices [73] to predicting combustion instabilities [67]. Bluff body flows are especially well positioned to benefit from computational savings and accuracy of Large Eddy Simulations. One of the implications of Kolmogorov's theory of self-similarity [60] is that the large eddies depend on the geometry, while the small scales are more universal. This feature implies that LES is well positioned to handle inherently three-dimensional flows with massive separation and recirculating regions at a lower computational cost than DNS.

Insight into instantaneous flow behaviour is important for studying the flow around the Ahmed body for two reasons: the fluctuating components of the pressure and velocity affect drag and Ahmed body wake exhibits random bi-modal switching

which which can only be captured if there is access to instantaneous flow-field variations. Therefore, LES is used for all the simulations in this work. The theoretical background and the specifics of the flow solver are described next.

2.1 Large Eddy Simulations

2.1.1 Governing LES Equations

The dynamics of an incompressible flow of a Newtonian fluid are described by the equations of conservations of mass and momentum, known as the Navier-Stokes equations. In tensor notation these are:

$$\begin{aligned} \frac{\partial u_i}{\partial x_i} &= 0 \\ \frac{\partial u_i}{\partial t} + \frac{\partial u_i u_j}{\partial x_j} &= -\frac{1}{\rho}\frac{\partial p}{\partial x_i} + \nu \frac{\partial^2 u_i}{\partial x_j^2} \end{aligned} \tag{2.1}$$

where ρ is fluid density, p is the pressure, t is time, and u_i and x_i are the velocity and the spatial components in the i^{th} direction respectively so that $\mathbf{u} = (u_1, u_2, u_3)$ and $\mathbf{x} = (x, y, z)$. The variables in equations (2.1) are then non-dimensionalised using the characteristic flow velocity U_∞ and characteristic length-scale for the flow, in this case H for body height:

$$t^* = \frac{tU_\infty}{H}, \quad u_i^* = \frac{u_i}{U_\infty}, \quad p^* = \frac{p}{\rho U_\infty^2}, \quad x^* = \frac{x}{H}, \quad Re = \frac{U_\infty H}{\nu} \tag{2.2}$$

where Re is the Reynolds number. The resulting Navier-Stokes equations are:

$$\begin{aligned} \frac{\partial u_i^*}{\partial x_i^*} &= 0 \\ \frac{\partial u_i^*}{\partial t^*} + \frac{\partial u_i^* u_j^*}{\partial x_j^*} &= -\frac{\partial p^*}{\partial x_i^*} + \frac{1}{Re}\frac{\partial^2 u_i^*}{\partial x_j^{*2}} \end{aligned} \tag{2.3}$$

The governing LES equations are then obtained by separating the resolved

and modelled parts using a spatial filter applied via a convolution function with a filtering kernel G. This is equivalent to splitting up any field into a filtered and a sub-filtered parts, e.g. $u_i^* = \overline{u}_i + u_i'$ where $\overline{u}$ is the resolvable part and u_i' is the subgrid-scale part. The resulting filtered Navier-Stokes equations are:

$$\begin{aligned} \frac{\partial \overline{u}_i}{\partial x_i} &= 0 \\ \frac{\partial \overline{u}_i}{\partial t} &= -\frac{\partial \overline{u}_i \overline{u}_j}{\partial x_j} - \frac{\partial \overline{p}}{\partial x_i} + \frac{2}{Re}\frac{\partial \overline{S}_{ij}}{\partial x_j} - \frac{\partial \tau_{ij}}{\partial x_j} \end{aligned} \tag{2.4}$$

where $\overline{S}_{ij} = \frac{1}{2}(\frac{\partial \overline{u}_i}{\partial x_j} + \frac{\partial \overline{u}_j}{\partial x_i})$ is a strain rate tensor and τ_{ij} is the subgrid-scale stress tensor that must be modelled to close the equations (2.4).

2.1.2 Subgrid-Scale Modelling

The principal role of the subgrid-scale (SGS) modelling is to extract the turbulent energy cascading from the large resolved structures across the cut-off frequencies. The most popular SGS models are the 'eddy viscosity models', where the traceless part of the subgrid-scale stress is defined as:

$$\tau_{ij} - \frac{1}{3}\delta_{ij}\tau_{kk} = -\nu_t\Big(\frac{\partial \overline{u}_i}{\partial x_j} + \frac{\partial \overline{u}_j}{\partial x_i}\Big) = -2\nu_t \overline{S}_{ij} \tag{2.5}$$

where δ_{ij} is the Kronecker delta and ν_t is the turbulent viscosity. The isotropic part of τ_{ij} is incorporated within the filtered static pressure term.

Eddy viscosity models differ in the way ν_t is defined. The most common one is the Smagorinsky model [106] with eddy viscosity defined as $\nu_t = (C_s\Delta)^2|\overline{S}|$ where C_s is the Smagorinsky constant and Δ is the filter width. This simple model has been successfully applied to simulations of numerous flows, however it has some well-known shortcomings. Firstly, the Smagorinsky constant, C_s, needs calibrating for different types of flows to correctly reproduce the decay of homogeneous isotropic turbulence for the specific implementation and code. Secondly the model is known

to be very dissipative and therefore not appropriate for simulating transition. Specifically pertaining to the Ahmed body flow, we believe that overly dissipative models could delay or even prevent bi-modal switching in the wake. Lastly the model allows ν_t to be non-zero at the wall despite the no-slip condition. This, however, is often counteracted by an exponential damping function to ensure τ_{ij} vanishes at the wall.

To capture the bi-modal dynamics of the Ahmed body wake flow, it is important that transition and small-scale strain rates are simulated accurately and reliably. Therefore all simulations described in this thesis employed the Wall-Adapting Local Eddy-Viscosity (WALE) model introduced by Nicoud and Ducros [85]. Unlike the Smagorinsky model, the WALE model can handle transition and ν_t naturally vanishes at solid boundaries and in the region of the boundary layer when transition begins [84]. It also accounts for the effects of the strain and the rotation rate of the smallest resolved turbulent fluctuations. The model has been tested on various flows and performed well on all of the above criteria [85, 108, 23].

2.1.3 LES Solver

Simulations presented in this thesis were performed using an in-house parallel LES flow solver *StreamLES*. This section will briefly present the key features of the code. For a more detailed description of the software and code validation, the interested reader is directed to the works by Temmerman [108] and Lardat et. al. [64]. More recently *StreamLES* was used to successfully simulate bluff body flows in [23, 24, 34].

StreamLES is a finite volume incompressible flow solver with fully-collocated storage, where the pressure-velocity decoupling is addressed by the Rhie & Chow interpolation practice [97]. The code uses fractional step method to discretise the governing equations in time, domain decomposition to parallelise the solution, and a multi grid algorithm to accelerate the solution convergence. The relevant specifics of the code are overviewed next.

Discretisation in space

The finite volume discretisation formulation of the governing Navier-Stokes equations is:

$$\int_{\Omega} \frac{\partial \overline{u}_i}{\partial x_i} d\Omega = 0 \tag{2.6}$$

$$\int_{\Omega} \frac{\partial \overline{u}_i}{\partial t} d\Omega = -\int_{\Omega} \frac{\partial \overline{u}_i \overline{u}_j}{\partial x_i} d\Omega - \int_{\Omega} \frac{\partial \overline{p}}{\partial x_i} d\Omega + \int_{\Omega} \frac{2}{Re} \Big(\frac{\partial \overline{S}_{ij}}{\partial x_j} + \frac{\partial \tau_{ij}}{\partial x_j} \Big) d\Omega \tag{2.7}$$

where Ω can be any of the finite volumes or the whole domain due to the conservative nature of the formulation. Recalling that the subgrid-scale stress is approximated by equation (2.5), the momentum equation can be rewritten as:

$$\int_{\Omega} \frac{\partial \overline{u}_i}{\partial t} d\Omega = -\int_{\Omega} \frac{\partial \overline{u}_i \overline{u}_j}{\partial x_i} d\Omega - \int_{\Omega} \frac{\partial \overline{p}}{\partial x_i} d\Omega + 2 \int_{\Omega} \frac{\partial (\nu_{tot} \overline{S}_{ij})}{\partial x_j} d\Omega \tag{2.8}$$

where the deviatoric part of the subgrid-scale tensor is merged with the pressure gradient so that $\overline{p} = \overline{p} - \frac{1}{3}\delta_{ij}\tau_{kk}$ and $\nu_{tot} = \frac{1}{Re} + \nu_t$, where ν_t is the eddy viscosity defined by the subgrid-scale model. *StreamLES* employs a collocated cell-centred storage approach, where the gridlines define the faces of the finite volumes and the average flow-field variables for each cell ($\mathbf{u}$ and p) are stored at the volume centroid. The velocities at the cell faces are stored as mass fluxes; this greatly simplifies the spatial treatment of convective and diffusive terms in (2.8) as demonstrated below.

The convective term in equation (2.8) is approximated using the Gauss divergence theorem:

$$\int_{\Omega} \frac{\partial \overline{u}_i \overline{u}_j}{\partial x_i} d\Omega = \int_{S} (\overline{u}_i \overline{u}_j) n_j dS \tag{2.9}$$

where S is the cell surface and n_j is the j^{th}-component of the vector normal to the cell face. Applying the second-order midpoint rule to approximate the surface integral in equations (2.9) gives:

$$\int_{S} (\overline{u}_i \overline{u}_j) n_j dS = \sum_{c=e,w,n,s,t,b} \overline{u}_i^c \; \overline{u}_j^c \; S_j^c = \sum_{c=e,w,n,s,t,b} \overline{u}_i^c \; C^c \tag{2.10}$$

where c represents the different faces of the control volume identified by six directions: e - east, w - west, n - north, s - south, t - top, b - bottom. Here $C^c = \overline{u}_j^c \; S_j^c$ is the mass flux through the cell face, where $\overline{u}_i^c$ is the i^{th} component of quantity convected through the cell face and S_j^c is the vector normal to the cell face with magnitude equal to its area.

The diffusive term is treated slightly differently due to the presence of the double derivative. First, using the Gauss divergence theorem to convert the volume integral to a surface integral and then applying the midpoint rule gives:

$$\int_\Omega \frac{\partial^2 \overline{u}_i}{\partial x_j^2} d\Omega = \int_S \frac{\partial \overline{u}_i}{\partial x_j} n_j dS \sum_{c=e,w,n,s,t,b} \Big(\frac{\partial \overline{u}_i}{\partial x_j}\Big)^c S_{x_j}^c \tag{2.11}$$

The gradient in equation (2.11) is centred on the cell face. To proceed, it needs to be expressed in terms of known velocities and geometric factors, i.e rewritten as the volume integral so the divergence theorem can be applied again.

$$\Big(\frac{\partial \overline{u}_i}{\partial x_j}\Big)^c = \frac{1}{\Omega_c} \int_{\Omega_c} \Big(\frac{\partial \overline{u}_i}{\partial x_j}\Big)^c d\Omega_c \tag{2.12}$$

Here a staggered volume Ω_c is considered. The geometric parameters at the staggered surfaces are computed as cell-averages: $S_j^S = (S_j^w + S_j^e)/2$, where S_j^S is the $j-$component of the staggered surface vector oriented in the direction *WE*. The final step is to apply the divergence theorem and the midpoint rule again:

$$\frac{1}{\Omega_c} \int_{\Omega_c} \Big(\frac{\partial \overline{u}_i}{\partial x_j}\Big)^c d\Omega_c = \frac{1}{\Omega_c} \int_S \overline{u}_i n_j dS = \frac{1}{\Omega_c} \sum_{c=e,w,n,s,t,b} \overline{u}_i^c \; S_j^c. \tag{2.13}$$

Discretisation in time

To advance the solution forward in time *StreamLES* uses a popular time-marching strategy called the fractional step method [19]. The algorithm for implementing the method consists of two parts, essentially representing an operator splitting mecha-

nism where the viscous and pressure forces are considered separately. In the first part, the solution is stepped forward in time to obtain an intermediate velocity field. At this stage conservation of mass is not satisfied and the velocity field needs to be corrected. In the second part the pressure is computed. It is then used to update the intermediate velocity and obtain the divergence-free velocity field. The specifics of implementation of the fractional step method in *StreamLES* are described below.

Firstly, the 2^{nd} oder backward Euler scheme is used to approximate the time derivative in the momentum equation (2.7) so that $\frac{\partial \overline{u}_i}{\partial t} = \frac{\overline{u}^{n+1} - 4\overline{u}_i^n + \overline{u}_i^{n-1}}{2\Delta t}$. At this step the pressure term of the momentum equation is ignored and the convective and diffusive terms are advanced in time using a third-order Gear-like scheme documented by Fishpool and Leschziner [33]. Compared to the second-order formulation, the extension to third-order improves the performance of the Gear-like scheme in terms of stability and accuracy [33] . At this step the velocity field is not divergence-free and needs to be corrected. However, to proceed to the second part of the fractional step-method algorithm, it is, first, necessary to interpolate the intermediate contravariant velocity C^* from the intermediate velocity field u_i^*. This is done using the relation:

$$C_i^* = L(u_i^*)S_i \tag{2.14}$$

where L is the linear interpolation from the cell centres to the cell faces and S_i is the normal vector to cell face i normalised by cell face surface. To obtain a well-posed problem for the second step the normal component of the intermediate contravariant velocity is specified on the boundary as:

$$C_i^{n+1} n_i = C_i^* n_i = const. \tag{2.15}$$

Furthermore to ensure that the condition of mass conservation is satisfied, $\int_\Gamma C_i^* n_i \, d\Gamma = 0$ has to hold.

The intermediate contravariant velocity is now projected onto the space of

divergence-free vector field by adding the gradient of the pressure:

$$\frac{3}{2\Delta t}(C_i^{n+1} - C_i^*) = -\frac{\partial \overline{p}^{n+1}}{\partial x_i}. \tag{2.16}$$

Applying the boundary condition (2.14) to equation (2.16) gives

$$-\frac{\partial \overline{p}^{n+1}}{\partial x_i} n_i = \frac{3}{2\Delta t}(C_i^{n+1} - C_i^*) n_i = 0. \tag{2.17}$$

Then applying the divergence operator on equation (2.16) in conjunction with the mass-conservation equation ($\frac{\partial \overline{u}_i}{\partial x_i} = 0$) gives the following system:

$$\begin{cases} \dfrac{\partial^2 \overline{p}^{n+1}}{\partial x_i^2} = \frac{3}{2\Delta t} C_i^* \\ \dfrac{\partial \overline{p}^{n+1}}{\partial x_i} n_i = 0. \end{cases} \tag{2.18}$$

System (2.18) is fully implicit and its solution is the most expensive part of the computation. To accelerate the convergence within any time-step a multigrid algorithm is employed. The method for solving for pressure is described in the next section.

Once the pressure p^{n+1} is solved, the contravariant velocity is updated using equation (2.16). The cartesian velocity $\overline{u}_i^*$ is updated through a similar equation

$$\frac{3}{2\Delta t}(\overline{u}_i^{n+1} - \overline{u}_i^*) = -\frac{\partial \overline{p}^{n+1}}{\partial x_i}, \tag{2.19}$$

where the difference is in the discrete gradient: staggered for the contravariant velocity and cell-centred for the cartesian. Since the solver uses collocated storage, spurious numerical oscillations can dominate the solution due to pressure-velocity decoupling. The use of different discrete gradients for updating the cartesian and contravariant velocities allows the coupling to be reestablished and is equivalent to applying the Rhie and Chow procedure [97].

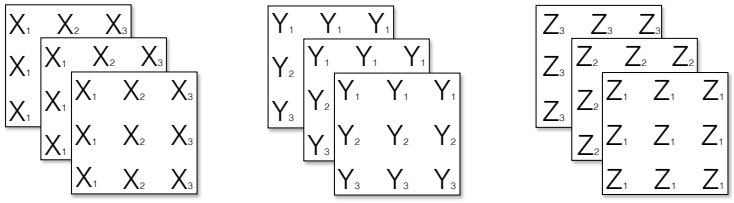


Figure 2.1: Data structure requirement for the grid blocks.

Pressure solver

The pressure at time $(n+1)$ is the solution of the system of equations (2.18). Considering a $2D$ mesh and writing system (2.18) in matrix form gives:

$$L\mathbf{p} = \mathbf{S} \tag{2.20}$$

where L is the matrix of coefficients, $\mathbf{p}$ is pressure and $\mathbf{S}$ is the right-hand-side of system of equations (2.18). The most straight-forward and coincidentally computationally expensive method for solving to $\mathbf{p}$ is to invert L. Instead *StreamLES* uses Successive Line Over-Relaxation (SLOR) and an alternate direction implicit techniques. Starting from an initial guess, the solution is corrected in successive sweeps through the mesh alternating in the $x-$ and $y-$directions until the convergence reaches the user-set tolerance level. The SLOR technique speeds up the convergence of each iteration by overestimating the correction of each point with a relaxation parameter ω. Because of the highly non-orthogonal mesh at the nose of the geometry in our case, the relaxation factor was set to 1 to maintain stability of the code, equating the SLOR scheme to the common Gauss-Seidel method.

The Gauss-Seidel technique produces smooth errors. A few iterations remove almost all high frequencies in the error vector e, however, low frequencies are reduced at a much lower rate significantly slowing down the rate of convergence. It is estimated that convergence requires $\mathcal{O}(N^2)$ iterations, where N is the number of meshpoints. To accelerate the convergence further a multi-grid V-cycling algorithm

is used. Firstly a few sweeps are performed on the original grid to damp out the high frequencies of the residual. If the solution has not converged, a coarser mesh if obtained by removing every other computational node and the smoothened residual is then represented on the new mesh. A few sweeps through the new mesh damp out the highest frequencies again. If convergence is not reached and it is possible to construct an even coarser grid, more mesh points are removed and the solution is iterated until all frequencies of the residual have been damped. Finally the solution is transferred onto the original mesh with a computational time saving achieved as it is much cheaper to sweep on a coarse mesh than the original one.

2.2 Pre-Processing

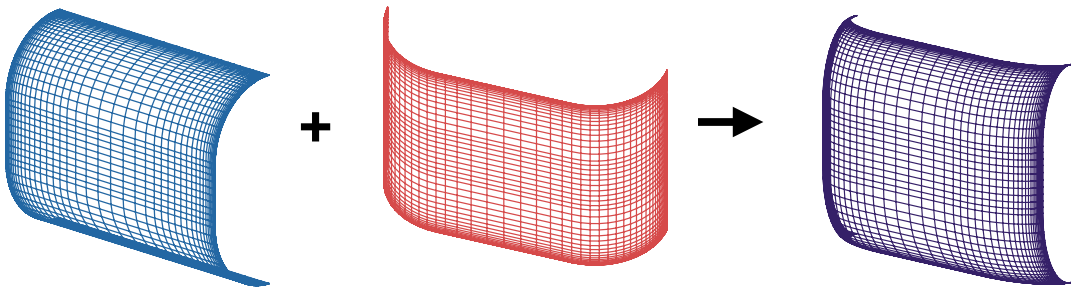


Figure 2.2: Generation of the rounded nose surface, where red (R) and blue (B) surfaces are used to generate the curved purple (P) surface using the relation $\frac{B+R}{2} = P$

StreamLES runs on a Cartesian grid which needs to be created and divided into blocks (for parallelisation) prior to simulations. StreamLES has been shown to perform very well on simple orthogonal geometries, where a grid can be produced using relatively simple algebraic grid generation routines. In the case of discretising the computational space around an Ahmed body two challenges were encountered. Firstly, StreamLES reads in only grid files in binary format where each file has to have the specific data structure shown in figure 2.1. This ruled out using any existing

mesh generation software for grid generation. Secondly the curvature of the nose introduces an extra level of complexity: it is important to keep the skew in the grid low and computational cells near the curved boundary as orthogonal to the body as possible. Therefore the grid was created using MATLAB where it was easy to visualise and adjust the key grid areas.

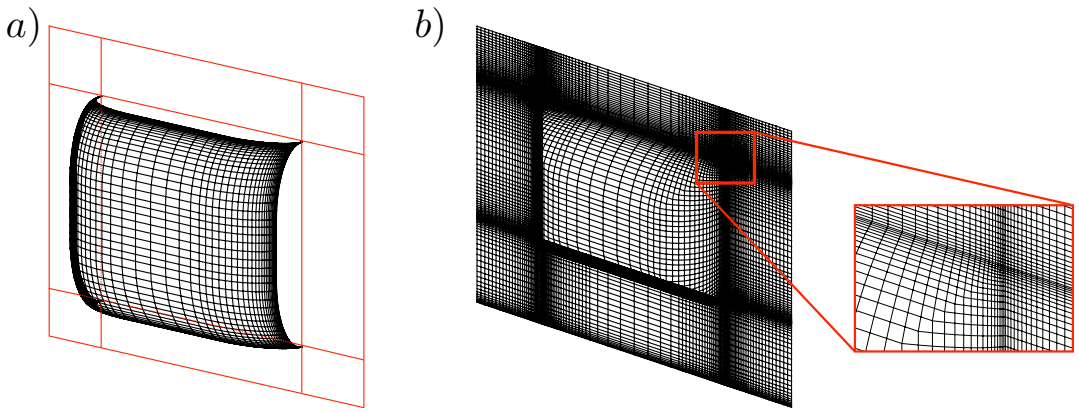


Figure 2.3: Generation of the rounded nose surface. *a)* red lines show the surface onto which the edges of the initial curved surface are projected. *b)* resulting mesh with emphasis on the discretisation of the corner.

By far the most challenging aspect of grid generation was defining the curved boundary at the nose of the body without creating significantly skewed cells. First, two curved surfaces were created and overlaid, as shown in figure 2.2. This results in the initial curved surface (purple surface in figure 2.2) from which the nose boundary is formed. Then a rectangular surface is defined at the base of the initial surface. The borders of the initial curved surface are then projected onto the defined boundary, smoothing out the stretched corners and creating the Ahmed body nose (figure 2.3). The corners of the nose are smoothed out further using hyperbolic functions, to ensure low skew and expansion ratio between the cells.

The rest of the mesh is very modular consisting of an O-grid spanning from the nose towards the inlet, followed by an area populated using three-dimensional linear transfinite interpolation algorithm (overviewed in more detail in appendix A

and [109]). This was done to create a smooth transition between the O-grid and the rest of the domain in the inlet. The different components of the mesh around the front of the body are shown in figure 2.4. The rest of the domain was populated using simple algebraic relations.

Unless otherwise stated, all simulations in this work were performed with a stationary ground. The boundary conditions for all simulations presented in this thesis are set as follows:

- The boundaries on the ground and around the body surfaces are defined by a no slip condition where $u(x,t) = (\mathbf{u}(\mathbf{x},t), v(\mathbf{x},t), w(\mathbf{x},t)) = (0,0,0)$.
- A free-slip condition was imposed at the domain sides as: $w(\mathbf{x},t) = \frac{\partial u}{\partial z}(\mathbf{x},t) = \frac{\partial v}{\partial z}(\mathbf{x},t) = 0$ and at the top boundary of the domain as: $v(\mathbf{x},t) = \frac{\partial u}{\partial y}(\mathbf{x},t) = \frac{\partial w}{\partial y}(\mathbf{x},t) = 0$.
- The outflow condition is imposed using the advection equation for the velocity: $\frac{\partial \mathbf{u}}{\partial t}(\mathbf{x},t) + U_\infty \frac{\partial \mathbf{u}}{\partial x}(\mathbf{x},t) = (0,0,0)$.
- At the inflow a constant velocity is imposed and the simulation is allowed to run for a few flow-throughs for the flow to develop along the floor and Ahmed body boundaries.

2.3 Control Strategy

The project investigates a control strategy for drag reduction targeting attenuation of pressure fluctuations in the wake. It is postulated that reducing base pressure fluctuations will lead to pressure recovery and subsequent decrease in drag. The theoretical framework for the approach is outlined by Dalla Longa et. al. in [24] where the authors used volume integral analysis to demonstrate that fluctuating component of the velocity affects the mean drag. The control is implemented using

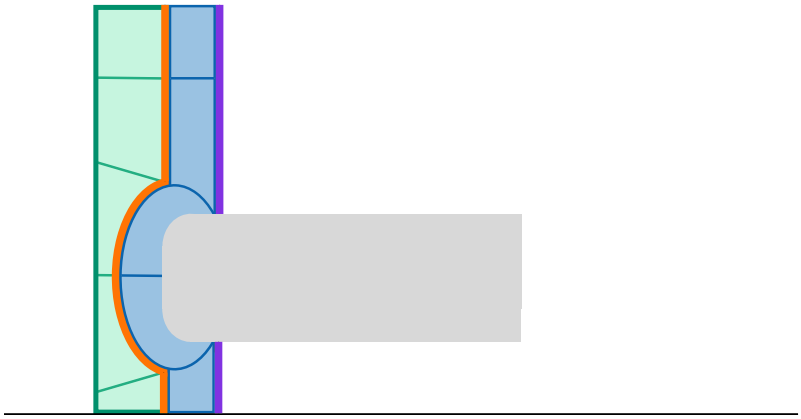


Figure 2.4: Structure of the mesh, where green area is populated using linear transfinite interpolation from the orange boundary towards the inlet and blue area is populated using an O-grid algorithm.

body-mounted actuators and sensors; the flow is forced using zero-net-mass-flux synthetic jets in response to the base pressure force signal measured with base-mounted sensors. This control arrangement was chosen to satisfy two conditions: efficiency and ease of transfer to real-life environment. For this reason, body mounted pressure sensors were chosen over flow field sensors, which might provide the controller with more information about wake dynamics but are not feasible in real life situations. It should be noted that previous studies [12], [62], [46] have shown that the base pressure signal carries the frequency signatures of the key wake dynamics: shedding and bubble pumping. It is thus assumed here that base pressure can provide state vectors to sufficiently observe the dynamics of the wake. Actuation is implemented using zero-net-mass flux synthetic jets as they are convenient from an experimental point of view and efficient in terms of power they require for operation. The actuation shape itself is chosen based on the findings from the analysis of the unforced flow. The exact sensor and actuator arrangement will be presented in the next chapter.

As previously mentioned, a square-back Ahmed body is classed as a three-dimensional blunt bluff body, which according to the classification introduced by Huerre and Monkewitz [54] can behave in two ways: convectively unstable displaying

amplifier behaviour and absolutely unstable displaying oscillator behaviour. This distinction in behaviour affects the choice of the control strategy. In amplifier flows perturbations are amplified locally and then convected downstream. These flows typically react sensitively to perturbations and other noise sources. Any controller designed for the amplifier flows, therefore, would need to accurately capture the noise environment. In case of oscillator flows, there is usually a critical Reynolds number, past which the flow becomes globally absolutely unstable and establishes a limit cycle behaviour. The flow becomes relatively insensitive to external disturbances and the dominant frequency of the flow is then little influenced by noise sources. At this point it is possible to use linear control tools to attempt to suppress linear instabilities. For a controller to increase base-pressure of the Ahmed body it needs to affect the recirculation region with limit-cycle behaviour, i.e. targeting oscillator flow behaviour. In this framework, the control actuation can also be unsteady, as based on the assumption of dynamic linearity the flow changes to unsteady actuation are predominantly linear as well. The remainder of the chapter will outline the linear feedback control strategy tested and implemented in this work.

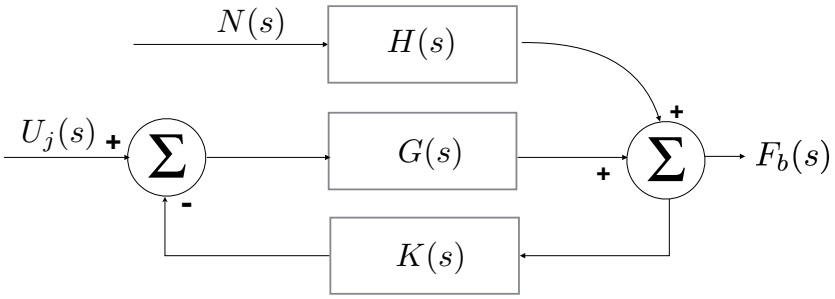


Figure 2.5: Dynamically linear model for feedback control: s denotes Laplace transform variable.

The feedback control approach investigated here is based on what is known as sensitivity transfer function and is summarised in the schematic in figure 2.5. Denoting s as the Laplace transform variable, fluctuations in the base pressure force $F_b(s)$ are assumed to respond in a dynamically linear manner both to the actuation,

$U_j(s)$, and to natural disturbances in the flow, $N(s)$. The Laplace transforms of the base pressure fluctuations in the absence and presence of feedback control then take the forms:

$$F_{b,\text{no control}}(s) = U_j(s)G(s) + H(s)N(s) \quad F_{b,\text{control}}(s) = \frac{U_j(s)G(s) + H(s)N(s)}{1 + G(s)K(s)} \tag{2.21}$$

The ratio of the size of these fluctuations with control to those without is then given by the magnitude of the "sensitivity transfer function";

$$|S(s)| = \frac{|F_{b,\text{control}}(s)|}{|F_{b,\text{no control}}(s)|} = \left|\frac{1}{1 + G(s)K(s)}\right|. \tag{2.22}$$

Therefore for the feedback controller, $K(s)$, to attenuate fluctuations, it is required that the sensitivity transfer function is below one $|S(s)| < 1$, i.e. the flow with feedback control has less fluctuations in the base pressure than then flow without feedback control. However, as the amplitude of the frequency response is reduced in one part of the spectrum, it may have to get larger in the other part due to the "waterbed effect" of the Bode sensitivity integral [36, 18]. Since the sensitivity cannot be small over the entire frequency range, the relation $|S(s)| < 1$ needs to hold over the frequencies where the wake exhibits significant dynamics, i.e. the most prominent frequencies in the sensor signal, given that the sensor signal is placed intelligently to ensure sufficient observability of the flow. It is thus important to identify the dominant frequencies of the sensor signal in the unforced flow, with the view to target these frequencies with feedback control.

The controller design described above requires a low-order linear model for $G(s)$, which represents how the sensor signal, $F_b(s)$, responds to actuation, $U_j(s)$. The model is derived from system identification data collected from open-loop simulations, where the flow is actuated using harmonic jets and the resulting shift in phase and gain of the sensor signal is recorded to form the basis of the model. While

there are a number of actuation choices, such as multi-sines or non-periodic signals overviewed in detail in [72], harmonic forcing is chosen in this work as it allows one to quantify and address potential nonlinearities of the system. Harmonic forcing allows one to characterise nonlinearity levels by checking *a)* that the main response frequency is at the forcing frequency and *b)* that the gain and phase shift remain within close bounds across the frequency spectrum when forcing at different amplitudes. A commonly encountered nonlinearity is "weak nonlinearity" - where the dominant response frequency matches the forcing frequency, but the gain and phase shift vary with forcing amplitude (as well as frequency). Recently Li and Morgans [67] proposed the use of the $\nu-$gap metric, introduced by Vinnicombe in [111], to rigorously account for weak nonlinearity in the design of linear feedback controller. Flinois et. al. [35] also used ν-gap combined with $\mathcal{H}_\infty$ loop-shaping to design a feedback controller to stabilise flow past a two-dimensional D-body. Additionally, harmonic forcing can also provide insight into flow response to specific forcing frequencies, which could be especially interesting for frequencies near the "lock-in" region (forcing near the dominant frequency).

The downside of using harmonic forcing is the associated computation costs. A complete model requires a large volume of simulations, as each calculation provides response information for a single frequency only. On top of that, each simulation has to run for a sufficiently long time for the transients to die away, amounting to an even larger requirement for the computational resource. In the present work the level of nonlinearities in the system is unknown, and thus the benefits of using harmonic forcing to gather system identification data are deemed worth the extra computational cost. The assumption of linearity is then evaluated by considering the amount of independence in the system identification data for different amplitudes of open-loop forcing.

As previously mentioned, the controller is designed with the view that reducing base pressure fluctuations will favourably affect the drag. This strategy has been

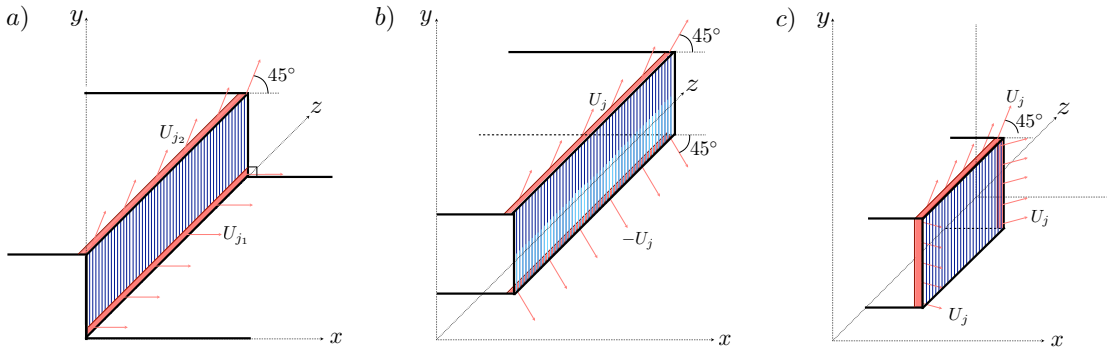


Figure 2.6: Sensor and actuation arrangement for blunt bluff body feedback control as implemented by *a)* Dahan. et. al [23] with the sensor measuring the pressure integrated over the base (dark blue) and two separate actuation locations U_{j_1} and U_{j_2}, *b)* Dalla Longa et.al. [24] with anti-symmetric sensor measurement of base pressure (light and dark blue) and out-of-phase forcing at the separation edges, and *c)* Flinois [34] with sensor measuring the pressure integrated over the base (dark blue) and uniform forcing along the separation edges. In all graphs the red arrows indicate the position and directions of the oscillating jets.

previously observed to work well as the basis for control design for bluff bodies by Dahan et. al. [23], Dalla Longa et. al. [24] and Flinois. [34]. Similar to the approach in this work, the authors in these studies [23, 24, 34] used synthetic jets, body mounted sensors and sensitivity-based feedback control to achieve drag reduction on the three-dimensional backward-facing step, three-dimensional D-body and a three-dimensional backward-facing step with side walls, respectively. The feedback control set-up in their study is shown in figure 2.6. Dahan et. al. looked at two separate locations for actuation: at the bottom of the backward-facing step base (U_{j_1}) to affect the secondary recirculation bubble and at the backward-facing step edge (U_{j_2}) to target the region of amplification near the separating shear layer. At turbulent Reynolds numbers, the authors report an increase in mean base pressure of 20% with the actuator located at the separation edge and a 10% increase with the actuator at the bottom of the base. Dalla Longa et. al. [24] considered the flow behind a D-shaped body with two separation lines. The authors employed actuation in which the two actuation locations were in anti-phase and with anti-symmetric sensing to better capture the asymmetric vortex shedding and hence

asymmetric component of the base pressure distribution. The resulting controller weakened the shear layers shedding from the edges of the D-body, elongating the recirculation region and delaying mixing leading to a 38% base pressure recovery. A more complex geometry exhibiting side walls and three-dimensional fluctuations was studied by Flinois, who implemented the sensitivity-based feedback control and found that it successfully suppressed base pressure fluctuations and achieved an increase in base pressure of around 10%. In present work we are looking to build further on these results and apply the control strategy described above to a more representative geometry - the three-dimensional Ahmed body.

2.4 Modal analysis

Here, we present a quick overview of modal analysis tools, used in the next chapters to gain further insight into the flow dynamics. Methods of Proper Orthogonal Decomposition (POD) and Dynamic Mode Decomposition (DMD) are used to reveal the energy content, spatial structure and temporal behaviour of the coherent structures in the wake. The theoretical background for POD and DMD is described below.

2.4.1 Proper Orthogonal Decomposition

Proper Orthogonal Decomposition (POD) is a powerful and elegant method of extracting large-scale energetic flow structures from a flow field by decomposing it into spatial modes and related time-dependent amplitudes. The POD algorithm derives an orthonormal basis in the least-squares sense for a given set of data, where the basis is ordered from the most to least energetic modes. POD offers a number of advantages for analysing fluid flows. Firstly, it does not require prior knowledge of the system behaviour to analyse patterns in the data. Secondly it is relatively computationally efficient as it requires only standard matrix manipulations. Even

when applied to nonlinear problems, the POD algorithm can provide insight into flow structures relatively cheaply. Because of this, POD has been widely used to study turbulent flows and their coherent structures. After Lumley first applied POD to study turbulent structures in [75], this decomposition method has been used to study numerous fluid flows, [11, 26, 83, 91]. More recently, Rigas et. al. [100] used POD to extract coherent structures from the snapshots of the axisymmetric body base and to reveal multi-stable behaviour. Östh et. al. [87] successfully applied POD to a three dimensional Ahmed body flow to extract the most relevant flow dynamics and construct reduced order flow model.

One of the most widely used methods for POD and the one later employed in this work is the method of snapshots developed by Sirovich [105]. The snapshot method produces the same results as the classical POD method, but it is better suited for cases where the number of measurement locations is greater than the number of instantaneous flow-field snapshots. This work uses the full three-dimensional wake snapshots as the input for the POD algorithm, rather that signal measurements, to visualise three-dimensional modes and better understand their spatial structure. Therefore the method of snapshots is better suited for present work and its mathematical framework and implementation is reviewed next. For the classical POD approach an interested reader is referred to Holmes et. al. [52] and Lumley [76]. To demonstrate the implementation of the snapshot POD a two dimensional velocity flow field is used. It is however important to point out that POD can be used on any flow field quantity.

The objective is to decompose a time-dependent velocity field snapshot $\mathbf{v}_m$ into a linear combination of spatial basis functions $\Phi = [\phi_1, \phi_2, ..., \phi_M]$ and time dependent coefficients $\mathbf{a} = [a_1, a_2, ..., a_M]^T$ (where M is the number of snapshots) such that the original velocity flow field can be reconstructed as $\mathbf{v}_m = \Phi a$. Firstly,

each snapshot $\mathbf{v}_m$ taken at time-step m is arranged into a matrix $\mathbf{V}_1^M$ such that:.

$$\mathbf{V_1^M} = \begin{bmatrix} \mathbf{v}_1 \\ \mathbf{v}_2 \\ \vdots \\ \mathbf{v}_M \end{bmatrix} = \begin{bmatrix} u^{(1)}_{i=1,j=1} & u^{(1)}_{i=1,j=2} & \cdots & u^{(1)}_{i=1,j=J} & u^{(1)}_{i=2,j=1} & \cdots & u^{(1)}_{i=I,j=J} \\ u^{(2)}_{i=1,j=1} & u^{(2)}_{i=1,j=2} & \cdots & u^{(2)}_{i=1,j=J} & u^{(2)}_{i=2,j=1} & \cdots & u^{(2)}_{i=I,j=J} \\ \vdots & \vdots & & \vdots & \vdots & & \vdots \\ u^{(M)}_{i=1,j=1} & u^{(M)}_{i=1,j=2} & \cdots & u^{(M)}_{i=1,j=J} & u^{(M)}_{i=2,j=1} & \cdots & u^{(M)}_{i=I,j=J} \\ v^{(1)}_{i=1,j=1} & v^{(1)}_{i=1,j=2} & \cdots & v^{(1)}_{i=1,j=J} & v^{(1)}_{i=2,j=1} & \cdots & v^{(1)}_{i=I,j=J} \\ v^{(2)}_{i=1,j=1} & v^{(2)}_{i=1,j=2} & \cdots & v^{(2)}_{i=1,j=J} & v^{(2)}_{i=2,j=1} & \cdots & v^{(2)}_{i=I,j=J} \\ \vdots & \vdots & & \vdots & \vdots & & \vdots \\ v^{(M)}_{i=1,j=1} & v^{(M)}_{i=1,j=2} & \cdots & v^{(M)}_{i=1,j=J} & v^{(M)}_{i=2,j=1} & \cdots & v^{(M)}_{i=I,j=J} \end{bmatrix} \tag{2.23}$$

Here $I \times J$ represents the number of total grid points in the velocity field. Then a spatial correlation matrix C, defined as $C = \frac{1}{M}(\mathbf{V}\mathbf{V}^T)$, is decomposed into a sum of weighted, linear, empirical basis functions (also called modes) Φ by minimizing the total reconstruction error while preserving the variance in the original data:

$$\left|\left|\mathbf{V}_1^{(M)} - \Phi\mathbf{a}\right|\right|^2 \rightarrow min \tag{2.24}$$

where $||\cdot||$ denotes the L^2 norm, Φ are the orthonormal modes and $\mathbf{a}$ are mode amplitudes.

This condition is realised by solving the singular value decomposition problem $C = \mathbf{U}\Sigma\mathbf{W}$. The energy of each mode in all snapshots is recorded in the diagonal matrix Σ and the corresponding POD modes are calculated by projecting the velocities onto the eigenvectors: $\Phi = \mathbf{V}^T\mathbf{U}$, and then normalising them. The coefficient matrix a containing the actual energy that each mode contributes to each snapshot can be generated by projection of each mode onto the corresponding snapshot: $\mathbf{a} = \mathbf{V}\Phi$. The resulting basis functions and corresponding coefficients can then be used to visualise coherent structures present in the data set. The Proper Orthogonal Decomposition is later used on the pressure component of the three-dimensional

wake flow-field to reveal the effects of bi-modality on the most energetic structures in the wake.

2.4.2 Dynamic Mode Decomposition

Another method popular for extracting coherent flow structures is the Dynamic Mode Decomposition (DMD) introduced by Schmid [104]. The algorithm is the numerical approximation of the linear but infinite-dimensional Koopman operator [61]. Spectral decomposition of the Koopman operator leads to a set of Koopman modes and eigenvalues which capture the evolution of observables describing any (even nonlinear) dynamical system [81]. While obtaining Koopman modes is not feasible for most systems, DMD provides an efficient approximation. Schmid applied the method to the flow over a square cavity, the wake behind a flexible membrane and the instabilities observed in experiments of a jet passing between two cylinders to successfully identify the unstable modes of the flow and visualise them. The DMD method has also been applied to the low Reynolds number bifurcation regime of a cylinder bluff body flow [5] showing that at low Reynolds numbers the DMD algorithm is capable of approximating the Koopman modes and thus providing a viable method of decomposing the flow into saturated and transient oscillatory modes. Unlike POD, which sorts coherent structures by energy and where each mode can exhibit different frequencies, the DMD algorithm produces a combination of modes, each oscillating at a specific frequency.

Unlike POD (which is based on spatial orthogonal framework) DMD represents the dominant flow features within a temporal orthogonal framework. The DMD algorithm approximates the data as a trajectory of a linear system, even if data was generated by a nonlinear process. DMD algorithm decomposes the flow field into oscillatory modes with a specific eigenvalue representing the growth/decay rate and frequency of the mode. Therefore DMD provides insight into coherent structures and their temporal evolution. Similar to the POD approach, first the snapshots

$\mathbf{v}_m$ from each from time-step m need to be arranged into matrix $\mathbf{V}_1^M$ such that $\mathbf{V}_1^N \leftarrow \{\mathbf{v}_1, \mathbf{v}_2, ...\mathbf{v}_N\}$. The data matrix $\mathbf{V}_1^N$ is then decomposed into two sets: $\mathbf{V}_1^{N-1} \leftarrow \{\mathbf{v}_1, \mathbf{v}_2, ...\mathbf{v}_{N-1}\}$ and $\mathbf{V}_2^N \leftarrow \{\mathbf{v}_2, \mathbf{v}_2, ...\mathbf{v}_N\}$, and the first set orthogonalised using the singular value decomposition (SVD): $[\mathbf{U}, \mathbf{\Sigma}, \mathbf{W}] = svd(\mathbf{V}_2^{N-1})$. Here the matrix $\mathbf{U}$ contains proper orthogonal modes of the first set of data $\mathbf{V}_1^{N-1}$. It is thus possible to express the last data vector $\mathbf{v}_N$ as a linear combination of the previous elements in the form:

$$\mathbf{S} = \mathbf{U}^H \mathbf{V}_2^N \mathbf{W} \mathbf{\Sigma}^{-1} \tag{2.25}$$

The eigenvectors of $\mathbf{S}$ are the modal structures and the eigenvalues contain information about the frequencies (imaginary part) and growth/decay rates (real part). To quantify how much the modes are represented in the original dataset, the optimum amplitudes are computed using the QR-decomposition of the product of the original data matrix $\mathbf{V}$, the singular values $\mathbf{\Sigma}$ and the modes, i.e. the eigenvectors of $\mathbf{S}$.

The resulting DMD modes contain information about coherent structures tied to a frequency and their temporal evolution. This approach is becoming increasingly popular in analysing complex flows and identifying emerging and saturated oscillating flow dynamics because it is computationally cheap and can be applied to really large data sets. This decomposition is later employed in the thesis to gain insight into spatial and temporal distribution of structures in the wake and analyse effects of the feedback controller on the flow.

To summarise both algorithms in a comparison: POD uses spatial orthogonal framework to extract the most energetic flow features by projecting low-dimensional modes onto the flow, while DMD extracts temporal evolution of the modes using temporal orthogonal framework. POD retains all nonlinear dynamics of the system and offers insight into spatial distribution of energy modes. DMD approximates the

Koopman operator that in turn best approximates the nonlinear dynamics of the system and allows to obtain temporal evolution of the modes. Both methods are computationally efficient and can be applied directly to simulation or experimental results, without the need for the governing equations.

Chapter 3

Laminar Ahmed Body Flow

The first investigation in this doctoral work is concerned with the Ahmed body flow and onset of bi-stable behaviour at low Reynolds numbers based on height H between $Re_H = 310$ and $Re_H = 435$. Similar to many other bluff bodies with fixed separation, symmetry breaking first occurs at low, laminar Reynolds numbers. This has been predicted by weakly nonlinear analysis of the Navier-Stokes equations in [80] and has been observed experimentally in [44, 100]. Since the symmetry breaking behaviour persists to the turbulent regime [112, 45, 46], an investigation of this behaviour at low Reynolds numbers is highly relevant to the wake dynamics at turbulent Reynolds numbers.

The recent experimental study of Grandemange et. al. [44] investigated the flow past the Ahmed body where the authors identified a scenario of symmetry breaking bifurcations as the Reynolds number increases. Below $Re_H = 365$ the Ahmed body wake is steady and symmetric. Then at $Re_H = 365$ the Ahmed body wake changes from steady symmetric to unsteady. Then after a brief transient state, during which the flow is symmetric, the wake flips to one side and becomes steady and asymmetric. As the Reynolds number is increased past $Re_H = 415$ the wake again becomes unsteady, but maintains asymmetry. These findings from [44] are summarised in figure 3.1.

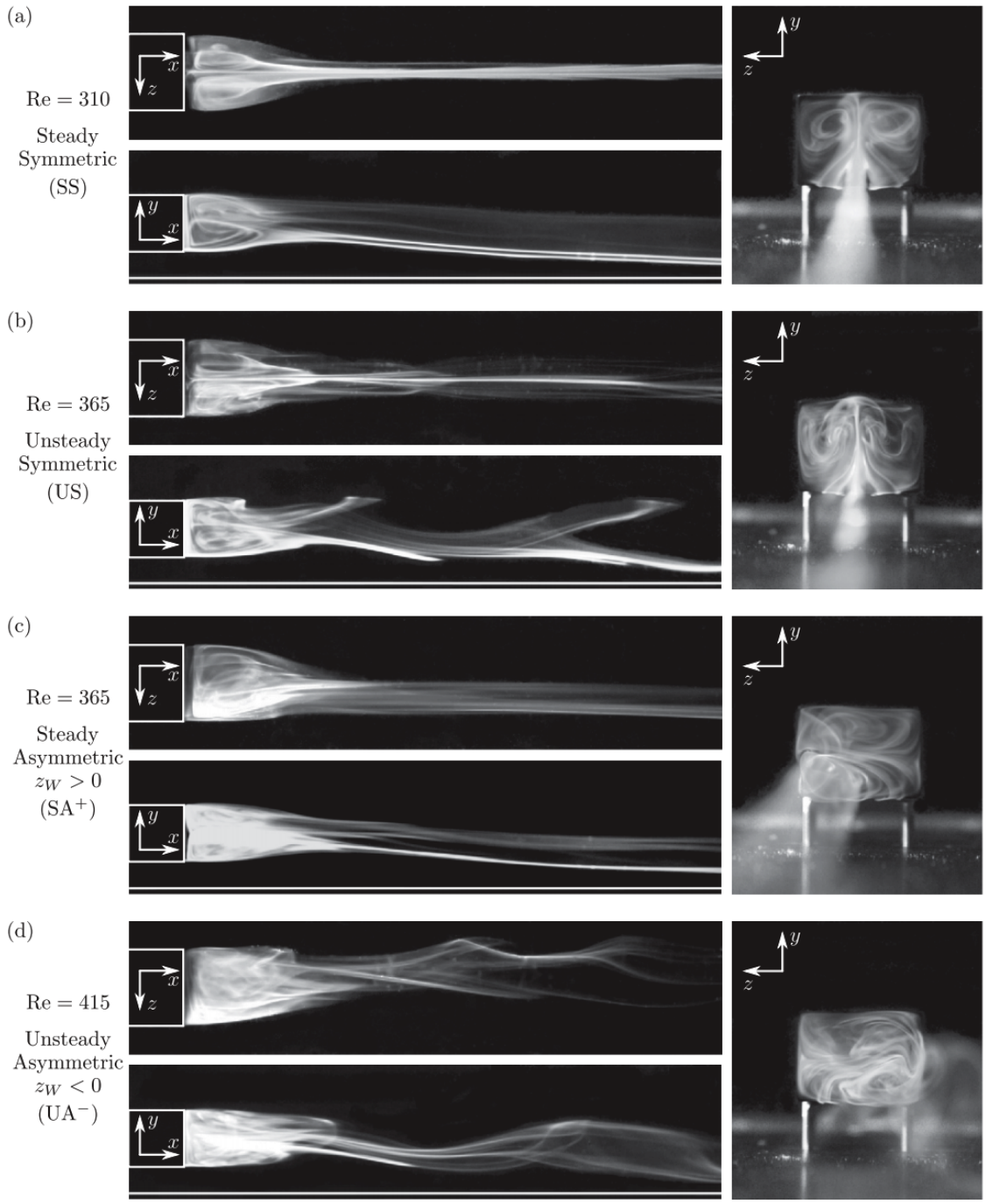


Figure 3.1: Flow visualizations at the Reynolds numbers *a)* $Re_H = 310$, *b)* and *c)* $Re_H = 365$, and *d)* $Re_H = 415$ from the experimental study by Grandemange et. al. [44]. For each Reynolds number: Top picture, top view; bottom picture, side view; right picture, rear view. The flow comes from the left for both top and side views.

Investigations into the symmetry breaking of blunt bluff body wakes has, so far, been primarily experimental, supplemented by modelling. No numerical studies have thus far identified these symmetry breaking states. In this chapter we present the first numerical investigation into the sequence of symmetry breaking bifurcations at low Reynolds numbers, successfully reproducing the experimental results of [44] in figure 3.1. With the access to the full three-dimensional flow-field, we are able to study the destabilising dynamics associated with symmetry breaking of the wake in more detail providing further insight into wake topology. Finally, a sensitivity-based feedback control strategy to reduce the form-drag of the Ahmed body is implemented.

The results presented in this chapter are a modified and extended version of the work published in a recent Journal of Fluid Mechanics Rapids article [31]. These results have also been presented at the 68th Annual Meeting of the American Physical Society's Division of Fluid Dynamics in Boston, MA, USA (2015), AEROVEHICLES 2 in Göthenburg, Sweden (2015) and UK Fluids Conference at Imperial College London, UK (2016).

3.1 The Test-Case

The Ahmed body used in this chapter exactly replicated the dimensions, aspect ratio and the ground clearance used by Grandemange et. al. in their work in [44] (figure 3.2). In this case the ground clearance is $C^* = \frac{C}{W} = 0.44$ and the aspect ratio is $H^* = \frac{H}{W} = 0.73$ which means that we expect to see displacement in the wake in the horizontal direction as shown in figure 3.3.

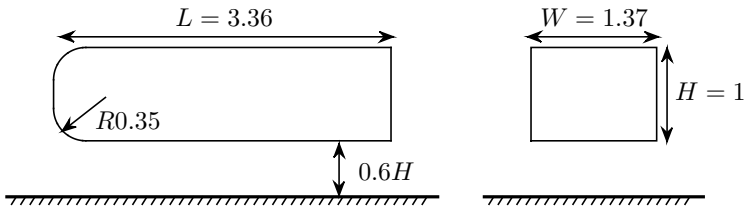


Figure 3.2: Schematic of square-back Ahmed body: (a) side view ; (b) rear view. For this test case $H^* = \frac{H}{W} = 0.73$ and $C^* = \frac{C}{W} = 0.44$.

The computational domain dimensions were set to have the following proportions: $\Omega_{AB} = (L_i, L_x, L_y, L_z) = (2L, 8L, 2L, 2L)$ where L_i is the inlet length and L_x, L_y and L_z are lengths in $x-$, $y-$ and $z-$directions and L is the body length. The domain extends at least five body lengths behind the Ahmed body to ensure that all scales of motion that are present in the flow are captured. The width and the height of the domain are set to two body lengths. The domain dimensions chosen here are consistent with the recommendation by ERCOFTAC [77, 56]. The domain was discretised into a cartesian structured grid with approximately 5.3 million computational nodes. The majority of the nodes are clustered around the body and in the wake to ensure the important flow dynamics are resolved. The details of the grid can be seen in figure 3.4. The largest skew of 0.6 (defined as $[max\left[\frac{\theta_{max}-90}{90}, \frac{90-\theta_{min}}{90}\right]]$, where θ is an angle between element edges) is found near the nose of the body; this is well within the accepted range as the skew for quadrilateral elements should not exceed 0.85. The maximum expansion ratio between adjacent cells is ≈ 1.04. For all simulations y^+ is less than 1 all around the body, as can be seen in figure 3.5, and the maximum Courant-Friedrichs-Lewy (CFL) number is 0.08, ensuring that the flow is spatially and temporally resolved. It should be noted that when a

	Nodes adjacent to body	C_d	St_H	Recirculation length
Nominal grid - no SGS	19,584	0.288	0.082	1.949H
Nominal grid - with SGS	19,584	0.308	0.081	1.949H
Fine Grid - with SGS	40,960	0.299	0.088	1.951H

Table 3.1: Grid comparison for simulations at $Re_H = 435$

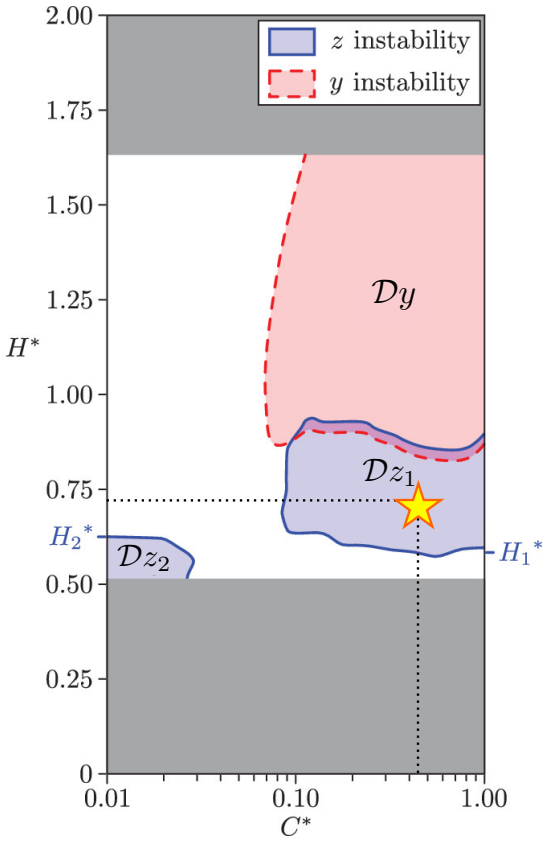


Figure 3.3: Regions of bi-modality (defined by the pressure gradient) as a function of ground clearance $C^* = \frac{H}{W}$ and aspect ratio $H^* = \frac{H}{W}$. The yellow star indicates the behaviour expected to be observed for the current test-case.

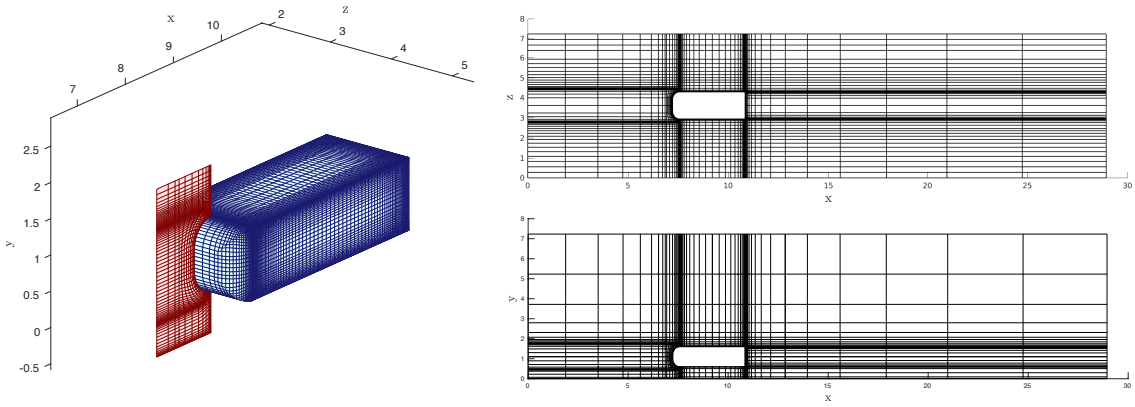


Figure 3.4: Structured grid used in the computations. Left: Grid in the vicinity of the nose (red) and around the body (blue). Right: horizontal and vertical slices through the domain, showing every 4^{th} node.

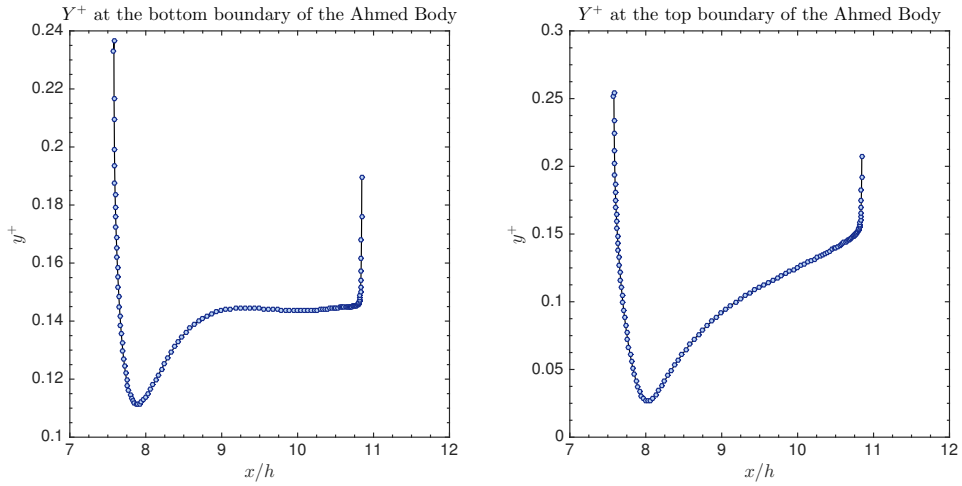


Figure 3.5: y^+ along the centerline of the south and north sides of the Ahmed body

simulation at $Re_H = 435$ was performed without the SGS model, there were few changes to the flow-field as can be seen in table 3.1. A comparison of body drag, recirculation bubble length (measured at the free stagnation point in the wake of the Ahmed body) and the dominant unsteady frequency for simulations on the fine (12.5 million nodes) and nominal (5.3 million nodes) grids in table 3.1 suggests that the simulations are sufficiently well-resolved. Since all simulations at low Reynolds numbers $310 \leq Re_H \leq 435$ ran on the same grid, the grid checks were performed only for the highest Reynolds number of $Re_H = 435$

The simulations used 384 cores and ran on Imperial College London's HPC High-End parallel cluster called CX2, and on the ARCHER UK National Supercomputing Service. All unforced and open-loop simulations ran for 800 convective time units, allowing to record the ≈ 34 occurrences of the lowest frequency in the unforced wake after the initial transient state. The feedback control simulations ran for less time as these simulations required a smaller static time step to ensure good resolutions. Approximately 600 convective time units were obtained, allowing to record ≈ 23 occurrences of the lowest frequency in the unforced wake after the transient state.

3.2 Unforced Flow

3.2.1 Topologies of the Laminar Wake

The changes in the mean position of the wake Z_w in the z-direction, observed in the numerical simulations as Reynolds number was increased, are shown in the bifurcation diagram in figure 3.6, alongside the experimental findings of [44]. Here Z_w was measured at the point where the averaged streamlines met in the far wake to create a trail. The simulations successfully capture the sequence of regimes identified experimentally, although small differences in the Reynolds numbers of the state changes are noted. For example, at $Re_H = 415$, the simulated wake is steady asymmetric, while experiments report an unsteady asymmetric wake. However once the simulation Reynolds number is increased to $Re_H = 435$ the wake becomes unsteady asymmetric.

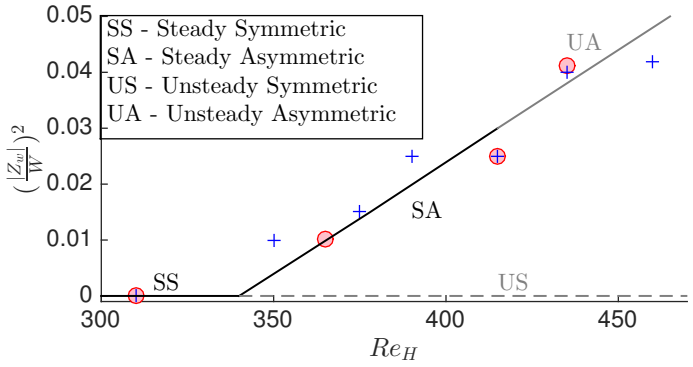


Figure 3.6: Bifurcation scenario of changes in the mean position of the wake in the z-direction (Z_w) as the Reynolds number is varied between $310 \leq Re_H \leq 435$. LES results (red circles) are compared to experimental results from [44] (blue crosses). Black and grey lines show steady and unsteady regimes respectively. Z_w was measured as the point where the averaged streamlines met in the far wake to create a trail.

The four states exhibited by the wake at different Reynolds numbers are shown in figure 3.7. At $Re_H = 310$, the wake is 'steady symmetric' and consists of two recirculating regions aligned horizontally next to one another, as shown in the three-dimensional streamlines on the right. The streamlines projected onto the 'side-view'

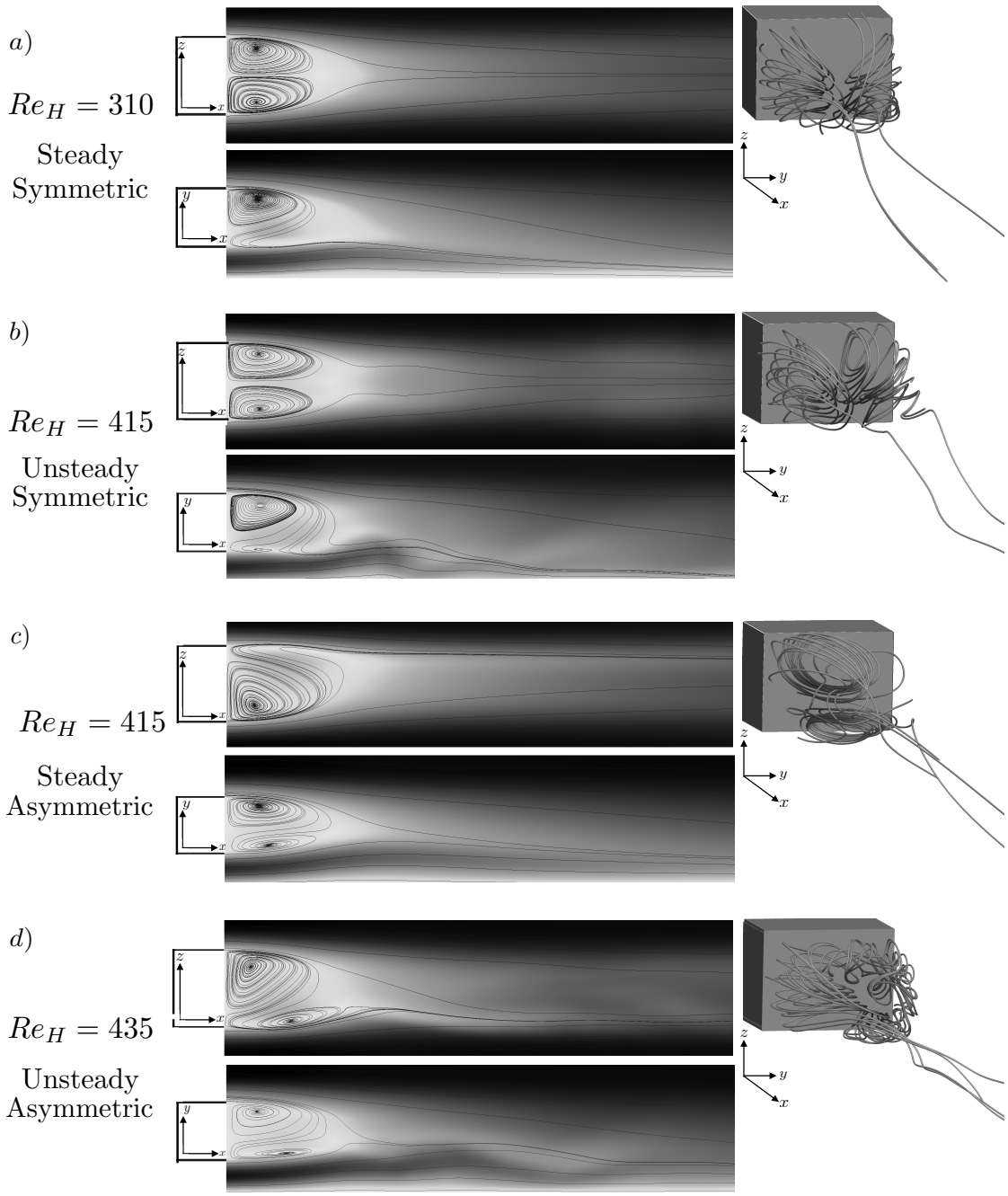


Figure 3.7: Visualisations of Ahmed Body flow at Reynolds numbers (*a*) $Re_H = 310$, (*b*) and (*c*) $Re_H = 415$, (*d*) $Re_H = 435$. For each Re_H the top and bottom left pictures show side view and top view respectively of a 2D slice with streamlines projected onto it; the right picture shows 3D streamlines in the wake.

slice of the flow field show that the separated flow travels past the top edge of the Ahmed Body and recirculates back towards the body base, where it interacts with the underbody flow. Due to the viscous effects of the fluid and the thick boundary layer on the ground, the underbody flow is under developed. As a result there is insufficient shear created at the bottom edge of the Ahmed body to initiate recirculating motion. As the Reynolds number is increased to $Re_H = 415$, the wake becomes 'unsteady symmetric'. This is a transient state and after a few flow-throughs the wake flips to the right, becoming 'steady asymmetric'. It is noteworthy that compared to 'steady symmetric' regime, the 'unsteady symmetric' wake visibly shows a more active bottom shear layer, with recirculating motion beginning to form at the bottom edge. As the flow settles into the 'steady asymmetric' state, two recirculating regions form, which are now aligned vertically one on top of the other. This suggests that the initial symmetry breaking occurs once the Reynolds number is sufficiently high to create enough underbody flow for the top and bottom shear layers to interact and recirculate back towards the base. This further corroborates observations in [6] and [45] that ground presence affects the boundary layer development along the lower surface of the body and thus influences the onset of transverse asymmetry in the wake. It is further postulated that when the wake is symmetric, the two recirculating regions located horizontally side by side originate from the side shear layers interacting - a relationship that is broken at higher Reynolds numbers due to strong bottom shear layer and the aspect ratio of the base (the top and bottom shear layers are closer to one another than the side shear layers). As the Reynolds number is increased further to $Re_H = 435$, the wake becomes 'unsteady asymmetric', with the two recirculating regions maintaining their vertical position. Overall it is possible to see that the numerical results presented here are in good agreement with the experimental results presented in figure 3.1. The simulations successfully capture the sequence of regimes identified experimentally and allow study of the flow in more detail. However, some small differences in the Reynolds

numbers of the state changes are noted. For example, at $Re_H = 415$, the simulated wake is steady asymmetric, while experiments report an unsteady asymmetric wake. However once the simulation Reynolds number is increased to $Re_H = 435$ the wake becomes unsteady asymmetric.

It should be noted, that at these Reynolds numbers the wake did not exhibit switching between asymmetric states, but remained in a single chosen asymmetric position. When the wake becomes unsteady, it maintained the same asymmetric position (the switch usually observed at higher turbulent Reynolds number was not observed) for the duration of the simulation. Similar lack of switching was reported in the experiments by Grandemange et. al. [44]. This could suggest that while the asymmetry is inherent to this type of flow, the switch between the two asymmetric states manifests when the boundary layer is turbulent and thus there is enough energy in the flow to trigger the flip.

Further insight into the unsteady symmetric and unsteady asymmetric states is provided by considering the Q-criterion [55] of the flow fields conditionally averaged at the same point in the shedding cycle and shown in figure 3.8. When the flow is symmetric, the internal vortex structure is positioned at the centre of the bottom edge of the base. As the symmetry breaks, the vortex structure inside the vortex ring changes its position. Once the wake shifts to the side, the vortex inside the recirculation bubble moves to the side edge of the base, subsequently affecting the position of the large recirculating structures further downstream.

The drag and lift coefficients associated with each of the simulated Reynolds numbers are listed in table 3.2. The drag is higher for the Reynolds numbers associated with the symmetric wake, while the asymmetric wake yields lower drag coefficients. The drag coefficient at $Re_H = 435$ is 0.308, falling within the range reported in the literature of 0.26 – 0.36 [43, 2, 112]. An increase in lift coefficient is also observed as the Reynolds number increases, which is consistent with an increased underbody flow developing and thus affecting the wake by shifting its

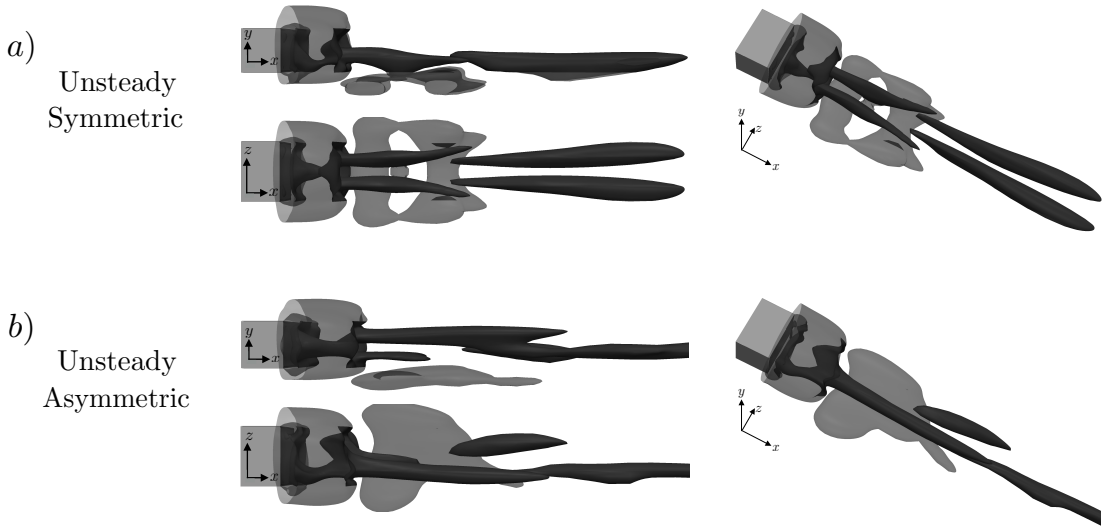


Figure 3.8: Q-criterion iso-contour of Ahmed Body flow at Reynolds number $Re_H = 435$ when the wake is (a) unsteady symmetric wake, (b) unsteady asymmetric wake, where the asymmetry is locked to one preferred position, no switch between the two asymmetric states was observed. For each regime, the top and bottom left pictures show side view and top view respectively; the right picture shows the diagonal view from the top. The same positive Q-criterion iso-contour is plotted with opaque and transparent parts to reveal the internal structure of the vortex ring in the wake.

location slightly upwards. The lift coefficient for $Re_H = 435$ compares well with the value reported in [43] of $C_l = -0.04$.

Re_H	State	C_d	C_l
310	Steady symmetric	0.353	-0.053
365	Unsteady symmetric	0.325	-0.049
415	Steady asymmetric	0.313	-0.042
435	Unsteady asymmetric	0.308	-0.038

Table 3.2: Drag and lift coefficients at different symmetry-breaking states

3.2.2 Dynamics of the Laminar Wake

Considering the spectra of the base pressure signal it is possible to track the evolution of the dynamics of the wake. Unsurprisingly, the spectrum at $Re_H = 310$ (figure 3.9 *(a)*) does not show any significant dynamics; the flow at that Reynolds number is steady, which is reflected in the base pressure signal spectrum. There are some small

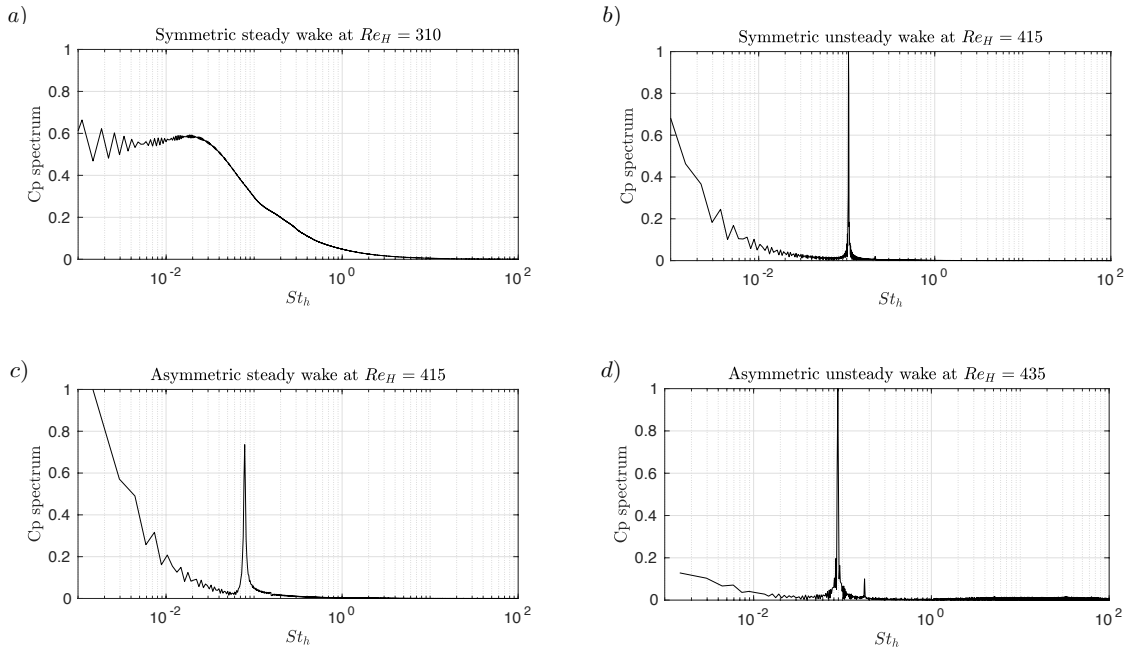


Figure 3.9: Amplitude of base pressure force spectrum for the Ahmed body flow at *a)* $Re_H = 310$ - steady symmetric wake, *b)* $Re_H = 415$ - unsteady symmetric wake, *c)* $Re_H = 415$ - steady asymmetric wake, and *d)* $Re_H = 435$ - unsteady asymmetric wake.

peaks at high frequencies, which are not physical and appear due to numerical noise. Then as the Reynolds number is increased to $Re_H = 415$ the wake, at first, becomes unsteady symmetric and the spectrum reveals frequency of $St_H \approx 0.1$ (figure 3.9 *(b)*). After a few flow throughs the wake returns to steady state but shifts to an asymmetric position and the dominant frequency peak in the spectrum settles at $St \approx 0.08$ as can be seen in figure 3.9 *(c)*. For the flow at $Re_h = 435$ when the wake is unsteady and asymmetric the two dominant frequencies in the base pressure spectrum are $St_H \approx= 0.09$ and $St_H \approx 0.18$. It appears that once the Reynolds number is high enough for the bubble pumping motion to occur, the wake starts to exhibit asymmetric behaviour.

A common way to visualise bi-modal behaviour is to use pressure gradients on the base in horizontal ($\partial C_p/\partial z$) and vertical ($\partial C_p/\partial y$) directions. In this work the gradients were computed by recording base pressure force signal averaged over

each half of the base and computing their difference, as shown in figure 3.10. The resulting signal allows to see if there is a concentration of pressure deficit on either side of the base. In case of the flow past an Ahmed body at $Re_H = 435$ these

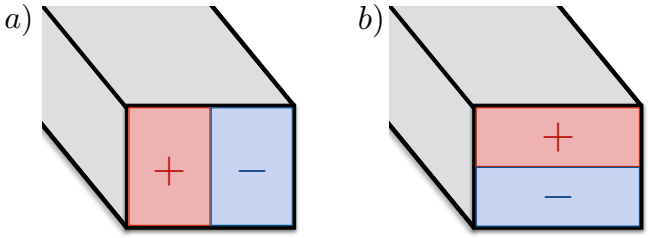


Figure 3.10: The a) horizontal and *b)* vertical pressure gradients: $\frac{\partial C_p}{\partial z}$ and $\frac{\partial C_p}{\partial y}$ respectively, are computed by recording separate base pressure signals averaged over blue and red regions and computing their difference.

gradients can be used to gain further insight into how the wake transitions to a symmetry breaking regime from the transient state. Figure 3.11 shows that initially the wake is positioned towards the bottom of the base, but centred in the horizontal direction. After around 200 time units the horizontal symmetry breaks and the wake is displaced to one side. Simultaneously the wake travels slightly upwards, however due to ground effects remains just below the vertical base center.

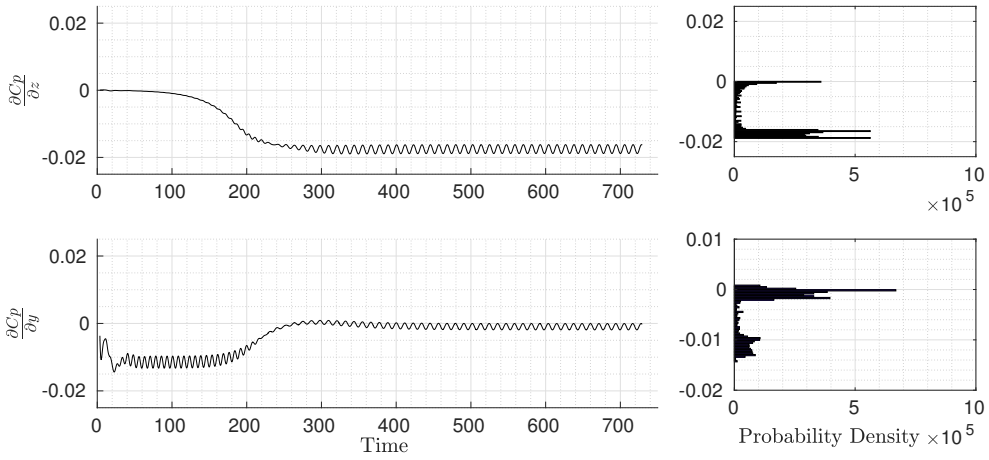


Figure 3.11: Right: Base pressure gradients for the Ahmed body flow at $Re_H = 435$. Left: Probability Density of the base pressure gradient signal.

3.2.3 Ground Effects

Grandemange [42] previously considered the effects of smaller ground clearances on the Ahmed body wake at laminar Reynolds numbers. Using a water tunnel two more ground clearances were tested: $C^* = C/H = 0.4$ and $C^* = C/H = 0.2$. Grandemange found that at $C^* = 0.2$ the unsteady transition only occurs at $Re_H = 450$ (for $C^* = 0.6$ the authors reported the unsteady transition at $Re_H = 365$), but the wake remains symmetric in the considered Reynolds number range. When the ground clearance is increased to $C^* = 0.4$ the first transition from steady symmetric to unsteady symmetric regime is observed at $Re_H = 380$. The wake remains unsteady symmetric until $Re_H = 440$ after which it transitions to unsteady asymmetric (for comparison: for $C^* = 0.6$ the asymmetry developed at $Re_H = 365$). The steady asymmetric state was by-passed altogether for $C^* = 0.4$ ground clearance case. Grandemange, thus, convincingly demonstrated that the ground has a stabilising effect, suppressing or delaying the onset of wake asymmetry.

To investigate further the influence of the ground on the wake and bi-modal dynamics, three more cases are considered in this thesis: Ahmed body at $Re_H = 310$ and $Re_H = 435$ without the ground and Ahmed body at $Re_H = 435$ with moving floor.

Simulations without ground

To compute the flow past the Ahmed body without the ground a new grid was generated. The domain size was kept the same, but the body was centred with respect to vertical axis with a free-slip boundary condition imposed at the bottom boundary of the domain. The mesh was discretised using 8.6 million computational nodes with maximum skew of 0.63 near the nose and $y^+ < 1$ all along the body boundaries. The results from the simulations are presented in figures 3.12 and 3.13. For the $Re_H = 310$ case in figure 3.12 it is possible to observe that the

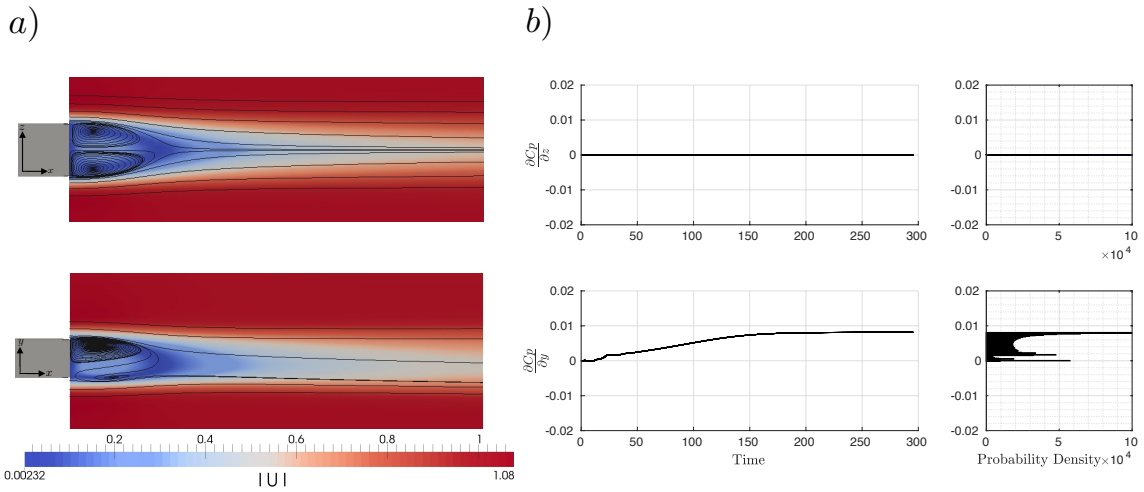


Figure 3.12: Results from simulations of Ahmed body flow at $Re_H = 310$ with no ground. *a)* Horizontal (top) and vertical (bottom) 2D slices through the instantaneous velocity flow field recorded at $T^* = 588$ with streamlines projected onto the slice. *b)* Horizontal (top) and vertical (bottom) base pressure gradient

flow is steady throughout the simulation. Initially the wake is symmetric in both vertical and horizontal directions. Then, the flow becomes vertically asymmetric and shifts upwards, where it remains for the remainder of the simulation. No horizontal asymmetry is observed for the duration of simulation at $Re_H = 310$.

The flow without the ground at $Re_H = 435$ is unsteady and almost immediately asymmetric, moving upwards in the vertical direction after around 60 convective time units. Similar behaviour was observed in the case with stationary ground at $Re_H = 435$ (figure 3.11), but the wake moved downwards due to the ground influence. It appears that without the ground influence the wake is initially free to explore all four reflectional-symmetry breaking states (2 in vertical and 2 in horizontal planes). Then after a few cycles (at around 310 convective time units) the wake begins to shift in the horizontal direction away from the base center while returning to center in the vertical direction. Two-dimensional slices in figure 3.13 *b)* taken at $T^* = 300$ and $T^* = 685$ show the wake exploring different possible switching scenarios. It has not, however, been observed during the simulations for the wake to be asymmetric in both vertical and horizontal directions simultaneously.

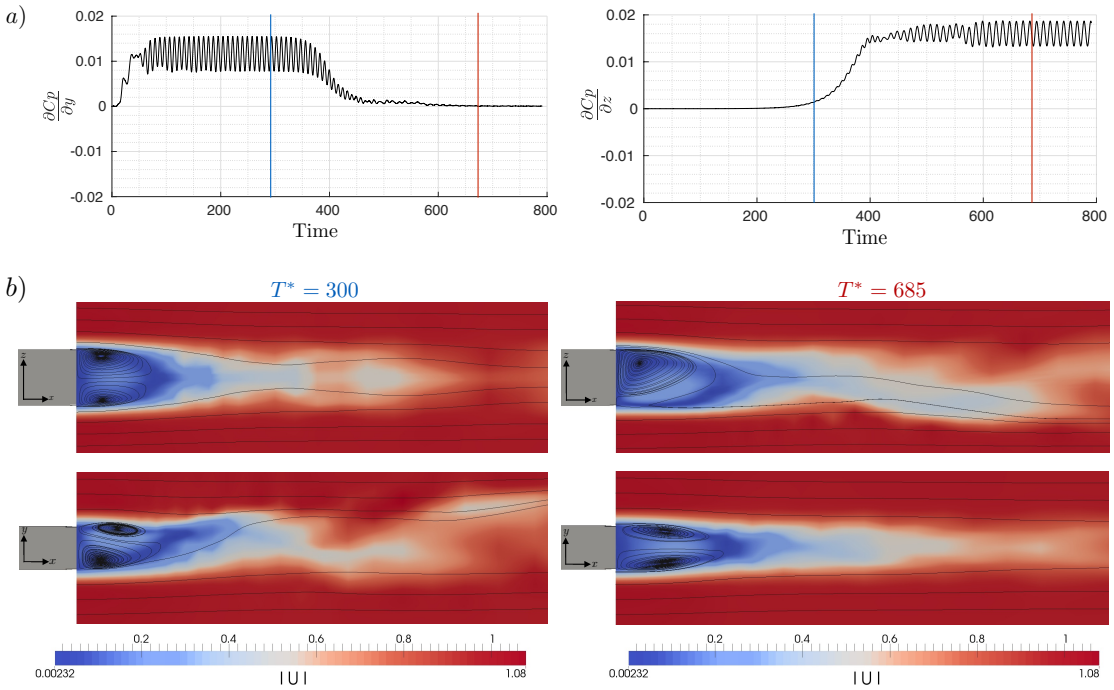


Figure 3.13: Results from simulations of Ahmed body flow at $Re_H = 435$ with no ground. *a)* Vertical (left) and horizontal (right) base pressure gradients. *b)* two-dimensional slices (top - horizontal; bottom - vertical) through the velocity flow field recorded at $T^* = 300$ and $T^* = 685$ with streamlines projected onto the slices.

Moving floor simulations

Simulations of the flow past the Ahmed body with the moving ground were conducted on the original nominal grid. The moving floor was imposed as a no-slip boundary condition on the bottom boundary of the domain, but the non-dimensional u-component of the velocity of the lower boundary was set to 1. The moving boundary condition was initially implemented in *StreamLES* by Agostini et. al. [1] and the same approach was used in this work.

The results from the simulation with the moving floor are presented in figure 3.15 The flow appears to be more unsteady when the ground is moving which is reflected in the fluctuations about the mean of the base pressure force signal. When the floor is moving the fluctuating component is $rms(C_p - \overline{C}_p)_{moving} = 0.0084$ and for the simulations with the fixed ground the fluctuating component is $rms(C_p - \overline{C}_p)_{fixed} = 0.0011$. The wake when the ground is moving exhibits similar dynamical

features as when the ground is stationary, which is reflected in the base pressure force spectrum in figure 3.14. It is possible to see that the frequencies in both simulations are identical at $St_H = 0.09$ and $St_H = 0.18$.

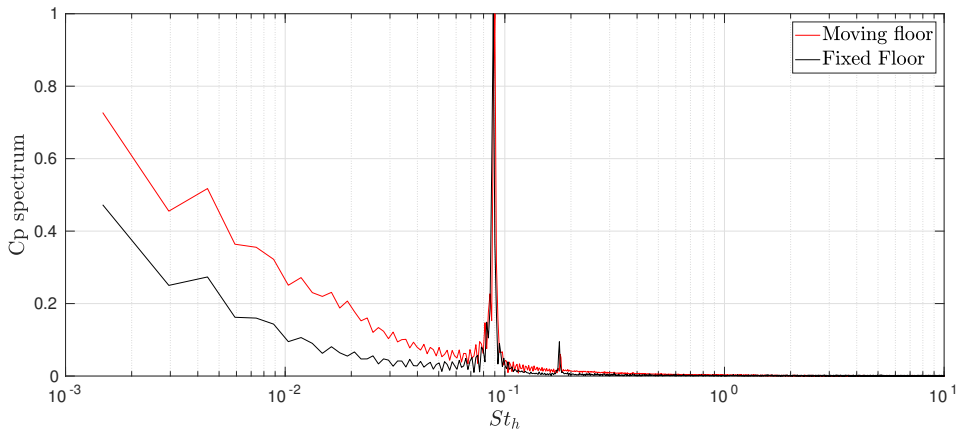


Figure 3.14: Normalised base pressure force signal from simulations with stationary floor and moving floor.

The transition to a horizontal symmetry breaking regime is also similar: the wake starts with a transient state as unsteady symmetric and after a few flow-throughs flips to the side. As in the case with fixed floor, the ground influence is observed in the vertical pressure gradient in figure 3.15 *b)* throughout the simulation: the wake starts off positioned closer towards the ground in the vertical plane, then as the flow develops the wake shifts upwards, but still remains below the center of the base. The main difference in the dynamical features of the flow between two configurations is that the wake appears to be convected downstream faster when the ground is moving due to increased underbody flow. As a result the recirculation region is much longer, as can be seen in figure 3.16 showing iso-surface of the u-component of the velocity at 0.

Effects on the body forces

The body forces recorded during the different simulations are considered in the table 3.3. When there is no ground, the drag is significantly decreased compared to the

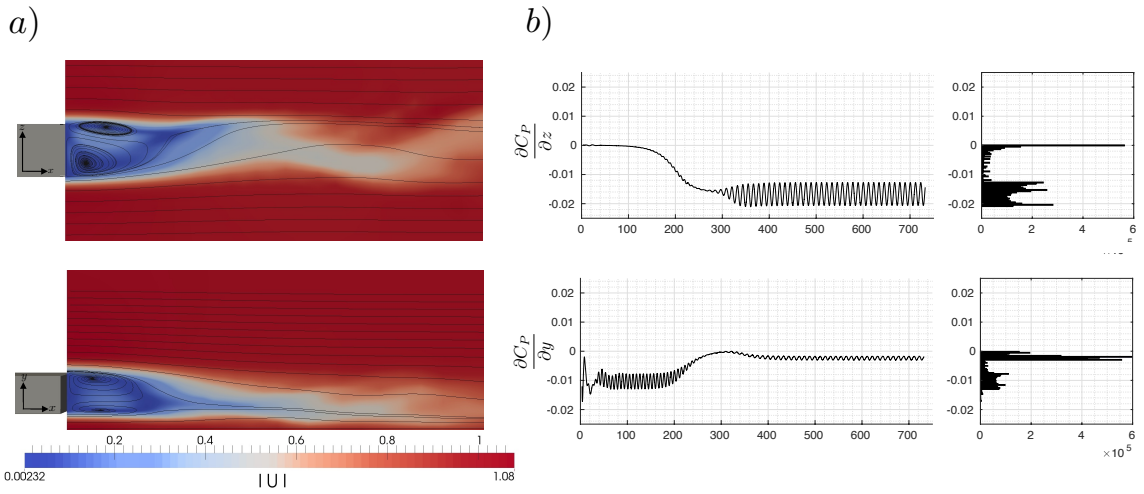


Figure 3.15: Results from simulations of Ahmed body flow at $Re_H = 435$ with moving ground. *a)* Two-dimensional slices (top - horizontal; bottom - vertical) through the velocity flow field recorded at $T^* = 729$ with streamlines projected onto the slices. *b)* corresponding base pressure gradients.

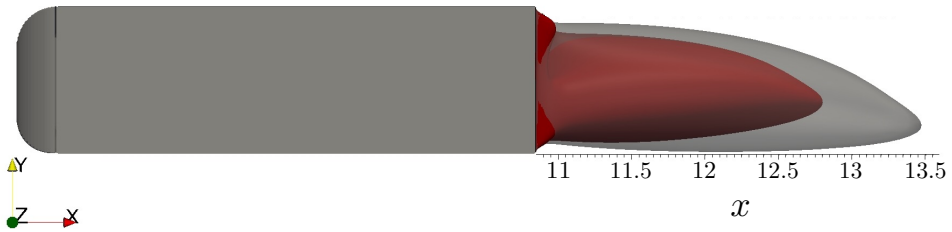


Figure 3.16: iso-surface contour at $u = 0$ visualising the recirculation regions when the ground is stationary (red) and when the ground is moving (opaque grey).

case with stationary ground. The drag value is consistent with studies that considered similar blunt bluff body geometries at large ground clearances [14, 25]. As expected, the lift force is close to zero, exhibiting only negligible downforce. This confirms that there should be no ground effects influencing the flow or orientation of the wake in the vertical plane. The drag is also smaller in the case with moving ground. This is consistent with findings by Cooper et. al. [21] and [7] who experimentally investigated the effects of moving floor on body forces of simplified blunt vehicles without wheels. The difference in drag values could be explained by a significantly larger recirculation region when the ground is moving, where the whole

Re_H	Ground	C_d	C_l
310	none	0.238	-0.006
435	none	0.219	-0.008
435	moving	0.240	-0.032
435	**stationary**	**0.308**	**-0.038**

Table 3.3: Drag and lift coefficients in simulations with no ground and moving ground, compared to the nominal test case with stationary ground (in bold).

low pressure region at the rear is spread over a larger area, leading to an increase in the pressure immediately on the base. There is also a decrease of 16% in the amount of downforce acting on the Ahmed body when the floor is moving compared to the fixed floor case.

3.3 Open-Loop Forcing

In this section the flow at Reynolds number based on height $Re_H = 435$ is actuated using harmonic open-loop forcing at a range of forcing frequencies St_f from $0.004 \leq St_f \leq 0.5$, and forcing amplitudes $A_j = 0.1$ and $A_j = 0.2$. The frequency range of $0.004 \leq St_f \leq 0.5$ was chosen to include the key frequencies identified in the unforced base pressure signal spectrum at $Re_H = 435$ in figure 3.17.

The overarching goal of performing open-loop forcing is to collect data for system identification - a process by which the phase and gain shift of the pressure signal is measured in response to actuation at different levels. Then based on this data a lower-order model is constructed and used as basis for feedback controller design in section 3.4. For the control strategy to be feasible in real-life environments body-mounted sensing and actuation are used. The sensor signal is the unsteady component of the base pressure force, while actuation takes the form of unsteady synthetic jets acting uniformly around the perimeter of body, just ahead of the separation. The jets are angled at 10° outwards from the body base and are directed downstream. It is postulated that this actuation set-up allows some control authority

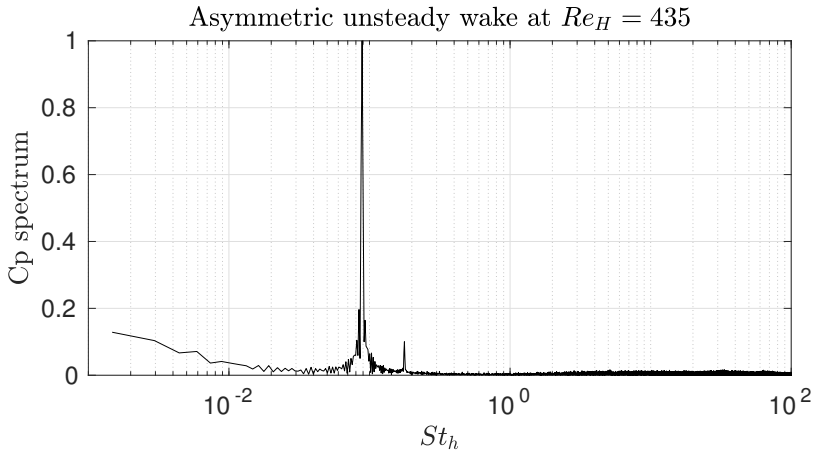


Figure 3.17: Amplitude force spectrum of the base pressure signal of the Ahmed body flow at $Re_H = 435$ clearly revealing key frequencies at $St_H \approx 0.09$ and $St_H \approx 0.18$, matching those in the literature as per chapter 1.2.1.

in the shear layers, while taking advantage of the benefits of downstream periodic forcing previously observed in the experimental study by Oxlade et. al. [88] for axisymmetric blunt bluff bodies. The schematic of the control arrangement is shown in figure 3.18.

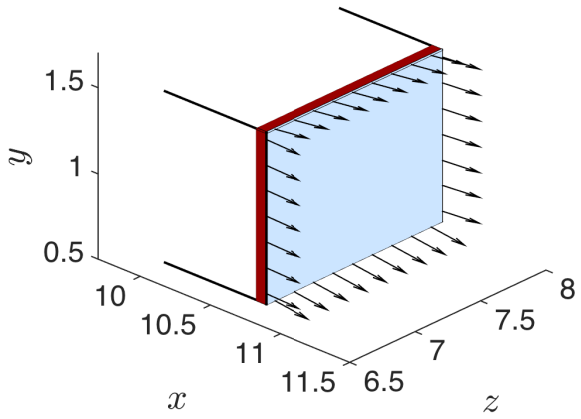


Figure 3.18: Schematic of the control arrangement: sensor (light blue) measures the base pressure force and actuation (red) acts via synthetic jets angled at 10° away from the body pointing downstream.

In the simulations the actuation is applied by imposing a time-varying velocity boundary condition with a flat profile at the jet orifice location. The jet cavity

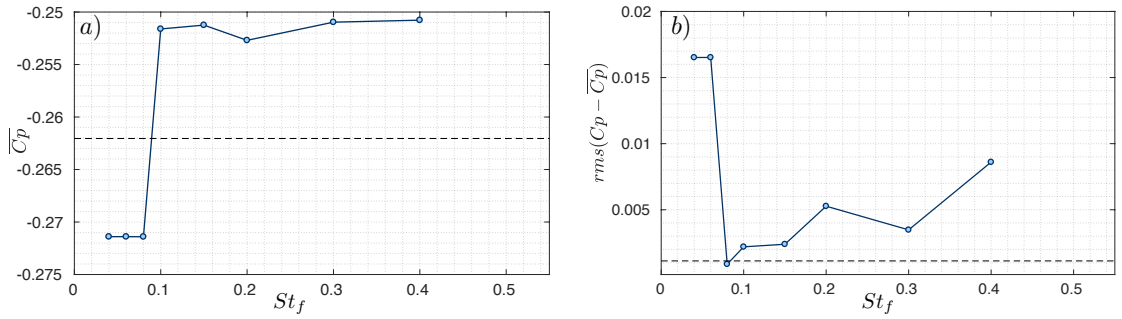


Figure 3.19: Effect of harmonic open-loop forcing at $A_j = 0.1$ and different forcing frequencies St_f on *a)* the time-averaged base pressure coefficient and *b)* the RMS value of the base pressure fluctuations. The dashed line represents the unforced value.

itself is not resolved in favour of keeping simulations more computationally economical. It has been previously shown by Leschziner et. al. [66] that in the context of numerical simulations, the details of the slot jet cavity are less critical than for round jets. Another numerical study by Utturkar et. al. [110] considered various designs of the synthetic jets and also found that the wide-ranging modifications to the jet cavity had limited effect on the jet exit flow. Therefore, in this case the modelling of the synthetic jets has been simplified. The total jet velocity is set to $U_{jet}(t) = A_j sin(2\pi St_f)$ where A_j is the amplitude of the harmonic forcing and St_f is the frequency of the jet. It is important to understand the amount of effort needed for the jets to implement the change to the flow. This is often quantified using the momentum coefficient $c_\mu = U_{jet}^2 A_{jet}/A_{base}U_\infty^2$ [4] - a measure of excitation imposed during active control. Here A_{jet} is the total area of the synthetic jets and A_{base} is the base area. For the highest forcing amplitude of $A_j = 0.2$, the momentum coefficient is $c_\mu = 1.37 \times 10^{-5}$. For comparison table 3.4 shows momentum coefficients reported in other studies which used synthetic jets at separation to implement feedback control to bluff body flows. It is possible to see that current configuration compares favourably with the previous studies and thus the controller is expected to be efficient.

Re_H	Geometry	c_μ	Reference
20,000	3D backward-facing step (BFS)	1.2×10^{-4}	Dahan et. al. in [23]
40,000	3D backward-facing step (BFS)	3.4×10^{-5}	Dahan in [22]
20,000	3D D-body	2.60×10^{-4}	Dalla Longa et. al. [24]
2,000	3D BFS with side walls	3.0×10^{-3}	Flinois [34]

Table 3.4: Momentum coefficients reported in other studies using active flow control on blunt bluff bodies All these studies actuated the flow using synthetic jets angled at 45° degrees to the downstream flow.

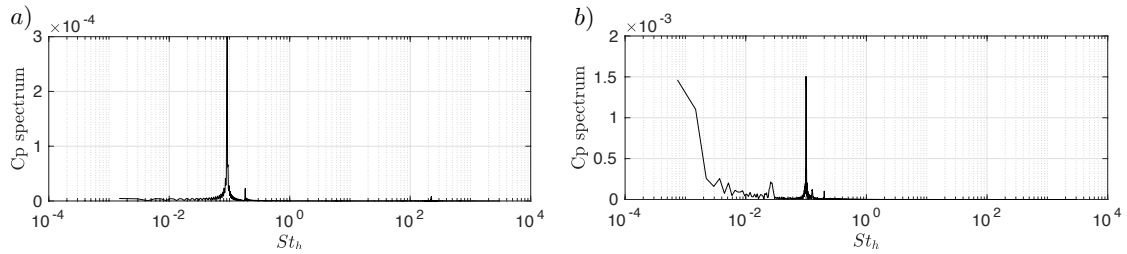


Figure 3.20: Base pressure spectra of the flow actuated at frequencies *a)* $St_f = 0.06$ and *b)* $St_f = 0.1$.

3.3.1 Effects of the Open-Loop Forcing

All simulations with open-loop forcing ran for at least 800 time units providing a sufficiently long signal to observe the effects of the forcing on the base pressure. Figure 3.19 summarises the effects of the open-loop forcing at amplitude $A_j = 0.1$ and frequencies $0.004 \leq St_f \leq 0.5$ on the mean base-pressure force ($\overline{Cp}$) and the rms value of the base pressure fluctuations around the mean. In most cases open-loop actuation increased the amount of fluctuations in the pressure signal. A small decrease in base pressure fluctuations about the mean is observed for forcing frequency $St_f = 0.08$ and is accompanied by a decrease in mean pressure. Forcing at frequencies $St_f = 0.04$ and $St_f = 0.06$ also affected the base pressure adversely - i.e. decreased it, however it also caused an increase in base pressure fluctuations. To visualise the different effects of the open-loop forcing on the flow fluctuations, two dimensional flow-field slices when the wake is actuated at $St_f = 0.06$ and $St_f = 0.08$ at amplitude $A_j = 0.1$ are shown in figures 3.21 and 3.22 respectively. Open-loop

St_f	0.04	0.06	0.08	0.1	0.15	0.2	0.3	0.4	0.5
St_H	0.09	0.09	0.09	0.1	0.15	0.2	0.3	0.4	0.5

Table 3.5: Dominant frequencies St_H of the base pressure signal spectrum from the simulations with open-loop forcing at amplitude $A_j = 0.1$ and forcing frequencies St_f ranging between $0.04 \leq St_f \leq 0.5$

forcing at frequency $St_f = 0.06$ causes the fluctuations about the mean to increase and considering figure 3.21 it is possible to see that the natural unsteady behaviour of the wake is amplified causing larger oscillations in the wake. When the flow is forced at $St_f = 0.08$ the wake is the least unsteady compared to it's behaviour when actuated at other frequencies, this is also confirmed in figure 3.22. It is worth noting that forcing at $St_f = 0.08$ caused the wake to flip across the horizontal plane of symmetry. For comparison the unforced flow is presented in figure 3.23.

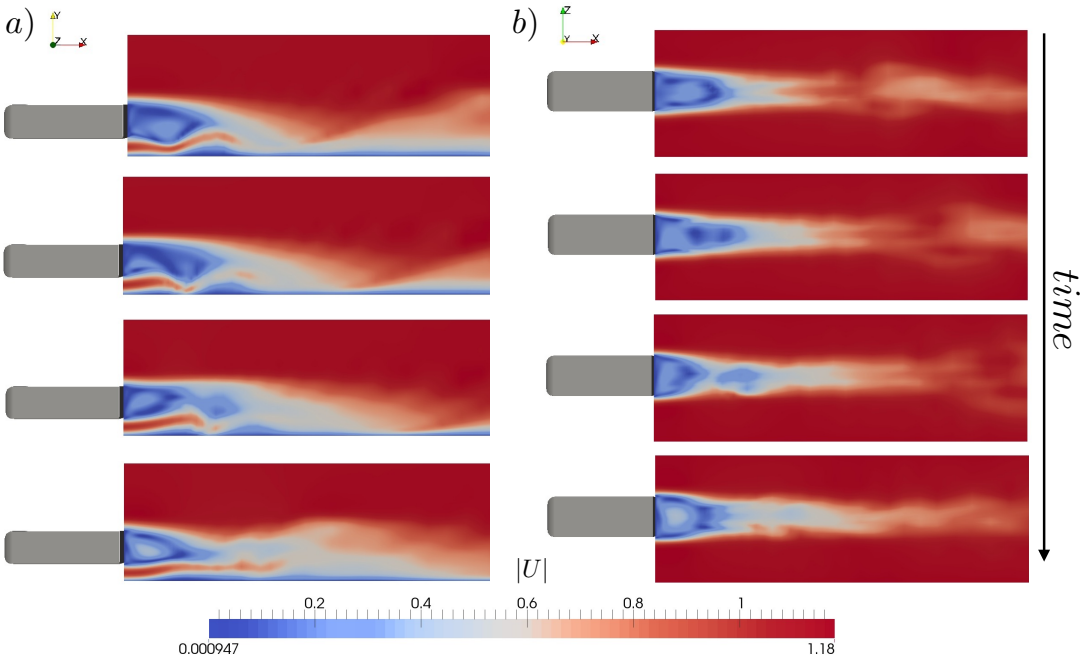


Figure 3.21: Instantaneous snapshots of the flow actuated at $St_f = 0.06$, $A_j = 0.1$: *a)* vertical slice, *b)* horizontal slice. Snapshots were taken at equal intervals over one cycle.

The spectra for the base pressure when the flow is actuated at $St_f = 0.06$ in figure 3.20 *a)* shows that the dominant frequency peak remains at $St_H \approx= 0.09$

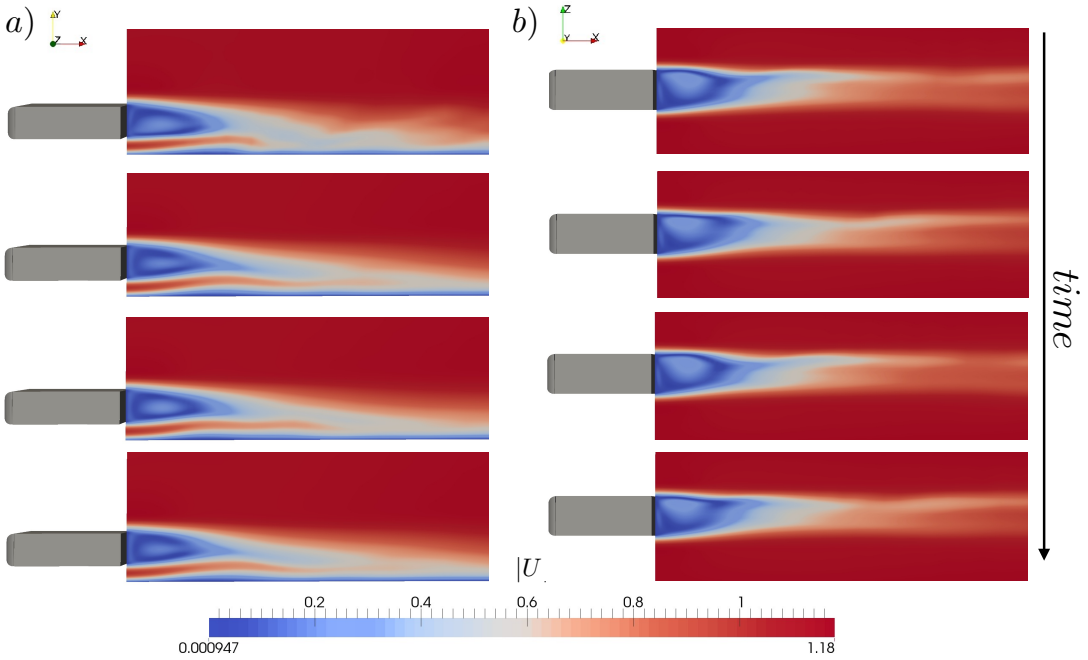


Figure 3.22: Instantaneous snapshots of the flow actuated at $St_f = 0.08$, $A_j = 0.1$: *a)* vertical slice, *b)* horizontal slice. Snapshots were taken at equal intervals over one cycle.

despite actuation at $St_H = 0.06$. The pressure spectrum reflects the actuation frequency only when actuating at or above $St_f = 0.1$. This behaviour is also observed in table 3.5 summarising the effects of forcing on the frequency spectrum of the base pressure. Frequencies lower than 0.1 have little effect on the dominant dynamic reflected in the spectrum of the base pressure, while forcing at frequencies above 0.1 completely dominates the wake. It appears the wake is less affected by low frequency actuation and maintains its natural frequencies. As described in the next section, the system identification procedure used in this work has the ability to extract the flow response from signals exhibiting dominant frequencies different to the forcing frequency.

3.3.2 System identification

The phase and gain shift in sensor signal is now measured for each forcing frequency and amplitude. First the sensor signal is analysed to remove all the transients.

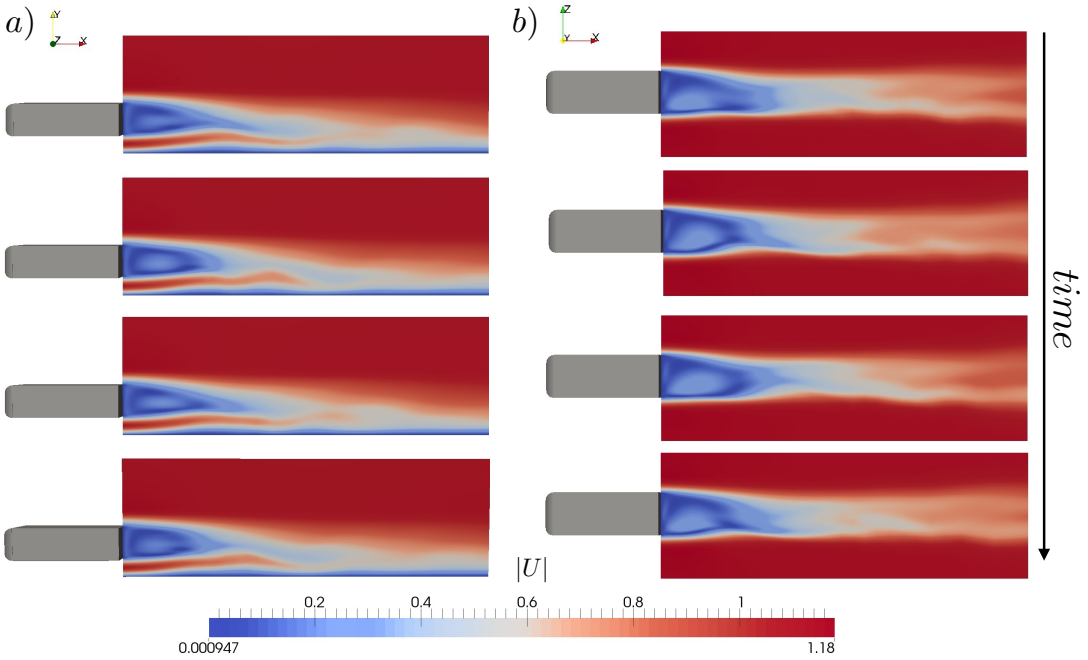


Figure 3.23: Instantaneous snapshots of the unforced flow. *a)* vertical slice, *b)* horizontal slice. Snapshots were taken at equal intervals over one cycle.

Then the signal is decomposed into sine and cosine Fourier transforms, isolating the forcing frequency and extracting the gain and phase shift using the procedure described in [118]. The resulting system identification data are summarised in figure 3.24. The different markers show variations in response when the flow is forced at different amplitudes A_j. It is possible to see that for the difference in gain and phase shift is small throughout the range of frequencies considered. Some weakly nonlinear effects are present around $St_f = 0.1$, but away from that frequency the dynamic linearity assumption holds. Then, based on the system identification data collected from open-loop forcing simulations, a low-order model for $G(s)$ can be fitted to the data using the Matlab command $fitfrd$.

3.4 Feedback Control

In this section a feedback controller is designed with the aim of attenuating fluctuations in the base pressure force. It is envisaged that in suppressing these fluctuations,

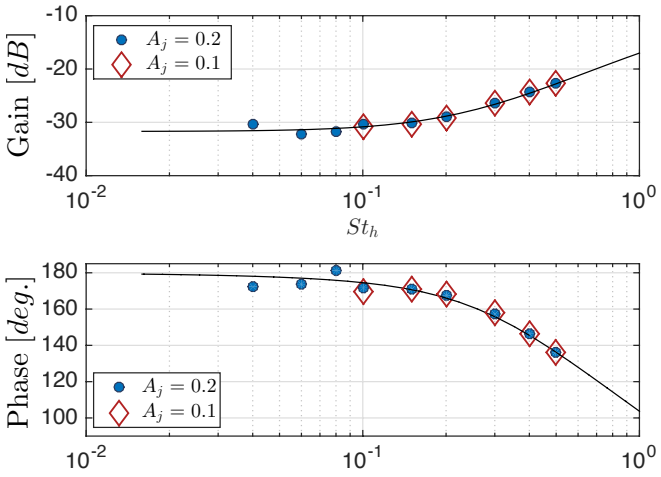


Figure 3.24: System identification data of frequency response gain and phase from open-loop simulations at $A_j = 0.1$ and $A_j = 0.2$.

a mean base pressure recovery will be achieved, giving a form-drag reduction. Having obtained the low-order linear model $G(s)$ in section 2.3, it is possible to proceed with designing the feedback controller $K(s)$.

The feedback controller, $K(s)$, was designed by shaping its response in the frequency domain ("loop shaping") to ensure low sensitivity for key frequencies and closed loop stability. The base pressure spectrum showed two peaks at $St_H \approx 0.09$ and $St_H \approx 0.18$, setting the targeted frequency range to $St_H \sim 0.09 - 0.18$. The final feedback controller is a combination of a second-order low-pass and first-order band-pass filters $K(s) = K_{lp}(s)K_{bp}(s)$ shown in eq. (3.1).

$$K_{lp}(s) = \frac{k\omega_{co}^2}{\omega_{co}^2 + 2\xi s\omega_{co} + s^2}\,, K_{bp}(s) = \frac{s\omega_h}{(\omega_l + s)(\omega_h + s)} \tag{3.1}$$

where the coefficients for the low-pass filter are: $k = -350$, $\xi = 6$ and $\omega_{co} = 0.13 \times 2\pi$ and the coefficients for the band-pass filter are: $\omega_h = 5 \times 2\pi$ and $\omega_l = 0.05 \times 2\pi$. The phase and gain of the controller $K(s)$ along with the resulting sensitivity transfer function are shown in figure 3.25 *b)*.

First the feedback controller was implemented in the simulations with the stationary ground at $Re_H = 435$; the unforced and forced base pressure signals

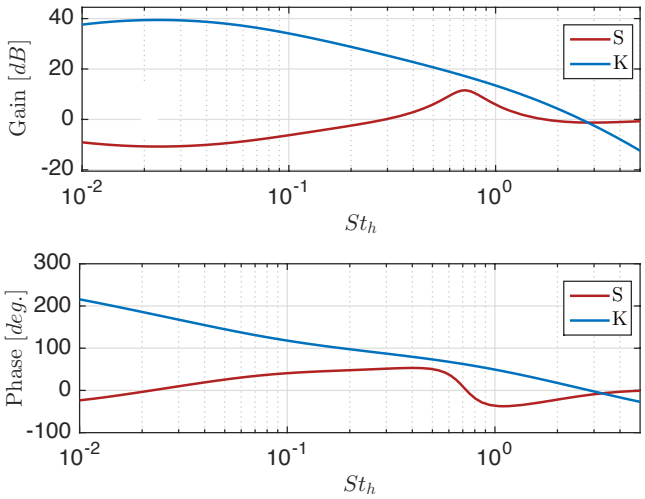


Figure 3.25: Frequency response gain and phase for the controller $K(s)$ and sensitivity function $S(s)$.

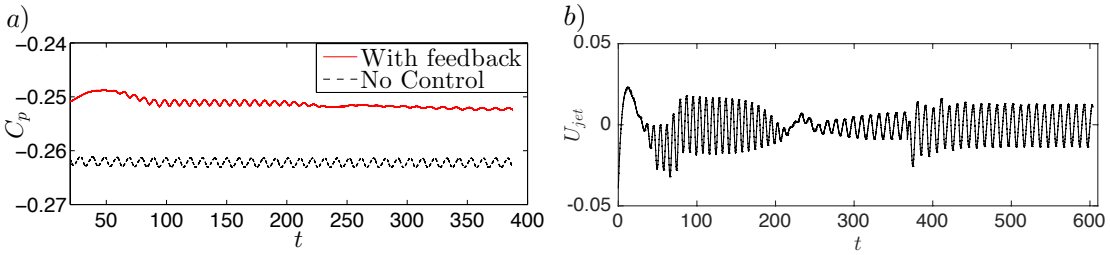


Figure 3.26: a) Comparison of converged base pressure coefficient, C_p, with (red) and without (black) feedback control. b) Corresponding actuation signal, U_{jet}

are compared in figure 3.26, alongside the actuation signal. Control successfully attenuated base pressure fluctuations, reducing the RMS by 33%. The base pressure spectrum of the flow with feedback control in figure 3.27 shows that low frequencies in the targeted range were successfully damped. Only a small peak remained at $St_H \approx 0.13$ compared to the unforced case. The reduction in base pressure fluctuations was accompanied by an increase in the mean base pressure of approximately 5%, which was achieved quickly, with convergence in approximately 20 convective times, and with actuation having zero mean throughout. Figure 3.28 shows two-dimensional horizontal velocity field slices (left) and vertical pressure field slices (right) of the wake both in the absence and presence of feedback control. The controlled wake has been re-symmetrised horizontally compared to the uncontrolled flow and the

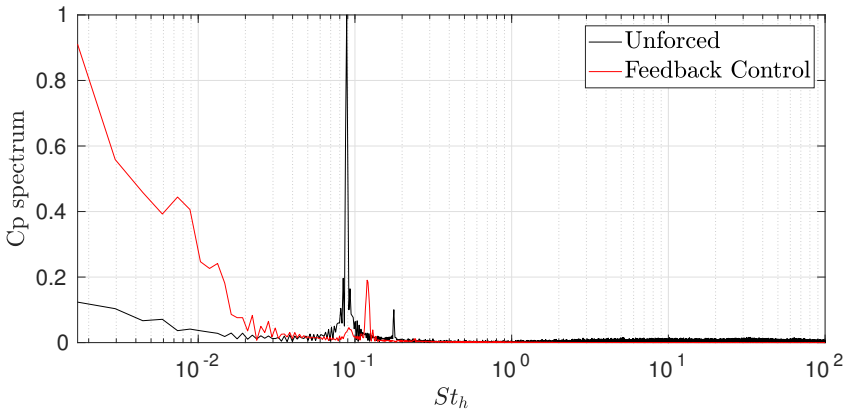


Figure 3.27: Base pressure signal spectrum for the Ahmed body flow at $Re_H = 435$ with and without feedback control.

low pressure region at the rear has been reduced and shifted further downstream away from the base. Figure 3.29 of the positive Q-criterion contours in the wake compares the unforced flow with the controlled flow. The comparison reveals that the wake is shifted upwards compared to the unforced flow where the ground effect was displacing the wake downwards (figure 3.8). Secondly the large counter-rotating structures further downstream in the wake have been weakened and don't appear in the flow with feedback control.

The drag coefficient for the controlled flow was $C_d = 0.2995$, approximately a 3% reduction on the unforced value. Note that as the controller aims to suppress base pressure force fluctuations, it is somewhat limited in what is achievable at the present low Reynolds number; the flow is not strongly unsteady and fluctuations are relatively small. Nonetheless, the implementation demonstrates that the linear feedback control strategy has potential for 3-D bluff body geometries at turbulent numbers.

The same feedback controller was applied to the simulations with moving ground. As can be seen from figure 3.30 the controller attenuated fluctuations, however there was no mean pressure recovery achieved. Overall the fluctuations of the base pressure signal about the mean decreased by 50% from 0.0084 (unforced) to 0.0042 (with feedback control). While the controller achieved its goal of suppressing

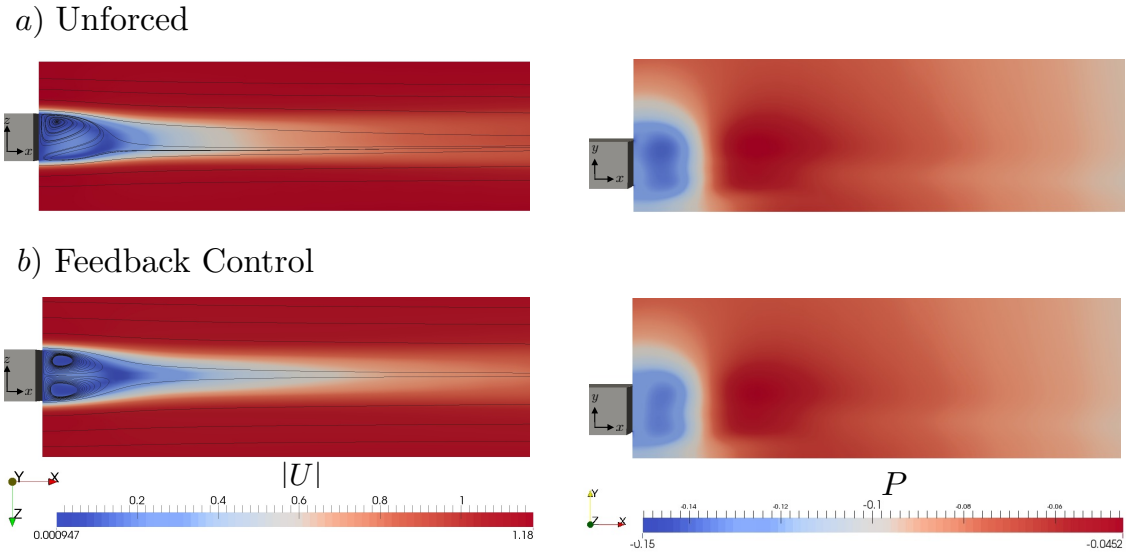


Figure 3.28: Horizontal 2D slice coloured by velocity magnitude with streamlines projected onto it (left) and vertical 2D slice coloured by pressure (right) of the *a)* unforced and *b)* controlled instantaneous flow fields

fluctuations, no mean drag increase was achieved. Even through the main wake frequencies remain the same for both configurations (figure 3.14) the ground effects are significantly weaker when the ground is moving, resulting in a more elongated recirculation region and consequently high base pressure. This would affect the phase and shift in the response of the flow to actuation and impede the ability of the low-order model $G(s)$ to approximate the relationship between actuation and sensing. This example highlights the importance of using moving ground in investigation of feasible control strategies for the Ahmed body flow.

3.4.1 Wake Mode Analysis

This section considers further the effects of the feedback controller on the Ahmed body flow over stationary ground. The apparent symmetrisation of the wake by the action of feedback control, even through the controller only targeted attenuation of fluctuations, leads us to analyse the wake modes using Dynamic Mode Decomposition (DMD) described in section 2.4.2. The results from DMD analysis for the Ahmed body flow without feedback control and in the presence of feedback control

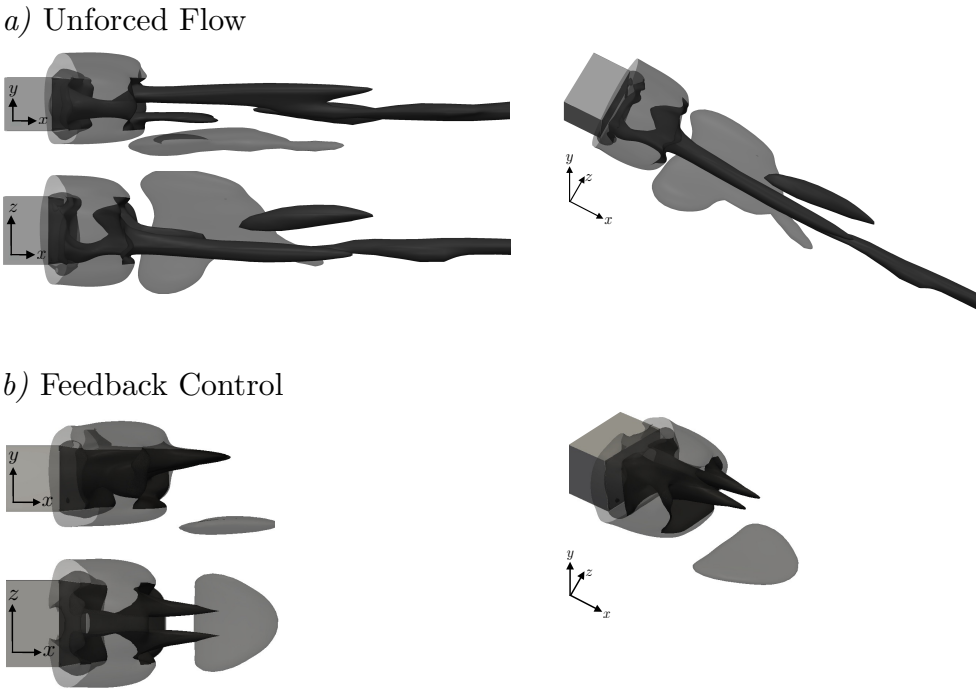


Figure 3.29: Q-criterion iso-contour of Ahmed Body flow at Reynolds number $Re_H = 435$ *a)* without and *b)* with feedback control. The top and bottom left pictures show top view and side view respectively; the right picture shows the diagonal view from the top. The same Q-criterion iso-contour is plotted with opaque and transparent parts to reveal the internal structure of the vortex ring in the wake.

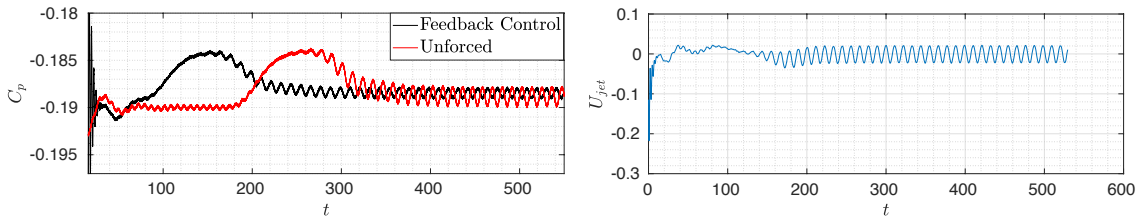


Figure 3.30: *a)* Comparison of the base pressure coefficient, C_p, with and without feedback control implemented to the case with moving ground. *b)* Corresponding actuation signal U_{jet}.

are shown in figure 3.31 *(a)* and *(b)* respectively. The top figures show the frequencies and growth rates of the DMD modes scaled by their optimum amplitudes. The most prominent unsteady mode in the unforced flow is at $St_H \approx 0.16$. The spatial structure of this mode is shown in the bottom picture of figure 3.31 *(a)*, revealing asymmetric shedding from only one side of the base. Once the feedback control is applied the growth rate vs. frequency plot shows that most of the low-

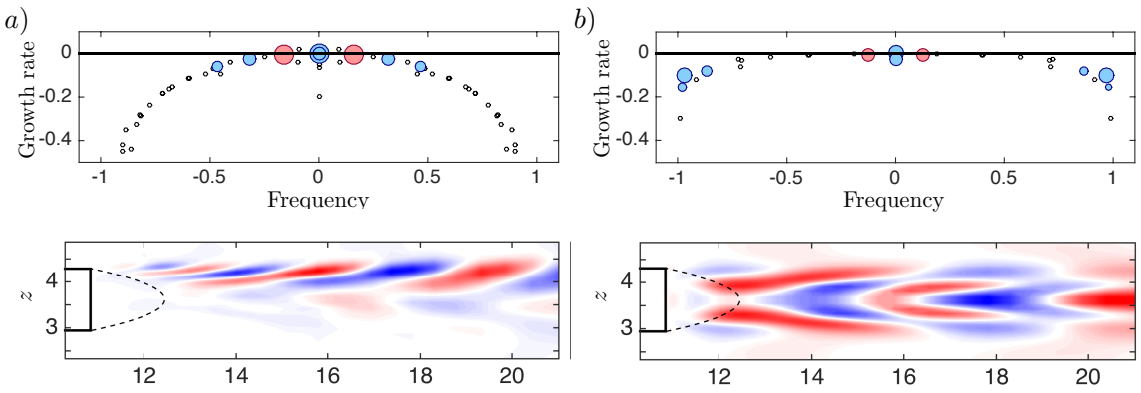


Figure 3.31: DMD results for *(a)* the unforced flow and *(b)* the flow with feedback control. The top figure shows the frequencies and growth rates of the DMD modes scaled by their optimum amplitudes; bottom figure is a top-view of the spatial structure of the most dynamically represented modes (red markers on the frequency vs. growth rate figure) at *(a)* $St_H = 0.16$ for unforced flow and *(b)* $St_H = 0.13$ for the flow with feedback control.

frequency dynamics seen in the unforced flow have been attenuated in accordance with the control aim. The most prominent low-frequency mode shifts to a frequency of $St_H = 0.13$, with its spatial structure revealing horizontally symmetric shedding consistent with the flow visualisations in figure 3.28. Notably the $St_H = 0.13$ is the only frequency peak visible in the base pressure spectrum of the flow with feedback control shown in figure 3.27. It is not uncommon for feedback control to shift the frequency of main dynamics, and in this case it appears to make the shedding slower and in-phase horizontally.

The importance of re-symmetrisation of the wake for drag reduction was highlighted by [30] who implemented passive boat tail control to weaken the reflectional symmetry breaking modes. Since overall perturbations in the flow are linked to the symmetry breaking behaviour of the wake it appears that attenuating the base pressure fluctuations reduced the overall perturbations in the wake, returning the wake to symmetry and achieving an increase in the mean base pressure.

3.5 Final Remarks

In this chapter the low Reynolds number bifurcation sequence for the Ahmed body wake, previously reported only in experiments, was reproduced numerically. The main flow features were investigated, revealing that as the reflectional symmetry of the wake is broken, the structure of the recirculation bubble changes from two recirculation regions positioned side by side, to one on top of the other. The vortex structure within the wake also moves from centred position to the side, affecting the position of the large recirculating vortices further downstream. It was conjectured that this change in the flow happens once there is sufficient underbody flow, allowing the shear layers shed from the top and bottom of the base (which are closer to one another than those from the side walls) to interact.

Linear feedback control, which targeted attenuation of the base pressure force fluctuations, was then applied. The control was implemented via body mounted sensors and unsteady synthetic jet actuation, for practical applicability. The effect of control was to attenuate the base pressure force fluctuations, increase the base pressure, reduce the drag and re-symmetrise the wake. DMD analysis of the controlled and uncontrolled flows at $Re_H = 435$ revealed that the feedback control slightly reduced the frequency of the shedding mode. The shedding from the sides also became in-phase when the control was applied. The topology of the wake was affected by feedback control as well: the recirculation region was elongated and the large counter-rotating vortices observed far downstream in the unforced flow were severely weakened.

In the next chapter we proceed to simulate Ahmed body flow at higher Reynolds numbers of $Re_H = 33,000$ and $Re_H = 25,000$, where reflectional symmetry breaking modes emerge as bi-modal or multi-modal switching at long timescales between asymmetric states. Open-loop forcing is also conducted to test the actuation/sensing arrangement with the view of moving towards feedback control for form-drag reduc-

tion.

Chapter 4

Turbulent Ahmed Body Flow

This chapter presents the results from simulations of the Ahmed body at $Re_H = 33,000$ and $Re_H = 25,000$. While in real life situations vehicles would experience Reynolds numbers of $Re \geq \mathcal{O}(10^6)$, achieving real-life Reynolds numbers in simulations is not always necessary for a simulation to yield useful information, as exemplified by Moin and Mahesh [89]. It is expected that especially for massively separated flows (such as blunt bluff bodies), in which the size of the eddies depends on the geometry rather than the Reynolds number, the qualitative features of the flow should not differ much once the critical Reynolds number range is passed. The Reynolds number chosen for this section ($Re_H = 33,000$) also matches the experimental study by Grandemage et. al. [45]. However, simulations of the flow at $Re_H = 33,000$ are expensive and to reduce the computing costs the open-loop forcing was performed on the Ahmed body flow at $Re_H = 25,000$ to evaluate the effects of the actuation shape and to start gathering system identification data towards designing the feedback controller overviewed chapter 2. At $Re_H = 25,000$ the flow is still turbulent at separation (as is the flow past the Ahmed body at $Re_H = 33,000$), making it a viable and more computationally efficient test-case for evaluating the chosen control shape and collecting system identification data. It is envisaged that any feedback controller design based on the collected data then could be tested on

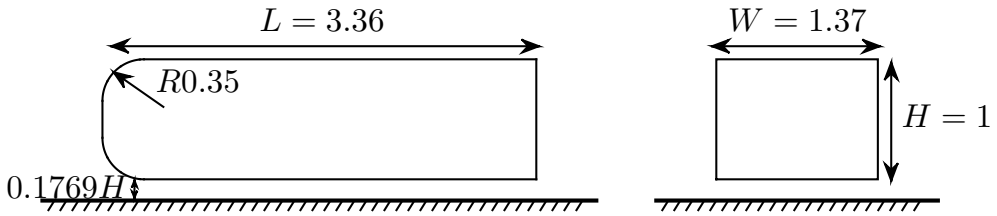


Figure 4.1: Schematic of square-back Ahmed body: (a) side view ; (b) rear view.

both flows: at $Re_H = 25,000$ and $Re_H = 33,000$.

4.1 The test-case

In the Large Eddy Simulations presented here the boundary layers along the Ahmed body walls and the ground are resolved, rather than using wall-models. While resolving the boundary layer increases the cost of simulations, we believe it is necessary to capture the bi-modal behaviour of the wake. Another important feature in all simulations presented here is that the turbulence and bi-modality are allowed to develop on their own, rather than 'tripping' the flow. It is a common practice in numerical simulations to force the switching in the wake by introducing a perturbation, however in present simulations bi-modality occurs on its own.

4.1.1 Computational Domain

To reduce the simulation costs, the computational domain used for high Reynolds number simulations was reduced to $\Omega_{AB} = (L_i, L_x, L_y, L_z) = (1.3L, 6.3L, 1.6L, 1.6L)$ where L_i is the inlet length and L_x, L_y and L_z are lengths in $x-$, $y-$ and $z-$directions. The domain still extends at least four body lengths behind the Ahmed body - sufficient to capture all scales of motion in the wake. The cross-section of the computational domain was reduced from $2L \times 2L$ to $1.6L \times 1.6L$ as in previous studies Krajnovic et. al. [62] found that $L_z = L_y = 1.6L$ was sufficient. Another change was

reduction in the length of the domain after the Ahmed body to four body lengths and reduction in the inlet from $2L$ to $1.3L$. The domain is still quite large compared to most computational studies of the Ahmed body flow; for example previous simulations obtained good results using domains with inlet of $1L$ [82] and length after body of $2L$ [47]. While the domain used for this case is smaller then the one presented for the low Reynolds number flow, these dimensions still fall within the accepted proportions proposed by ERCOFTAC [56, 77]. To check if the shorter

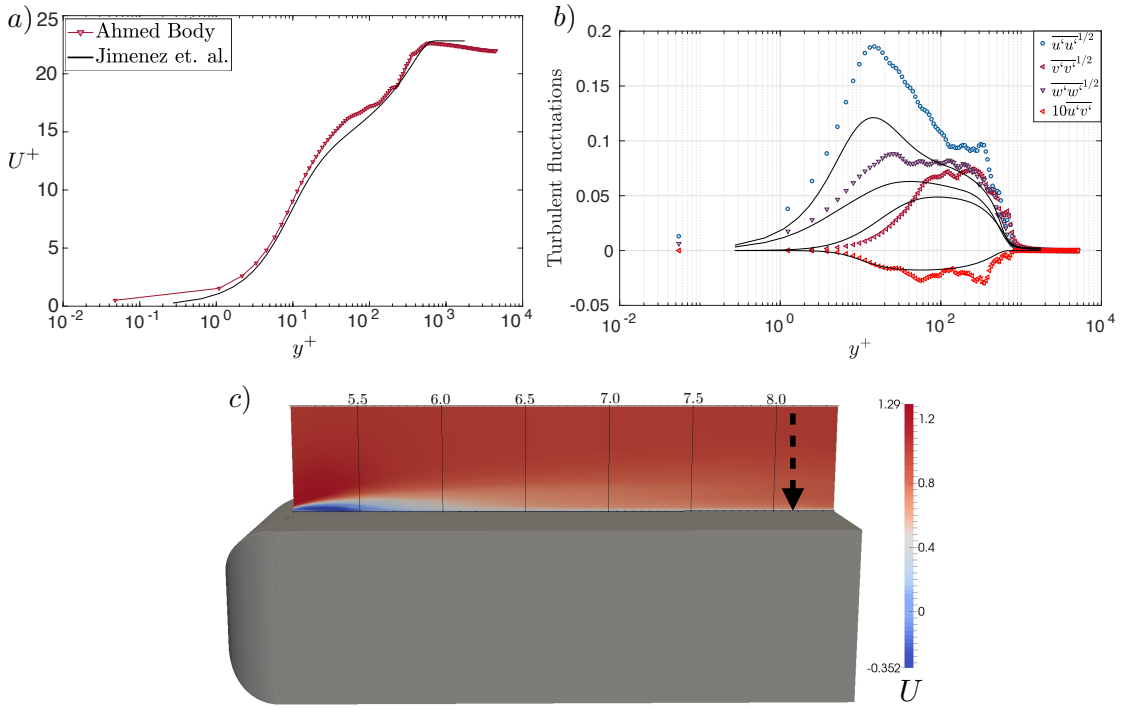


Figure 4.2: Flow characteristics sampled before separation (arrow) along the horizontal centerline of the north boundary of the Ahmed body. LES data is compared to DNS channel flow data (at $Re_\theta = 1551$) from Jimenez et al. [57] (solid lines). *a)* the mean streamwise velocity profile, *b)* the root-mean-square turbulent fluctuations and Reynolds stress and *c)* sampling location.

domain inlet has adverse effects on the development of the turbulent boundary layer at separation, the root mean square turbulent fluctuations, Reynolds stress and streamwise velocity profiles from simulations at $Re_H = 25,000$ are compared to turbulent channel flow data from [57] in figure 4.2. It is possible to see that there is fair agreement for the velocity profile. The turbulent fluctuations and stresses for the Ahmed body flow and channel flow are similar for the first few cells, but

further away from the body three dimensional fluctuations, characteristic of Ahmed body flows, cause discrepancies between the channel data and the Ahmed body simulations data. This most likely happens due to the flow separating near the nose creating a small recirculation bubble. The bubble generated a disturbance in the boundary layer which is the convected downstream along the body sides, affecting the boundary layer at separation and introducing more three-dimensional turbulent fluctuations. The level of fluctuations (even larger than for the turbulent channel flow) suggests that the separation is turbulent. To further investigate the characteristics of the boundary layer the Reynolds number based on the momentum thickness and the shape factor along the north boundary of the Ahmed body are computed and presented in figure 4.3. At separation the Reynolds number based on momentum thickness is around $Re_\theta = U_\infty \theta/\nu \approx 3000$ and the shape factor is around $H = \delta^*/\theta \approx 1.2$ where $\delta^* = \int_0^\infty (1 - u/u_\infty)dy$ is the displacement thickness and $\theta = \int_0^\infty (u/u_\infty(1 - u/u_\infty)dy$ is the momentum thickness. For comparison, plate boundary layer is considered turbulent when the shape factor is $H < 1.3 - 1.4$ or when the $Re_\theta > 2000$ [103].

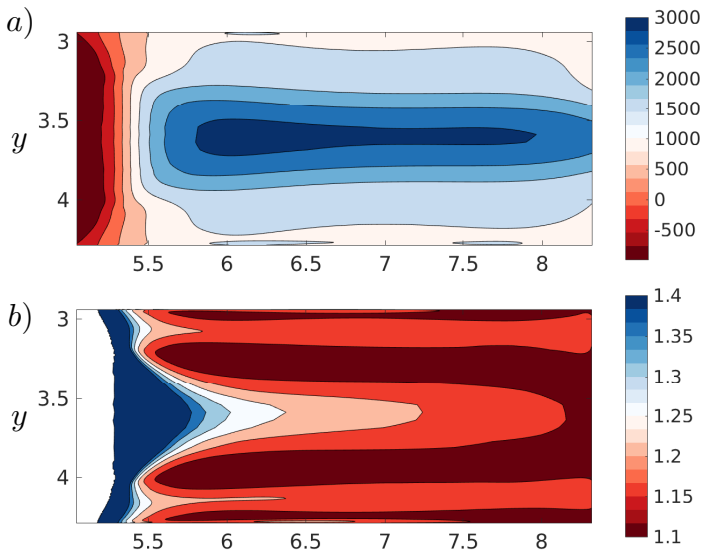


Figure 4.3: *a)* Re_θ and *b)* shape factor $H = \delta^*/\theta$ along the top surface of the Ahmed body at $Re_H = 25,000$.

4.1.2 Computational Mesh

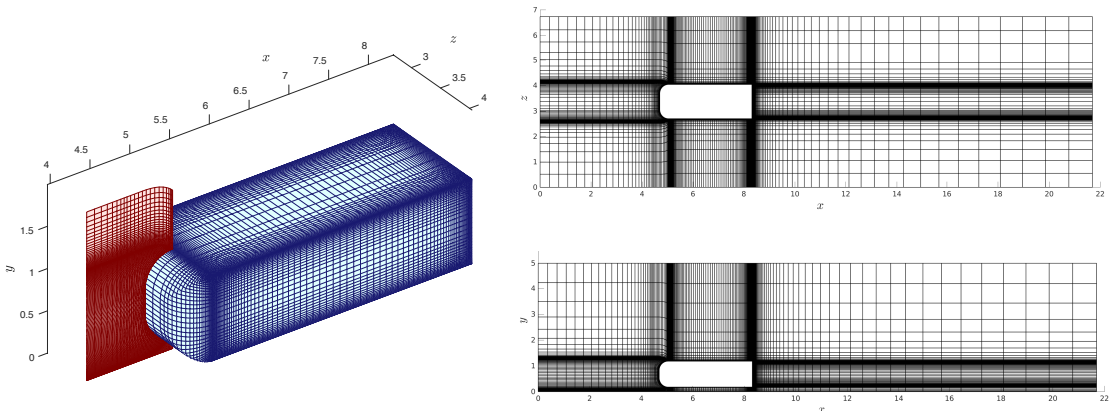


Figure 4.4: Structured grid used in the simulations of the Ahmed Body flow at Reynolds number $Re_H = 30,000$. Left: Grid in the vicinity of the body nose and discretisation around the body. Right: horizontal and vertical slices showing every 4^{th} node of the grid.

Grid	Nodes	Nodes adjacent to body boundary	C_d	Recirculation Length
Fine	$\approx$ 31.5 million	114,688	0.273	1.41
Nominal	$\approx$ 56.5 million	270,336	0.318	1.48
Fine	$\approx$ 86.5 million	524,288	0.318	1.50

Table 4.1: Grid comparison for simulations at $Re_H = 33,000$.

The Ahmed body used in this chapter corresponds to the standard Ahmed body case introduced in [2] and thus has a smaller ground clearance than in chapter 3. The exact proportions of the body can be seen in figure 4.1. In this case the ground clearance is $C* = \frac{C}{W} = 0.176$ and the aspect ratio is $H* = \frac{H}{W} = 0.73$. At turbulent Reynolds number Cadot et. al. [16] found that the ground looses its stabilising influence if it is above 7% of the body height. Taking this finding and the model presented in [45] (figure 4.5) into account, we expect to observe horizontal displacement of the wake in this case as well.

The domains were discretised differently for simulations at $Re_H = 33,000$ and

Grid	Nodes	Nodes adjacent to body boundary	C_d	Recirculation Length
Coarse	$\approx$ 31.5 million	114,688	0.224	1.35
Nominal	$\approx$ 82.5 million	294,912	0.340	1.49
Fine	$\approx$ 97.0 million	311,296	0.339	1.49

Table 4.2: Grid comparison for simulations at $Re_H = 25,000$.

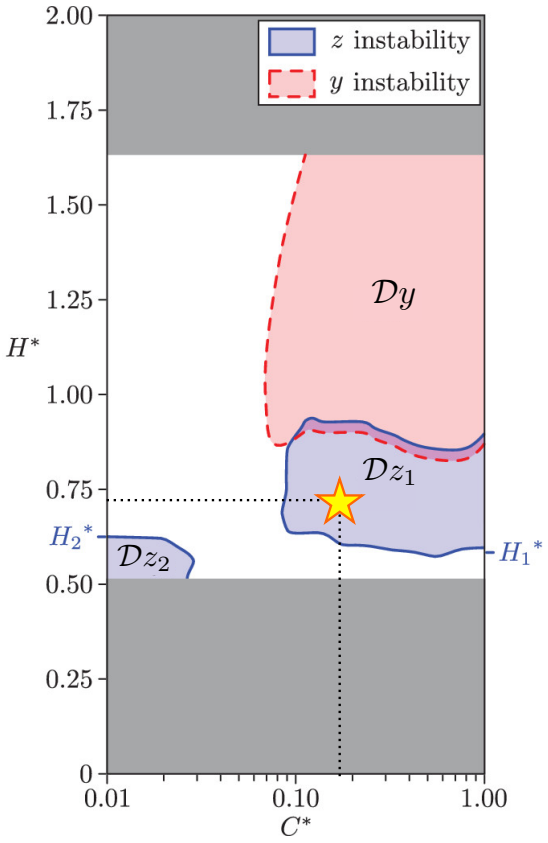


Figure 4.5: Regions of bi-modality as a function of ground clearance and aspect ratio. The yellow star indicates the behaviour expected to be observed for the current test-case.

$Re_H = 25,000$ due to changes in the architecture of the university HPC massively parallel cluster CX2. Simulations at $Re_H = 33,000$ were performed first and tested for convergence on two domains presented in the table 4.1. Since the domain is modular it is hard to achieve uniform increase in the number of cells in all directions without disproportionally increasing the computational costs. To conduct the convergence tests the overall number of cells was increased focusing on refining im-

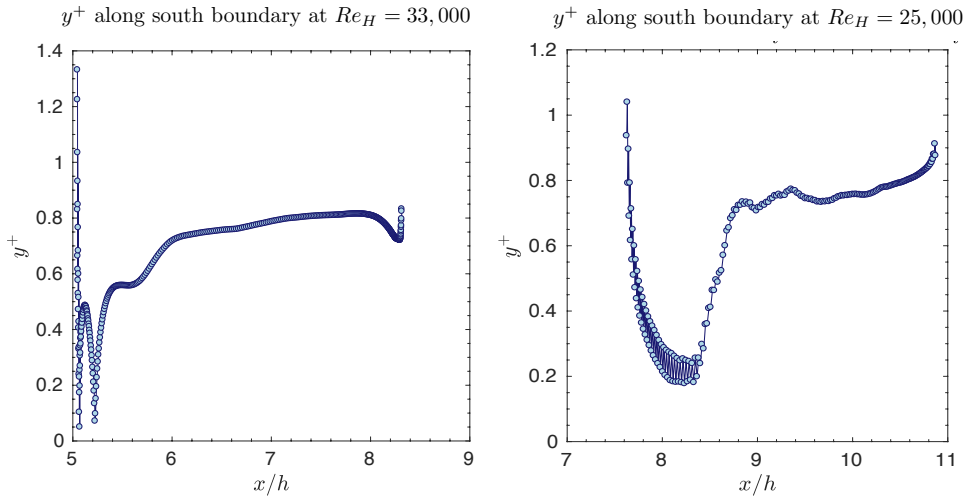


Figure 4.6: y^+ along the centerline of the south boundary of the Ahmed body at *a)* $Re_H = 33,000$ and *(b)* $Re_H = 25,000$.

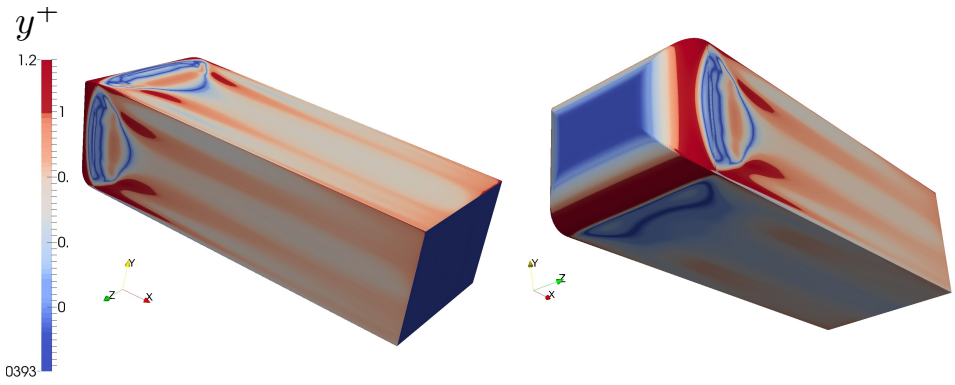


Figure 4.7: y^+ contours at $Re_H = 33,000$.

mediately around the body. Using more computational cells around the body meant that the domain was refined more heavily in all directions normal to the body, while the extremities of the domain (the corners) were refined to a lesser degree. The two quantities used for comparison are the drag coefficient and the length of the recirculation bubble measured at the free stagnation point. Only three grids were tested per Reynolds number due to computational costs.

The convergence checks for simulations at $Re_H = 33,000$ are summarised in table 4.1. While the coarse grid under-predicted both drag and the recirculation length, the differences in values between the nominal and fine grids, suggest that the nominal grid is suitable to accurately simulate the Ahmed body flow. The

nominal grid consists of 56 million computational points, has a maximum expansion ratio between consecutive cells of 1.05 in vertical and horizontal directions and skew maintained below 0.61. The discretisation of the domain is shown in figure 4.4. After completing the simulations at $Re_H = 33,000$ the architecture of the college cluster expanded, making it more time efficient to run on larger grids. The summary of the grids used for convergence checks at $Re_H = 25,000$ is presented in table 4.2. The coarse grid significantly under-predicted both control variables: the drag and the recirculation length. Such discrepancy is most likely due to short time of the coarse grid simulation. The nominal grid, consisting of significantly more computational nodes, seems to predict the control quantities well compared to the find grid. As a result the grid of approximately 82.5 million points was used for the simulations at $Re_H = 25,000$. The skew of the grid is kept below 0.63 and the maximum expansion ratio of two consecutive cells in the vertical and horizontal directions is 1.04.

The variation of y^+ along the Ahmed body surface is shown in figure 4.6, where it can be seen that y^+ remains below 1.5 for the simulations at $Re = 33,000$ and below 1 for simulations at $Re = 25,000$. Most importantly in all cases y^+ was below 1 at the separation edge. Figure 4.7 presents colour contours illustrating the full spatial variation of the y^+ around the body.

4.2 Unforced Flow

This section presents the results from unforced simulations of the Ahmed body flow at $Re_H = 33,000$. The unforced flow at $Re_H = 25,000$ was also simulated to use as reference in assessing the effect of the open-loop forcing discussed in section 4.3. However since the flows at $Re_H = 33,000$ and $Re_H = 25,000$ are qualitatively very similar, only results for $Re_H = 33,000$ simulation will be presented here.

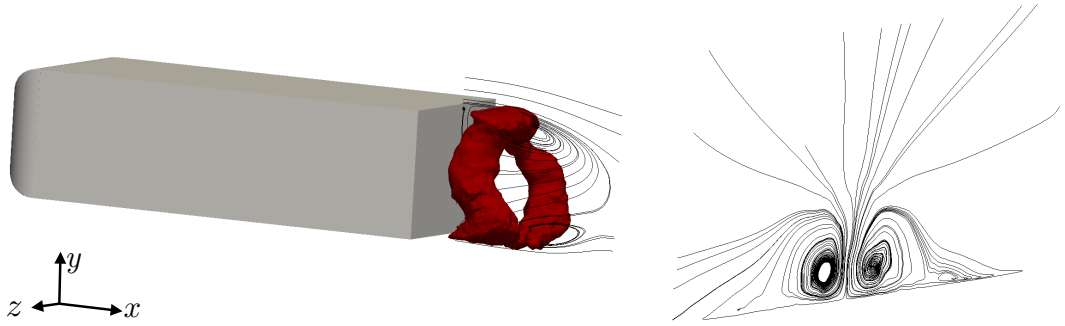


Figure 4.8: Time-averaged vortex-ring of a turbulent wake at $C_p = -0.22$ with streamlines projected onto two dimensional slices to reveal recirculation region in the near wake and large counter-rotating vortices in the far wake.

4.2.1 Time-Averaged flow

Simulation results compare well with the averaged flow previously reported in the literature and overviewed in section 1.2.1. Figure 4.8 shows the topology of the averaged wake. The near wake is defined by a low pressure vortex ring with a stronger upper vortex compared to the lower vortex, and further downstream the flow is dominated by two large counter-rotating vortices, similar to those reported in [101, 62, 45, 63] and visualised in figure 1.3. Figure 4.9 shows horizontal and vertical slices through the averaged flow and further confirms that the averaged wake is slightly asymmetric in the vertical plane due to the presence of the ground. Given a long enough time-average, the wake is completely symmetric in the horizontal plane. The drag coefficient of the unforced flow is $C_d = 0.32$ and the lift coefficient is $C_l = -0.03$. For these simulations the drag value also falls within the range reported in the literature of $0.26 - 0.36$ [43, 2, 112, 63, 93], while the recorded downforce is slightly smaller than the one reported by Grandemange et. al. [43].

4.2.2 Instantaneous flow

The unsteady wake is highly complex, exhibiting bi-modality and various coherent structures interacting with each other. This makes it difficult to describe the in-

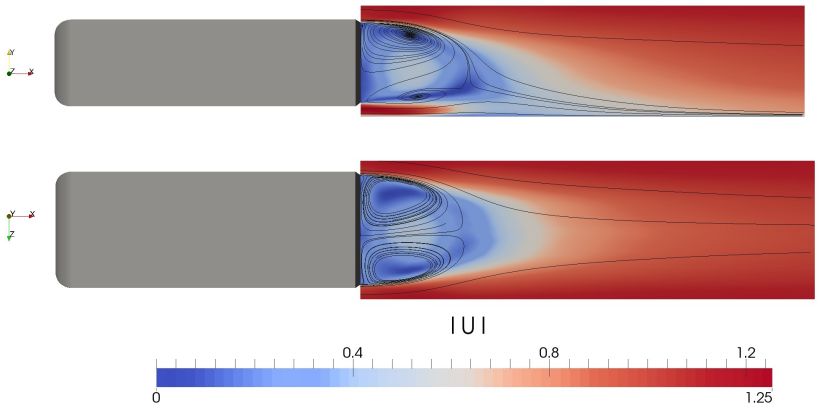


Figure 4.9: Time-averaged horizontal (top) and vertical (bottom) 2D slices of the wake coloured by velocity magnitude with streamlines projected onto them.

stantaneous behaviour of flow. At present most investigations of the Ahmed body flow dynamics are experimental and conducted in a wind tunnel. These experimental wake investigations use pressure taps, flow field velocity sensors and two-dimensional PIV planes, which makes it difficult to reconstruct the full three-dimensional flow field. This section, therefore, will attempt to describe the make up of the instantaneous wake topology based on the results from the Large Eddy Simulations.

The simulations successfully capture the bi-modality of the wake as can be seen in bottom graph in figure 4.10: at around 150 units the wake begins to switch its location. The pressure gradient in vertical direction shows that the wake is positioned towards the bottom of the base throughout the simulation due to the ground effect.

The behaviour of the flow when the wake is asymmetric is of particular interest. A number of theories regarding the topology of the wake when it is switching have been proposed. First, Evrard et. al. [30] conjectured that instantaneously the wake is made up of a horseshoe vortex system pictured in figure 4.11 *a)*, where the wake explores randomly the two reflectional symmetry breaking positions. Later Perry et. al. [93] proposed an alternative model where each reflectional symmetry breaking state is characterised by the coexistence of two vortical structures: a vortex shed

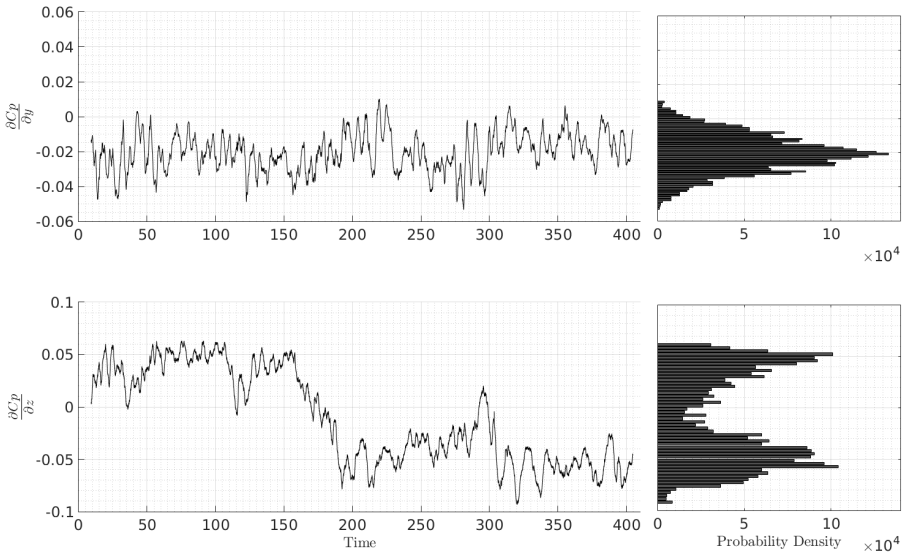


Figure 4.10: Base pressure gradient signal in vertical (top) and horizontal (bottom) directions

from one of the vertical edges of the base and a horseshoe vortex as pictured in figure 4.11 *b)*. These two structures average to a toroidal system. The authors

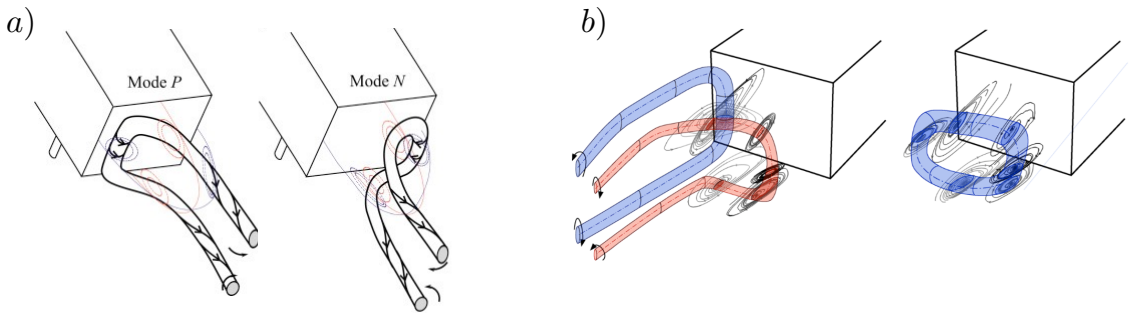


Figure 4.11: Instantaneous three-dimensional wake topology as proposed by *a)* Evrard et. al. [30] and *b)* Perry et. al. [93].

drew these conclusions from two-dimensional PIV slices. Our access to full three-dimensional flow field data enables visualisation of the unsteady pressure contours. We do not observe such a horseshoe vortex system in the wake described in [30] and [93]. The instantaneous pressure contours in figure 4.12 reveal that the vortex structure observed in the averaged flow can also be seen in the instantaneous flow,

but tilted according to the wake's position. This is much more similar to structures captured in the simulations by Lucas et. al. [74], who used conditional averaging to visualise tilted torus in the wake. Figure 4.12 confirms existence of the the toroidal structure in the instantaneous flow by showing pressure contours in three different instantaneous snapshots (columns) of the wake for three states (rows): when the wake is switched to the left, when it is in the center switching between the two reflection symmetry breaking states and when the wake is switched to the right. The vortex ring clearly deforms according to the position of the wake, while the vortex roll-ups which are shed from the edges interact with the vortex ring sides furthest away from the base. The interaction of the roll-ups and the vortex ring seems to sporadically manifest as horseshoe structures shed from the longest part of the wake (figure 4.13).

4.2.3 Modal Analysis

In this section modal analysis tools are used to consider the spatial distribution and interaction of the coherent structures in the wake.

4.2.4 Dynamic Mode Decomposition of the Turbulent Ahmed Body Wake

The results from the dynamic mode decomposition (DMD) of the pressure field of the Ahmed body wake are discussed here. As shown in section 4.2, most wake dynamics are best visualised using the pressure field - for this reason pressure field was chosen as the input for the DMD algorithm. To see how bi-modal behaviour affects the topology of the wake two sets of snapshots are considered: those from a time series during which the wake is positioned on the right and those from a time series during which the wake is positioned on the left. The snapshots extend from the body base to $1.5H$ in the downstream direction, sufficient to capture the full

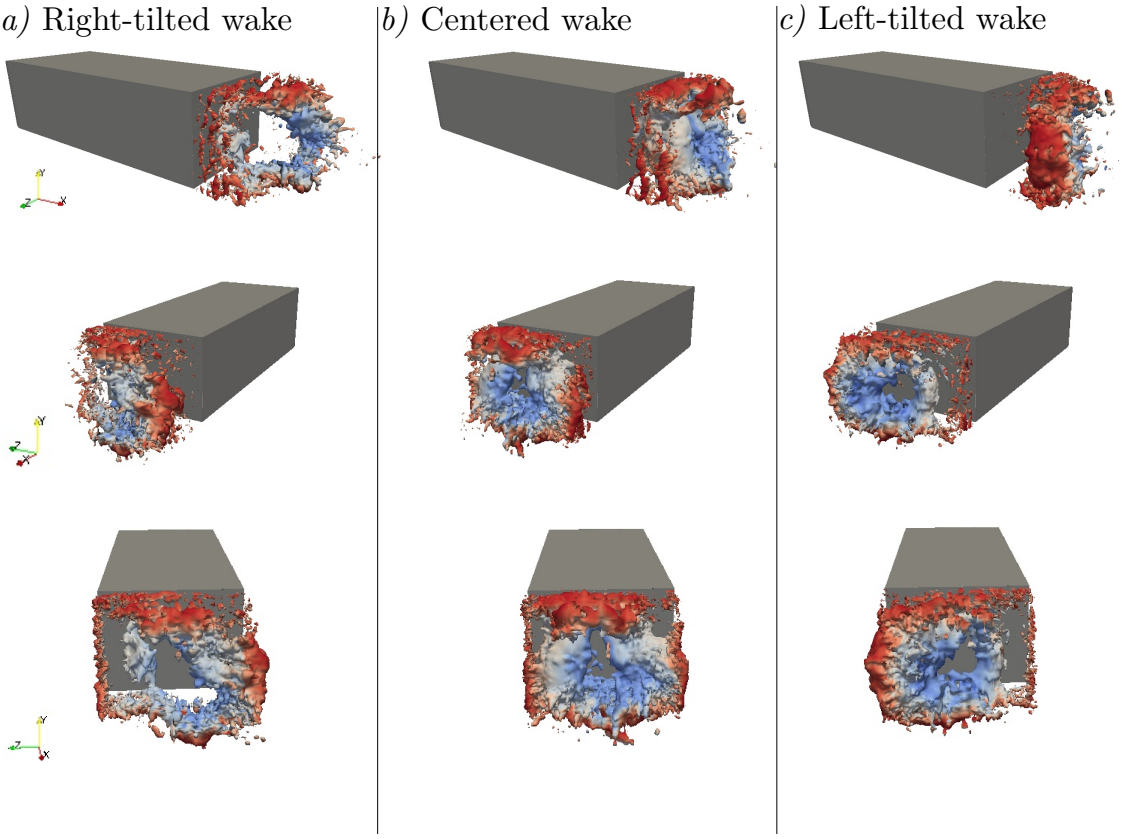


Figure 4.12: Evolution of the position of the instantaneous vortex ring when the wake is tilted *a)* and *c)* and the wake during the flip between the two positions *b)*. The vortex visualised using pressure contours at $Cp = -0.21$ coloured by velocity in the streamwise direction

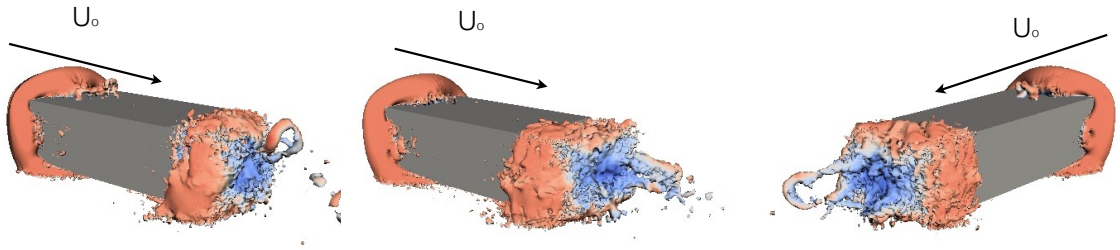


Figure 4.13: Horseshoe structures shed from the longest part of the wake visualised as pressure contours at $Cp = -0.16$ coloured by velocity in the streamwise direction.

recirculation region. The DMD algorithm was then applied as described in section 2.4.2.

The results of the dynamic mode decomposition are shown in figure 4.14, where the DMD modes are plotted on the growth rate vs frequency plane and the

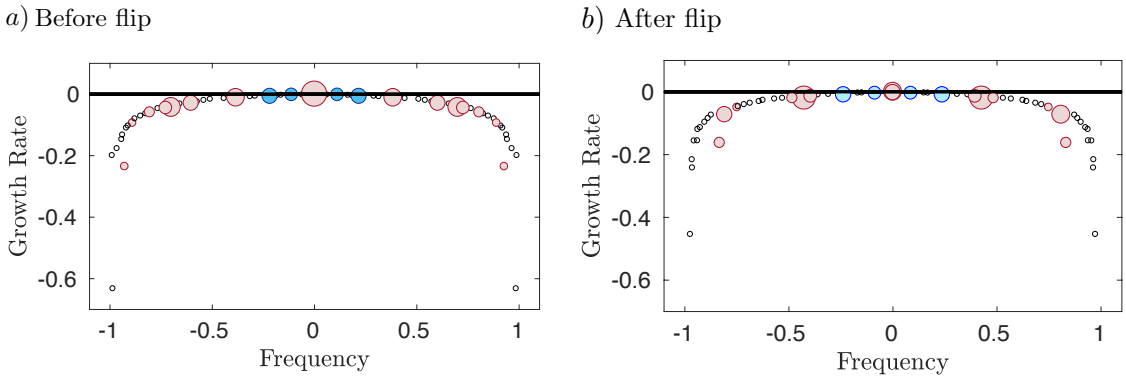


Figure 4.14: DMD modes plotted by their growth rates and frequencies and scaled by the amplitudes. The modes at $St_H \approx 0.08$ and $St_H \approx 0.2$ are highlighted in blue. *a)* DMD modes before the flip and *b)* DMD modes after the flip.

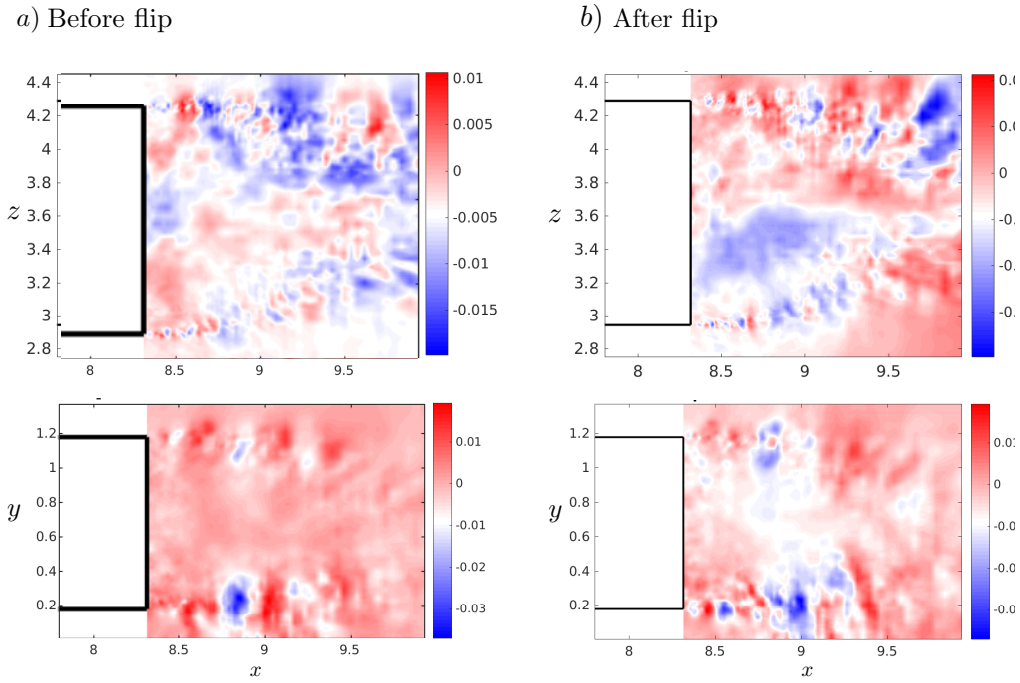


Figure 4.15: 2D slices (top - horizontal slice, bottom - vertical slice) of the DMD mode at $St \approx 0.08$ corresponding to bubble pumping mode *a)* when the wake is shifted to the left and *b)* after the flip when the wake is shifted to the right.

size of each mode is scaled with its amplitude. Unsurprisingly the mean is the most prominent mode with the highest amplitude. The other two modal pairs highlighted in blue are modes at $St \approx 0.08$ and $St \approx 0.21$. These DMD modes correspond to the peaks found using amplitude spectrum analysis and therefore will be considered

in further detail. Their high amplitude also reflects their prominence in the data. The mode at $St \approx 0.08$, generally accepted as the bubble pumping mode, is shown in figure 4.15.

The two-dimensional horizontal slices through the DMD mode at $St \approx 0.08$ reveal a horizontal asymmetric structure which shifts its position as the wake changes between asymmetric states. To better visualise the structure of the mode, three-dimensional contours are also plotted in figure 4.16. The contours reveal a toroidal structure, distorted in the direction of the flip due to bi-modality, now associated with frequency of $St \approx 0.08$. The shedding mode at $St \approx 0.21$ is visualised in figures 4.17 and 4.18. The two-dimensional slices through the mode in figure 4.17 reveal shedding structures originating at the body edges and spanning all along the recirculation region in the wake. Considering the three-dimensional contour visualised in figure 4.18 it is possible to see the structure of the recirculation region formed by these shear layers. One side of the structure is significantly weaker, corresponding to the shifted wake. Overall, using the DMD analysis presented in this section it has been possible to visualise the three-dimensional spatial structure of flow dynamics at bubble pumping and shedding frequencies.

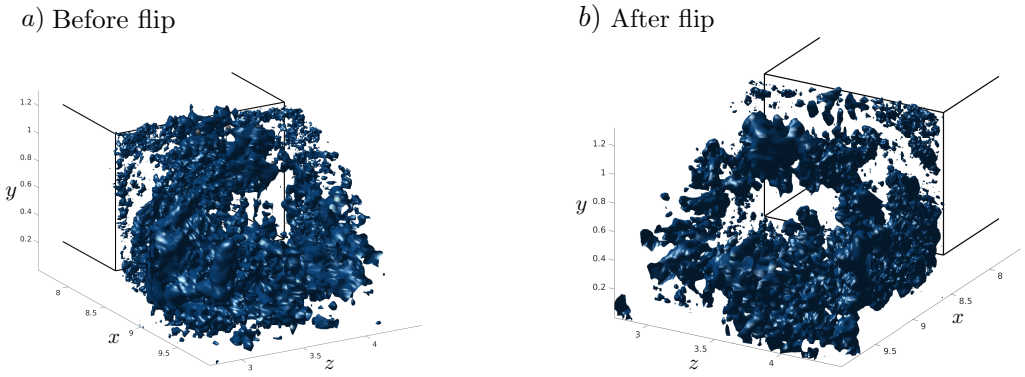


Figure 4.16: 3D iso-contours of the DMD mode at $St \approx 0.08$ corresponding to bubble pumping mode*a)* when the wake is shifted to the left and *b)* after the flip when the wake is shifted to the right.

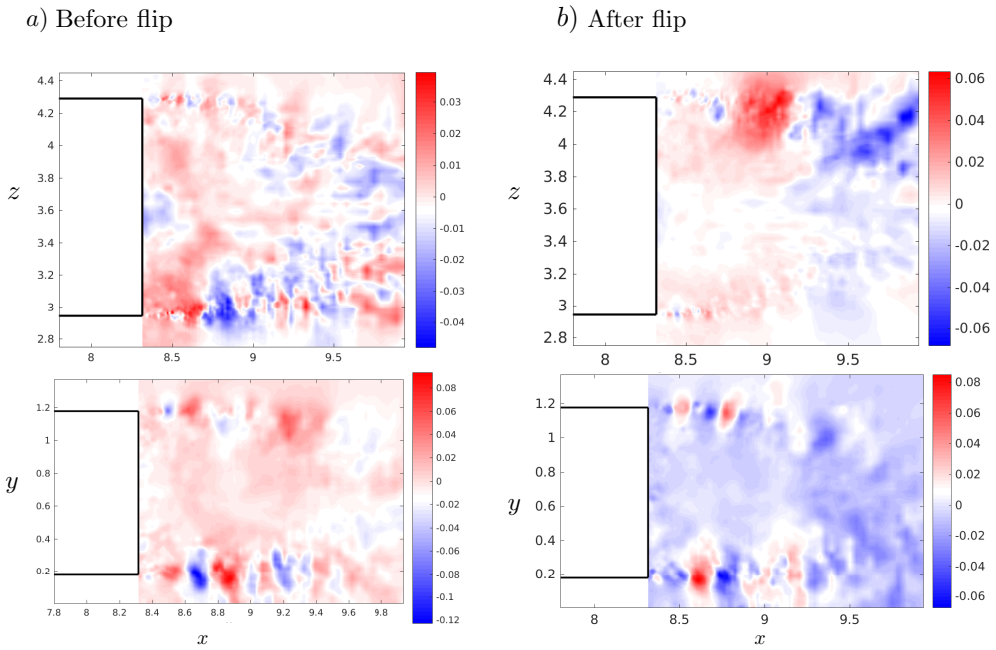


Figure 4.17: 2D slices (top - horizontal slice, bottom - vertical slice) through the DMD mode at $St \approx 0.2$ corresponding to shedding mode *a)* when the wake is shifted to the left and *b)* after the flip when the wake is shifted.

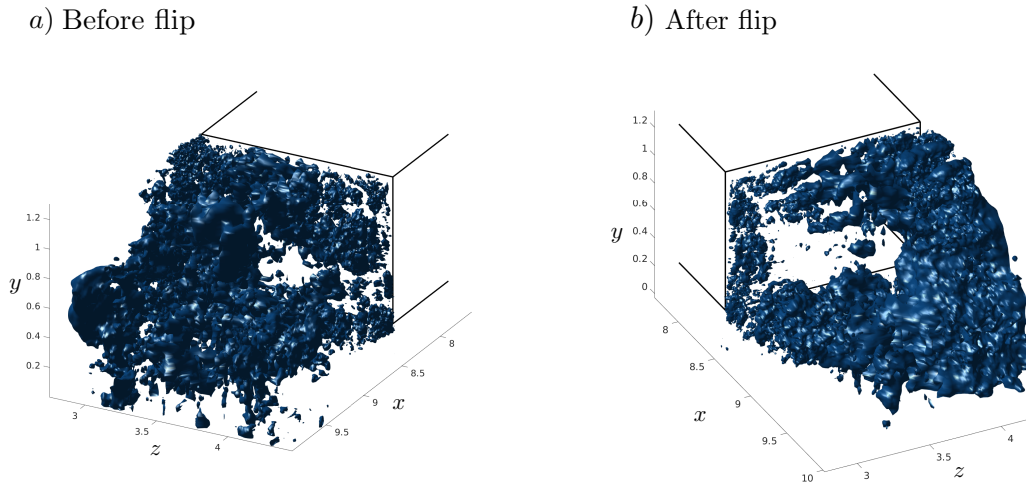


Figure 4.18: 3D iso-contours of the DMD mode at $St \approx 0.2$ corresponding to shedding mode *a)* when the wake is shifted to the left and *b)* after the flip when the wake is shifted.

4.2.5 Proper Orthogonal Decomposition of the Turbulent Ahmed Body Wake

To identify the most energetic structures in the wake of the Ahmed body, Proper Orthogonal Decomposition (POD) was used. Once again two sets of pressure field

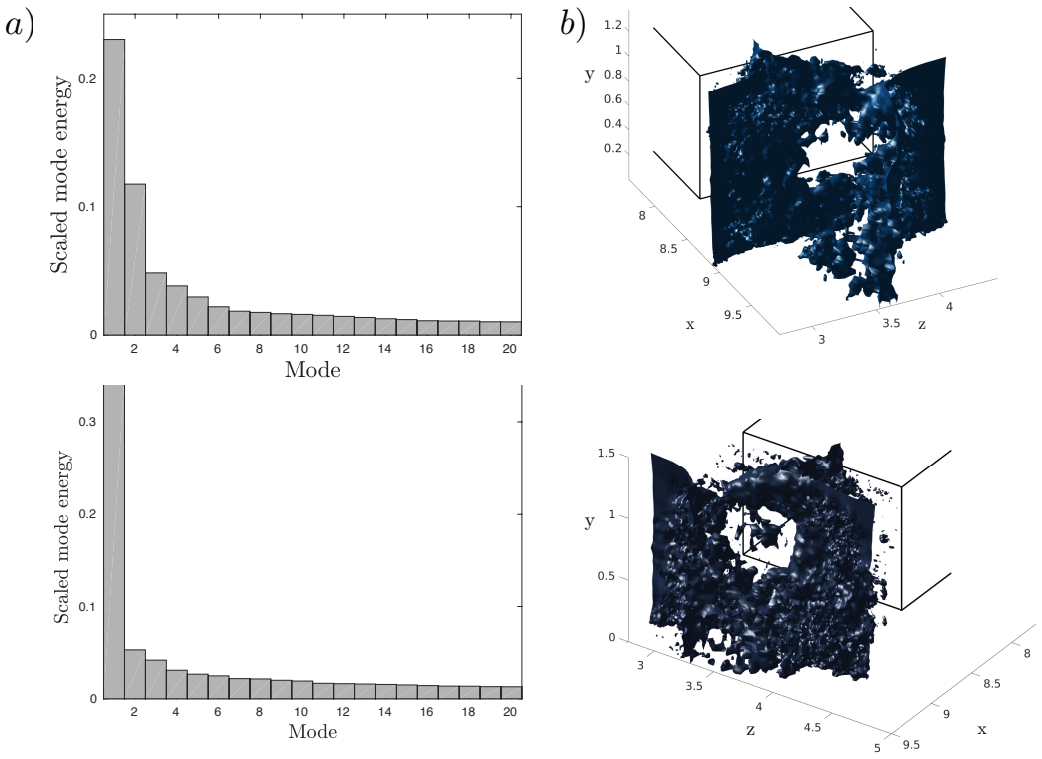


Figure 4.19: *a)* The energy of the extracted POD modes for two datasets: top - wake on the left, bottom - wake on the right. *b)* 3D iso contour (above 0) of the first and most energetic mode for the two datasets: top - wake on the left, bottom - wake on the right.

snapshots were used to study how the most energetic structures change with the position of the wake. The results are summarised in figure 4.19 *a)* showing the energetic content of the POD modes. The first mode is by far the most energetic and is visualised as a three-dimensional contour in 4.19 *b)*. The first and most energetic mode has the structure of a ring which is shifted according to the position of the wake. The next three modes are visualised in figure 4.20 revealing that the other modes are similar in structure regardless of the position of the wake. The other modes are symmetric and are being convected downstream and downwards.

The next few modes, shown in figure 4.20, are no longer tilted according to the wake. The structure of the 2*nd* POD mode is more energetic on one side, reflecting

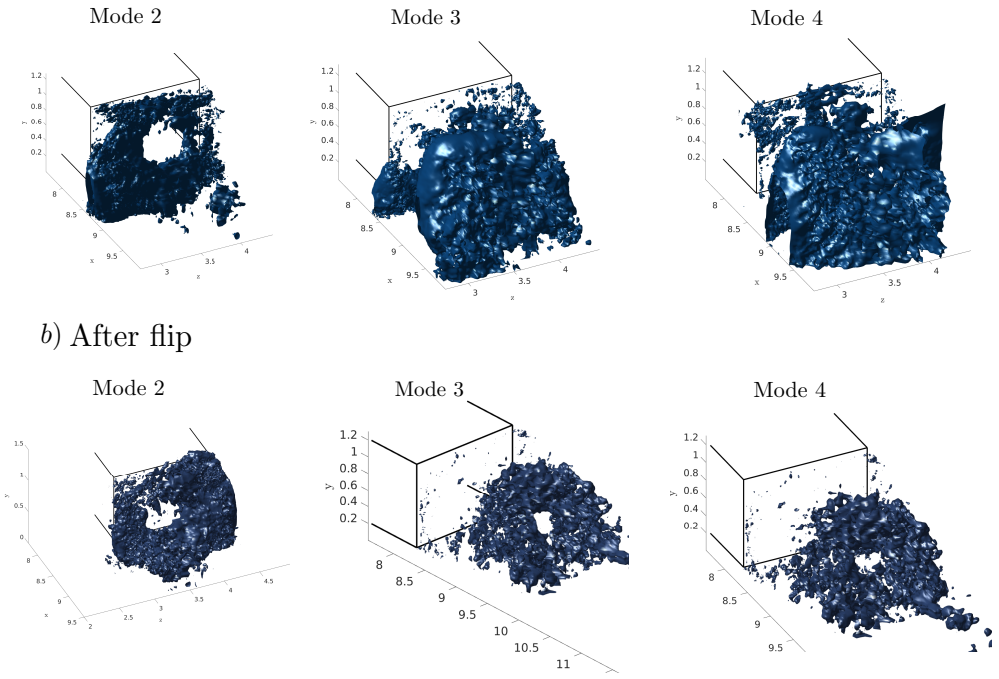


Figure 4.20: The next three POD modes were derived from two datasets: top - iso-contours of the POD modes when the wake on the left, bottom - iso-contours of the POD modes when wake on the right.

a more active shear layer due to the asymmetry of the wake, but it is not tilted. Mode 3 and 4 are also symmetric in the horizontal plane; only ground effects are affecting the structure. Overall, the $2nd$ - $4rd$ modes show the distribution of energy in the wake: most of the energy being concentrated near the base and some lower energy dynamics further downstream in the wake. The last few POD modes also pick up some shedding activity near the top edge of the base. Overall the POD modes reveal that the tilted asymmetric nature of the wake is present only in the first and most energetic mode. The remaining modes show different asymmetry: mode 2 reveals higher energy in one of the shear layers, while modes 3 and 4 appear more symmetric in horizontal direction, but asymmetric vertically, reflecting ground interacting with the wake.

4.3 Open Loop Forcing

In this section the Ahmed body flow at $Re = 25,000$ is actuated using open-loop harmonic forcing across forcing frequencies of $0.004 \leq St_f \leq 0.5$ at amplitudes $A_j = 0.1$. The range was selected based on the frequency spectrum of the base pressure force signal in figure 4.21. The unfiltered amplitude spectrum, computed using fft command in Matlab, captured well the broad spectrum dynamics at the lower frequencies. However, because the spectrum is so rich, it is hard to identify clear peaks. To better identify the key frequencies in the spectrum, the Matlab *pwelch* function was used to compute the Power Spectral density estimate using Welch method [114]. As a result, three main peaks can be observed in the power spectrum (red) in figure 4.21: at $St_H \approx 0.036$, $St_H \approx 0.061$ and $St_H \approx 0.082$. While the simulations presented here ran for long enough to observe the bi-stabile switch, the signal capture was, most likely, performed over too short a time to obtain discrete low frequency peaks in the spectrum. It is likely that given a longer signal the low-frequency peaks listed above, would converge to the bubble pumping frequency. There is also some spectral activity observed at $St_H \approx 0.182$ which most likely represents the shedding dynamics. The spectrum does not display significant dynamics past $St_H = 0.5$. The actuation shape is chosen to be the same as for low Reynolds number simulations, presented in section 3.3. The data from the open loop simulations can be used to build a low order model and design a feedback controller following the procedure described in section 2.3.

4.3.1 Effects of the Open-Loop Forcing

Due to the computational cost all open-loop forcing simulations were limited to 8 cycles of the forcing frequency after the transients disappear. This criterion ensured that the flow has sufficient time to respond to actuation and there is a reasonable number of occurrences of harmonic forcing to be able to draw conclusions from

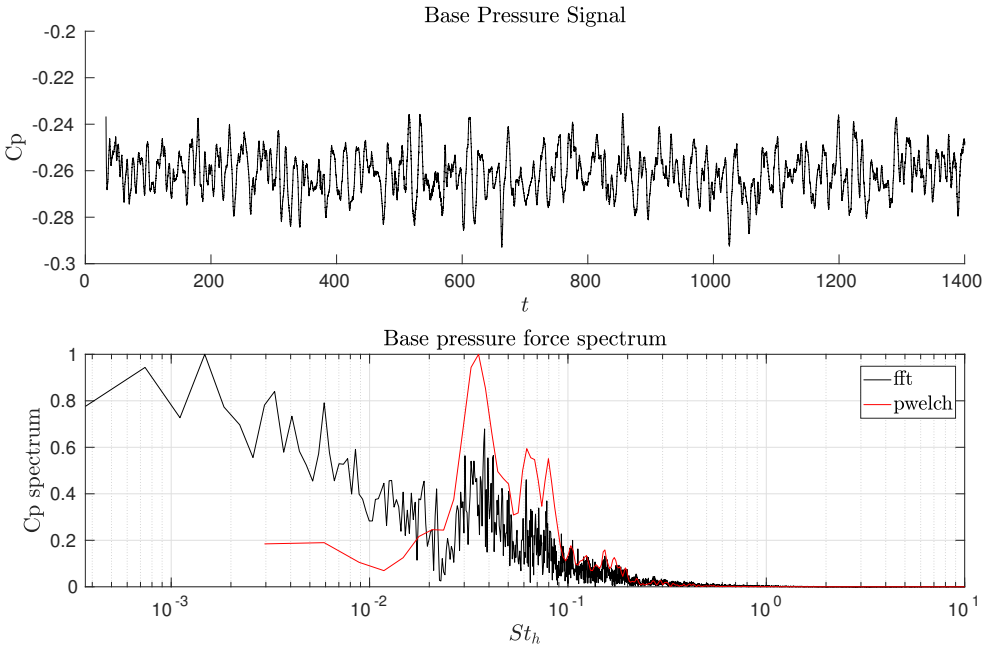


Figure 4.21: Base pressure force signal over the duration of the simulation (top) and the corresponding base pressure force spectrum (bottom). The base pressure force spectrum was computed using both fft (black) and $pwelch$ (red) Matlab commands show the rich wake dynamics at the low frequencies and extract the main peaks.

the response data. Another criterion was to ensure the spectrum captures the low frequencies observed in the unforced signal. First, the effects of the open-loop forcing are considered in figure 4.22 showing changes in the mean base pressure and rms of base pressure fluctuations about the mean when the flow is actuated at various frequencies and amplitude $A_j = 0.1$.

Overall no large changes can be observed in the base pressure force signal in response to open-loop forcing. There is an increase in the mean base pressure at the highest frequency of $St_f = 0.5$ suggesting that high-frequency forcing could be effective in reducing drag of Ahmed body. However, the observed increase in the mean base pressure could also be the result of insufficient grid resolution to fully capture the small-scale structures produced by high-frequency perturbations. Surprisingly, forcing at the low frequencies in the "lock-in" region (forcing at frequencies that would naturally be amplified by the flow) appears to have adverse effects on the

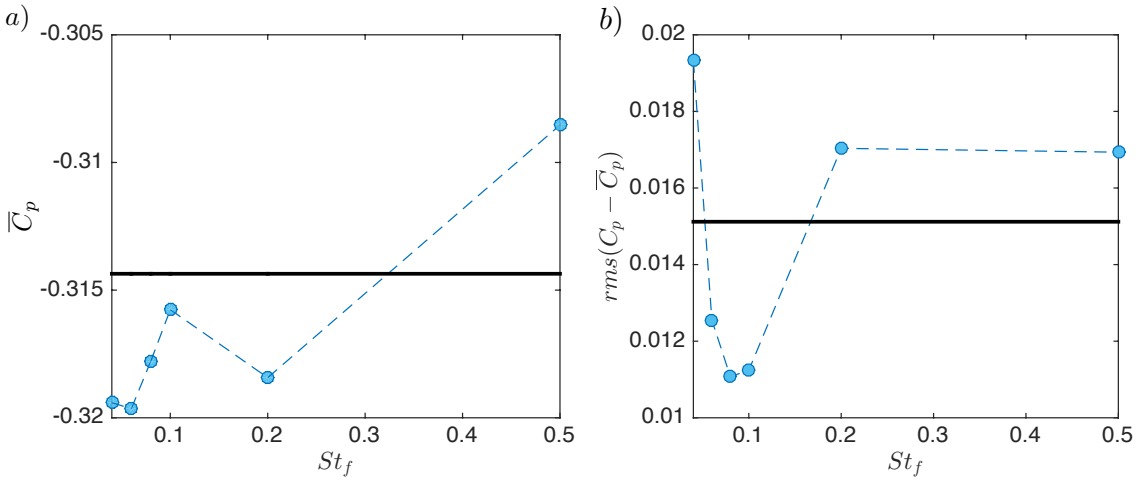


Figure 4.22: Changes in *a)* mean base pressure and *b)* root-mean square of fluctuations about the mean of base pressure signal in response to open-loop forcing at different frequencies and amplitude $A_j = 0.1$. The black line represents the value recorded in the unforced simulations and the blue and red dotted lines represent the values recorded in simulations with open-loop forcing.

base pressure: while for some frequencies the fluctuations are attenuated, the mean base pressure is decreased for the entire range from $0.04 \leq St_f \leq 0.2$.

It is useful to compare the response of the flow to open-loop forcing observed here with previous studies which performed a similar procedure to design and implement a sensitivity-based feedback control strategy to blunt bluff bodies. Figure 4.23 shows the results from open-loop forcing performed by *a)* Dahan et. al. [23] and *b)* Flinois [34]. Both authors used the data from open-loop simulations to design feedback controllers which attenuated base pressure fluctuations and achieved a base pressure recovery. Both studies were overviewed in detail in chapter 2 with actuation and sensing arrangements shown in figure 2.6. Both investigations employed synthetic jets for actuation and base pressure force signal for sensor measurements. In both cases forcing at the low frequencies near the lock-in range produced an increase in mean base pressure, while forcing near Kelvin-Helmholtz instability frequency of $St = 0.2$ appeared to excite the natural disturbances in the flow and affect the mean base pressure adversely . Most importantly, at low frequencies Dahan et. al. [23] report over 30% increase and Flinois [34] reports approximately 7% increase in mean

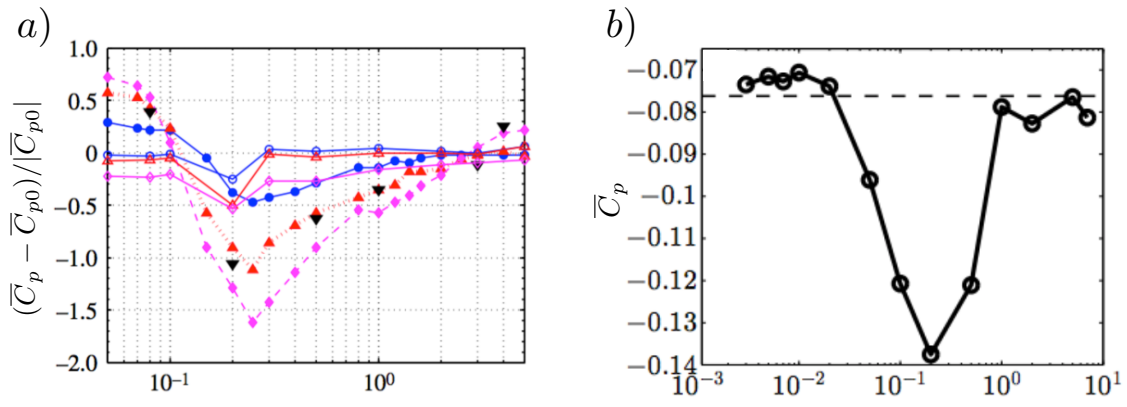


Figure 4.23: Changes in the mean base pressure in response to open-loop forcing via synthetic jets *a)* for a three-dimensional backward-facing step by Dahan et. al. [23] and *b)* for a three-dimensional backward-facing step with side walls by Flinois [34]. In *a)* the change in mean base pressure due to forcing along the separation line is shown for amplitudes $A_j = 0.1$ (●), $A_j = 2$ (▲) and $A_j = 0.3$ (◆) and due forcing at the base of the backward-facing step at amplitude $A_j = 0.2$ (▼). In *b)* the mean base pressure is shown at every forcing frequency compared to the mean value indicated by the dotted line.

base pressure in response to open-loop forcing, demonstrating that the selected actuation strategy has sufficient control authority to implement changes to the flow in the key frequency range. In contrast, in present work actuation at low frequencies yielded a decrease of $\approx 2\%$ in mean base pressure. Given that the usual trends in the response of the flow to open-loop forcing were not observed and forcing at the key frequencies did not achieve positive changes to the flow it is concluded that the current actuation shape is unlikely to yield good results in a feedback loop. Given the computational costs associated with performing linearity checks and feedback controller design, it has been decided not to proceed with feedback control implementation. We still believe the strategy holds promise, but its success depends on selecting a correct actuation and sensing arrangement to suit the dynamics of the flow. Therefore as part of future work, other sensing/actuation shapes need to be tested to design an effective sensitivity-based feedback controller.

4.4 Final Remarks

The results from Large Eddy Simulations of the Ahmed body flow with turbulent separation have been presented in this chapter. The bi-modal behaviour of the wake was captured and instantaneous structures analysed, revealing how asymmetry of the wake affects the wake topologies. The simulations also captured the presence of horseshoe vortices, shedding off from the toroidal wake. Using modal analysis, structures associated with specific wake frequencies and structures carrying the most energy are revealed. Open-loop forcing is performed with the view of collecting system identification data for feedback control design. However, upon consideration of the effects of the open-loop forcing on the flow, it is concluded that for the feedback controller to produce positive results other actuation/sensing arrangements need to be considered. A rigorous study of control/sensing arrangement could consider combinations of out-of-phase forcing, single edge forcing or anti-symmetric sensing to identify a configuration with most control authority.

Chapter 5

Conclusion

This thesis investigates numerically the flow past a simplified vehicle geometry known as the Ahmed body, focusing on capturing accurately the complex wake dynamics and the recently reported bi-modal behaviour and developing feedback control methods for form-drag reduction. The flow is studied at both laminar and turbulent Reynolds numbers, attempting to present a larger picture of how reflectional symmetry breaking in the wake manifests and develops.

At laminar numbers, Large Eddy Simulations are used to confirm a bifurcation sequence towards a reflectional symmetry breaking state, which previously has only been observed in experiments. The changes in the topology that accompany the bifurcation sequence are studied in further detail, revealing that as the reflectional symmetry of the wake is broken, the structure of the recirculation bubble changes from two recirculation regions positioned side by side, to one on top of the other. The vortex structure within the wake also moves from centred position to the side, affecting the position of the large recirculating vortices further downstream.

The reflectional symmetry breaking behaviour also persists to turbulent regime, where it manifests as slow bi-modal switching. In this work we obtained the first simulation of a turbulent blunt Ahmed body flow which captures bi-modal displacement of the wake from one asymmetric state to the other. While previous numerical

studies showed only one of the asymmetric states, present work captured both. Importantly, the simulations presented here resolve the wall boundary layer and have undergone a grid resolution study. They, therefore, could provide a springboard for both: future feedback control studies and more in-depth investigations into the Ahmed body dynamics.

The work presented in this thesis was the first to capture the switch numerically, the main difference with other simulations being resolution of the flow down to the wall. It thus makes a strong case, that for LES to capture the random bi-modal switching observed in the Ahmed body wake the simulations need to resolve the boundary layer. Further investigation is still necessary to establish if resolving the boundary layer (i.e. capturing the turbulent fluctuations believed to trigger the bi-modal switch) is indeed the deciding factor in whether or not the simulations capture bi-modality.

The instantaneous wake structures are analysed in detail, revealing how asymmetry affects the wake topologies. It is observed that instantaneously the wake is composed of a toroidal low pressure structure, which is distorted according to the asymmetric displacement of the wake. The simulations also revealed presence of horseshoe vortices, shedding off from the longest past of the toroidal wake. Modal analysis tools were also used to visualise *a)* the wake topologies by frequency using Dynamic Mode Decomposition (DMD) and *b)* the wake topologies by the energy content using Proper Orthogonal Decomposition (POD). The DMD modes revealed that the bubble pumping frequency originates from the motion of the low pressure vortex ring, as it moves towards and away from the body base. The DMD mode associated with the shedding frequency has the structure of the wake envelope, created by the shear layers shedding from the base sides and meeting downstream. The POD analysis revealed that the most energetic structures in the wake appear to be distorted according to the bi-modal displacement of the wake, while the less energetic structures appear to be symmetric.

A linear feedback control strategy, targeting attenuation of the base pressure force fluctuations, was developed and fully tested on the flow at laminar Reynolds number with a first set of investigations towards its implementation performed at turbulent Reynolds numbers. The control was implemented via body mounted sensors and unsteady synthetic jet actuation to ensure it is transferable to moving body experiments. At low Reynolds numbers the controller was quite successful, achieving attenuation of the base pressure force fluctuations, an increase in the mean base pressure, a drag reduction and re-symmetrisation of the wake. DMD analysis of the controlled and uncontrolled flows at $Re_H = 435$ revealed that the feedback controller slightly reduced the frequency of the shedding mode. Other effects of the controller included synching the shedding from the sides to become in-phase, elongating the recirculation region and severely weakening the large counter-rotating vortices observed far downstream in the unforced flow.

However, the first-stage investigations on the flow at higher Reynolds numbers, at which the flow exhibits turbulent separation, revealed that the actuation had little effect on the wake flow. Open-loop forcing performed across the range of main wake frequencies resulted in little change in the sensor signal with almost no favourable effects on the mean base pressure. Based on this, it is expected that a feedback controller with the chosen actuation and sensing arrangement would not have been able to reduce the mean drag. The computational and time resource required to conduct the necessary linearity checks and to implement the feedback controller went beyond that available. It is envisaged that the feedback control strategy requires a more rigorous investigation of actuation and sensing arrangements, something that will be performed in the future work.

5.1 Outlook

The present thesis demonstrates the complexity of the modern flow control problems, spanning many fields such as fluid dynamics, numerical methods, modelling, control theory, hydrodynamic stability theory and modal analysis. Leveraging all of these methods allows to successfully tackle real life problems and also opens up numerous avenues for future research.

As mentioned previously, a clear path for future research would be to benchmark new actuation and sensing arrangements for the linear feedback controller described in this work. It would also be interesting to see how the present control strategy would perform on more complex and representative geometries. These could incorporate elements such as moving ground, rotating wheels, underbody roughness or an air intake. Throughout this project, it became apparent how challenging and important grid generation is to capturing accurately the turbulent Ahmed body flow and bi-modal switching. Another element of future work, therefore, could be to compute the Ahmed body flow and the bi-modal switching using a different code able to handle unstructured grids. The present work could be used for validation, facilitating progressing to more complex and realistic geometries.

Other, more advanced controllers can also yield interesting results. For example, a multi-input multi-output controller could potentially be better suited to handle the bi-modal behaviour of the Ahmed body wake. Since the Ahmed body flow has some weak non-linearities, it can benefit from controllers which incorporate robust control and can account for nonlinearities in the response.

Another fundamental question, which is still outstanding, is what physical process drives the bi-modal switching of the wake. Investigation into the global modes and hydrodynamic stability properties of the unforced Ahmed body flow can aid the understanding of the physics behind bi-modality. The fact that the bi-modal switching in the Ahmed body wake has also been reported for real-life vehicles [15],

demonstrates how pertinent this behaviour is to our understanding of the ground vehicle flows and signifies it as another major research avenue.

Bibliography

[1] L. Agostini, E. Touber, and M. A. Leschziner. Spanwise oscillatory wall motion in channel flow: drag-reduction mechanisms inferred from DNS-predicted phase-wise property variations at $Re_\tau = 1000$. *Journal of Fluid Mechanics*, 743:606–635, 2014.

[2] S. R. Ahmed, G. Ramm, and G. Faltin. Some salient features of the time-averaged ground vehicle wake. *SAE Technical Paper*, (No. 840300), 1984.

[3] M.-R. Alam, W. Liu, and G. Haller. Closed-loop separation control: An analytic approach. *Physics of fluids*, 18(4):043601, 2006.

[4] M. Amitay, D. R. Smith, V. Kibens, D. E. Parekh, and A. Glezer. Aerodynamic flow control over an unconventional airfoil using synthetic jet actuators. *AIAA Journal*, 39(3):361–370, 2001.

[5] S. Bagheri. Koopman-mode decomposition of the cylinder wake. *Journal of Fluid Mechanics*, 726:596–623, 2013.

[6] D. Barros, J. Borée, B. R. Noack, A. Spohn, and T. Ruiz. Bluff body drag manipulation using pulsed jets and Coanda effect. *Journal of Fluid Mechanics*, 805:442–459, 2016.

[7] P. W. Bearman, D. De Beer, E. Hamidy, and J. K. Harvey. The effect of a moving floor on wind-tunnel simulation of road vehicles. In *SAE International Congress and Exposition*. SAE International, 1988.

[8] P.W. Bearman. Near wake flows behind two- and three-dimensional bluff bodies. *Journal of Wind Engineering and Industrial Aerodynamics*, 69:33 – 54, 1997. Proceedings of the 3rd International Colloqium on Bluff Body Aerodynamics and Applications.

[9] R. Becker, M. Garwon, C. Gutknecht, G. Bärwolff, and R. King. Robust control of separated shear flows in simulation and experiment. *Journal of Process Control*, 15(6):691–700, 2005.

[10] E. Berger, D. Scholz, and M. Schumm. Coherent vortex structures in the wake of a sphere and a circular disk at rest and under forced vibrations. *Journal of Fluids and Structures*, 4(3):231 – 257, 1990.

[11] G. Berkooz, P. Holmes, , and J. L. Lumley. The proper orthogonal decomposition in the analysis of turbulent flows. *Annual Review of Fluid Mechanics*, 25(1):539–575, 1993.

[12] R. D. Brackston, J. M. García de la Cruz, A. Wynn, G. Rigas, and J. F. Morrison. Stochastic modelling and feedback control of bistability in a turbulent bluff body wake. *Journal of Fluid Mechanics*, 802:726–749, 2016.

[13] Rowan D. Brackston, Andrew Wynn, and Jonathan F. Morrison. Extremum seeking to control the amplitude and frequency of a pulsed jet for bluff body drag reduction. *Experiments in Fluids*, 57(10):159.

[14] S. Cabitza. *Active control of the wake from a rectangular-sectioned body.* PhD thesis, Imperial College London, 2014.

[15] O. Cadot, A. Courbois, D. Ricot, T. Ruiz, F. Harambat, V. Herbert, R. Vigneron, and J. Délery. Characterisations of force and pressure fluctuations of real vehicles. *International Journal of Engineering Systems Modelling and Simulation*, 8(2):99–105, 2016.

[16] O. Cadot, A. Evrard, and L. Pastur. Imperfect supercritical bifurcation in a three-dimensional turbulent wake. *Physical Review E*, 91:063005, 2015.

[17] S. Camarri and A. Iollo. Feedback control of the vortex-shedding instability based on sensitivity analysis. *Physics of Fluids*, 22(9):094102, 2010.

[18] F. A. Chandra, G. Buzi, and J. C. Doyle. Glycolytic oscillations and limits on robust efficiency. *Science*, 333(6039):187–192, 2011.

[19] A. J. Chorin. The numerical solution of the Navier-Stokes equations for an incompressible fluid. *Bull. Amer. Math. Soc.*, 73(6):928–931, 11 1967.

[20] K. R. Cooper. Truck aerodynamics reborn - lessons from the past. In *International Truck & Bus Meeting & Exhibition*. SAE International, nov 2003.

[21] K. R. Cooper, T. Bertenyi, G. Dutil, J. Syms, and G. Sovran. The aerodynamic performance of automotive underbody diffusers. In *International Congress & Exposition*. SAE International, 1998.

[22] J. Dahan. *Linear feedback control for form-drag reduction on bluff bodies with a blunt trailing edge.* PhD thesis, Imperial College London, 2013.

[23] J. A. Dahan, A. S. Morgans, and S. Lardeau. Feedback control for form-drag reduction on a bluff body with a blunt trailing edge. *Journal of Fluid Mechanics*, 704:360–387, 2012.

[24] L. Dalla Longa, A. S Morgans, and J. A. Dahan. Reducing the pressure drag of a D-shaped bluff body using linear feedback control. *Theoretical and Computational Fluid Dynamics*, 2017.

[25] L. Dalla Longa, A. S. Morgans, and O. Evstafyeva. Numerical study of the bi-stable wake past a three-dimensional blunt bluff body. *Submitted to Journal of Fluid Mechanics*.

[26] J. Delville, L. Ukeiley, L. Cordier, J. P. Bonnet, and M. Glauser. Examination of large-scale structures in a turbulent plane mixing layer. Part 1. Proper orthogonal decomposition. *Journal of Fluid Mechanics*, 391:91–122, 1999.

[27] E. G. Duell and A. R. George. Measurements in the unsteady near wakes of ground vehicle bodies. In *International Congress & Exposition*. SAE International, 1993.

[28] E. G. Duell and A. R. George. Experimental study of a ground vehicle body unsteady near wake. In *International Congress & Exposition*. SAE International, 1999.

[29] H.-J. Emmelmann. Performance of cars and light vans. In W.-H. Hucho, editor, *Aerodynamics of Road Vehicles*, pages 83 – 105. Butterworth-Heinemann, 1987.

[30] A. Evrard, O. Cadot, V. Herbert, D. Ricot, R. Vigneron, and J. Délery. Fluid force and symmetry breaking modes of a 3D bluff body with a base cavity. *Journal of Fluids and Structures*, 61:99 – 114, 2016.

[31] O. Evstafyeva, A. S. Morgans, and L. Dalla Longa. Simulation and feedback control of the Ahmed body flow exhibiting symmetry breaking behaviour. *Journal of Fluid Mechanics*, 817, 2017.

[32] D. Fabre, F. Auguste, and J. Magnaudet. Bifurcations and symmetry breaking in the wake of axisymmetric bodies. *Physics of Fluids*, 20(5):051702, 2008.

[33] G.M. Fishpool and M.A. Leschziner. Stability bounds for explicit fractional-step schemes for the Navier–Stokes equations at high Reynolds number. *Computers & Fluids*, 38(6):1289 – 1298, 2009.

[34] T. L. B Flinois. *Modelling and linear feedback control of bluff body flows*. PhD thesis, Imperial College London, 2015.

[35] T. L. B. Flinois and A. S. Morgans. Feedback control of unstable flows: a direct modelling approach using the eigensystem realisation algorithm. *Journal of Fluid Mechanics*, 793.

[36] J. Freudenberg and D. Looze. Right half plane poles and zeros and design tradeoffs in feedback systems. *IEEE Transactions on Automatic Control*, 30(6):555–565, 1985.

[37] N. Gautier and J.-L. Aider. Control of the separated flow downstream of a backward-facing step using visual feedback. In *Proc. R. Soc. A*, volume 469, page 2013 0404. The Royal Society, 2013.

[38] V. Gentile, F. F. J. Schrijer, B. W. Van Oudheusden, and F. Scarano. Low-frequency behavior of the turbulent axisymmetric near-wake. *Physics of Fluids*, 28(6):065102, 2016.

[39] A. R. George and J. R. Callister. Aerodynamic noise of ground vehicles. In *SAE Technical Paper*. SAE International, 1991.

[40] P. Gilliéron and A. Kourta. Aerodynamic drag reduction by vertical splitter plates. *Experiments in Fluids*, 48(1):1–16, 2010.

[41] H. Götz. Commercial vehicles. In W.-H. Hucho, editor, *Aerodynamics of Road Vehicles*, pages 295 – 354. Butterworth-Heinemann, 1987.

[42] M. Grandemange. *Analysis and Control of Three-dimensional Turbulent Wakes: from Axisymmetric Bodies to Road Vehicles*. PhD thesis, l'ENSTA ParisTech, 2013.

[43] M. Grandemange, O. Cadot, A. Courbois, V. Herbert, D. Ricot, T. Ruiz, and R. Vigneron. A study of wake effects on the drag of the Ahmed's squareback model at the industrial scale. *Journal of Wind Engineering and Industrial Aerodynamics*, 145, 2015.

[44] M. Grandemange, O. Cadot, and M. Gohlke. Reflectional symmetry breaking of the separated flow over three-dimensional bluff bodies. *Physical Review E*, 86:035302R, 2012.

[45] M. Grandemange, M. Gohlke, and O. Cadot. Bi-stability in the turbulent wake past parallelepiped bodies with various aspect ratios and wall effects. *Physics of Fluids*, 25:095103, 2013.

[46] M. Grandemange, M. Gohlke, and O. Cadot. Turbulent wake past a three-dimensional blunt body. part 1. Global modes and bi-stability. *Journal of Fluid Mechanics*, 722:51–84, 2013.

[47] E. Guilmineau. Computational study of flow around a simplified car body. *Journal of Wind Engineering and Industrial Aerodynamics*, 96(6):1207–1217, 2008.

[48] T. Han. Computational analysis of three-dimensional turbulent flow around a bluff body in ground proximity. *AIAA Journal*, 27(9):1213–1219.

[49] L. Henning and R. King. Drag reduction by closed-loop control of a separated flow over a bluff body with a blunt trailing edge. In *Proceedings of the 44th IEEE Conference on Decision and Control*, pages 494–499, 2005.

[50] L. Henning and R. King. Robust multivariable closed-loop control of a turbulent backward-facing step flow. *Journal of aircraft*, 44(1):201–208, 2007.

[51] A. Hervé, D. Sipp, P. J. Schmid, and M. Samuelides. A physics-based approach to flow control using system identification. *Journal of Fluid Mechanics*, 702:26–58, 2012.

[52] P. Holmes, J. L. Lumley, G. Berkooz, and C. W. Rowley. *Turbulence, Coherent Structures, Dynamical Systems and Symmetry.*

[53] J. Howell and D. Hickman. The influence of ground simulation on the aerodynamics of a simple car model. In *SAE International Congress and Exposition*. SAE International, 1997.

[54] P. Huerre and P. A. Monkewitz. Local and global instabilities in spatially developing flows. *Annual Review of Fluid Mechanics*, 22(1):473–537, 1990.

[55] J. C. R. Hunt, A. Wray, and P. Moin. Eddies, stream, and convergence zones in turbulent flows. Technical report, Center for Turbulence Research Report, 1988.

[56] S. Jakirlić, R. Jester-Zücker, and C. Tropea. Proc. 9^{th} ERCOFTAC/IAHR/COST workshop on refined turbulence modelling. October 2001.

[57] J. Jiménez, S. Hoyas, M. P. Simens, and Y. Mizuno. Turbulent boundary layers and channels at moderate Reynolds numbers. *Journal of Fluid Mechanics*, 657:335, 2010.

[58] F. Juillet, P. J. Schmid, and P. Huerre. Control of amplifier flows using subspace identification techniques. *Journal of Fluid Mechanics*, 725:522–565, 2013.

[59] B. Khalighi, K.-H. Chen, and G. Iaccarino. Unsteady aerodynamic flow investigation around a simplified square-back road vehicle with drag reduction devices. *Journal of Fluids Engineering*, 134(6):061101–061101–16, 2012.

[60] A. Kolmogorov. The Local Structure of Turbulence in Incompressible Viscous Fluid for Very Large Reynolds Numbers. *Akademiia Nauk SSSR Doklady*, 30:301–305, 1941.

[61] B. O. Koopman. Hamiltonian systems and transformation in hilbert space. *Proceedings of the National Academy of Sciences*, 17(5):315–318, 1931.

[62] S. Krajnovic and L. Davidson. Numerical study of the flow around a bus-shaped body. *ASME Journal of Fluids Engineering*, 125:500–509, 2003.

[63] A. Lahaye, A. Leroy, and A. Kourta. Aerodynamic characterisation of a square back bluff body flow. *International Journal of Aerodynamics*, 4(1-2):43–60, 2014.

[64] R. Lardat and M. A. Leschziner. A Navier-Stokes solver for LES on parallel computers. Technical report, UMIST, Department of Mecanical Engineering, 1998.

[65] G. M. Le Good, J. P. Howell, M. A. Passmore, and K. P. Garry. On-road aerodynamic drag measurements compared with wind tunnel data. In *International Congress & Exposition*. SAE International, 1995.

[66] M. A. Leschziner and S. Lardeau. Simulation of slot and round synthetic jets in the context of boundary-layer separation control. *Philosophical Transactions of the Royal Society of London A: Mathematical, Physical and Engineering Sciences*, 369(1940):1495–1512, 2011.

[67] J. Li, Y. Xia, A. S. Morgans, and X. Han. Numerical prediction of combustion instability limit cycle oscillations for a combustor with a long flame. *Combustion and Flame*, 185(Supplement C):28 – 43, 2017.

[68] R. Li, D. Barros, J. Borée, O. Cadot, B. R. Noack, and L. Cordier. Feedback control of bimodal wake dynamics. *Experiments in Fluids*, 57(10):158, 2016.

[69] R. Littlewood and M. Passmore. The optimization of roof trailing edge geometry of a simple square-back. In *SAE 2010 World Congress & Exhibition*. SAE International, 2010.

[70] R. Littlewood, M. Passmore, and D. Wood. An investigation into the wake structure of square back vehicles and the effect of structure modification on

resultant vehicle forces. *SAE International Journal of Engines*, 4(2):2629–2637, 2011.

[71] R. P. Littlewood and M. A. Passmore. Aerodynamic drag reduction of a simplified squareback vehicle using steady blowing. *Experiments in fluids*, 53(2):519–529, 2012.

[72] L. Ljung, editor. *System Identification (2Nd Ed.): Theory for the User*. Prentice Hall PTR, Upper Saddle River, NJ, USA, 1999.

[73] J-E. W. Lombard, D. Moxey, S. J. Sherwin, J. F. A. Hoessler, S. Dhandapani, and M. J. Taylor. Implicit Large-Eddy Simulation of a wingtip vortex. *AIAA Journal*, 54(2):506–518, 2015.

[74] J.-M. Lucas, O. Cadot, V. Herbert, S. Parpais, and J. Délery. A numerical investigation of the asymmetric wake mode of a squareback Ahmed body – effect of a base cavity. *Journal of Fluid Mechanics*, 831:675–697, 2017.

[75] J. L. Lumley. The Structure of Inhomogeneous Turbulent Flows. In A. M. Yaglom and V. I. Tatarski, editors, *Atmospheric turbulence and radio propagation*, pages 166–178. Nauka, 1967.

[76] J. L. Lumley. *Stochastic Tools in Turbulence*. Academic Press New York, 1970.

[77] R. Manceau and J.-P. Bonnet. Proc. 10^{th} ERCOFTAC (SIG-15)/IAHR/QNET-CFD workshop on refined turbulence modelling. October 2002.

[78] F. Marrot, P. Gajan, S. Pauzin, and F. Simon. Experimental application of an active control loop on backward-facing step flow. *AIAA Journal*, 43(6):1176–1186, 2005.

[79] W. Mayer and G. D. Wickern. The new audi a6/a7 family - aerodynamic development of different body types on one platform. *SAE Int. J. Passeng. Cars – Mech. Syst.*, 4:197–206, 2011.

[80] P. Meliga, J. M. Chomaz, and D. Sipp. Global mode interaction and pattern selection in the wake of a disk: a weakly nonlinear expansion. *Journal of Fluid Mechanics*, 633:159–189, 2009.

[81] Igor Mezić. Spectral properties of dynamical systems, model reduction and decompositions. *Nonlinear Dynamics*, 41(1):309–325, 2005.

[82] M. Minguez, R. Pasquetti, and E. Serre. High-order large-eddy simulation of flow over the "Ahmed body" car model. *Physics of Fluids*, 20(9):095101–095101, September 2008.

[83] M. Miozzi and G. Querzoli. PTV and POD analysis of the instabilities in a quasi two-dimensional convective flow. *Applied Scientific Research*, 56(2):221–242, 1996.

[84] V. I. Mistry, G. J. Page, and J. J. McGuirk. Simulation of receptivity and induced transition from discrete roughness elements. *Flow, Turbulence and Combustion*, 95(2):301–334, Oct 2015.

[85] F. Nicoud and F. Ducros. Subgrid-scale stress modelling based on the square of the velocity gradient tensor. *Flow, Turbulence and Combustion*, 62(3):183–200, 1999.

[86] Office of National Statistics. Uk environmental accounts, 2017.

[87] Noack B. R. Östh, J. and, S. Krajnović, D. Barros, and Borée. J. On the need for a nonlinear subscale turbulence term in POD models as exemplified for a high-Reynolds-number flow over an Ahmed body. *Journal of Fluid Mechanics*, 747:518–544, 2014.

[88] A. R. Oxlade, J. F. Morrison, A. Qubain, and G. Rigas. High-frequency forcing of a turbulent axisymmetric wake. *Journal of Fluid Mechanics*, 770:305–318, 2015.

[89] Moin P., , and Mahesh K. Direct numerical simulation: A tool in turbulence research. *Annual Review of Fluid Mechanics*, 30(1):539–578, 1998.

[90] M. Pastoor, L. Henning, B. R. Noack, R. King, and G. Tadmor. Feedback shear layer control for bluff body drag reduction. *Journal of Fluid Mechanics*, 608:161–196, 2008.

[91] B. Patte-Rouland, G. Lalizel, J. Moreau, and E. Rouland. Flow analysis of an annular jet by particle image velocimetry and proper orthogonal decomposition. *Measurement Science and Technology*, 12(9):1404, 2001.

[92] A-K. Perry. *An investigation into the base pressure of simplified automotive squareback geometries.* PhD thesis, Loughborough University, 2016.

[93] A.-K. Perry, G. Pavia, and M. Passmore. Influence of short rear end tapers on the wake of a simplified square-back vehicle: wake topology and rear drag. *Experiments in Fluids*, 57(11):169, 2016.

[94] S.B. Pope. *Turbulent Flows*. Cambridge University Press, 2000.

[95] M. Provansal, C. Mathis, and L. Boyer. Bénard-von Kármán instability: transient and forced regimes. *Journal of Fluid Mechanics*, 182:1–22, 1987.

[96] Pasquetti R. and Peres N. A penalty model of synthetic micro-jet actuator with application to the control of wake flows. *Computers & Fluids*, 114(Supplement C):203 – 217, 2015.

[97] C. M. Rhie and W. L. Chow. Numerical study of the turbulent flow past an airfoil with trailing edge separation. *AIAA Journal*, 21(11):1525–1532, 1983.

[98] G. Rigas, A. S. Morgans, R. D. Brackston, and J. F. Morrison. Diffusive dynamics and stochastic models of turbulent axisymmetric wakes. *Journal of Fluid Mechanics*, 778:R2, 2015.

[99] G. Rigas, A. S. Morgans, and J. F. Morrison. Weakly nonlinear modelling of a forced turbulent axisymmetric wake. *Journal of Fluid Mechanics*, 814:570–591, 2017.

[100] G. Rigas, A. R. Oxlade, A. S. Morgans, and J. F. Morrison. Low-dimensional dynamics of turbulent axisymmetric wake. *Journal of Fluid Mechanics Rapids*, 755:R5, 2014.

[101] M. Rouméas, P. Gilliéron, and A. Kourta. Analysis and control of the near-wake flow over a square-back geometry. *Computers & Fluids*, 38(1):60 – 70, 2009.

[102] M. Sardou. "Reynolds effect" and "moving ground effect" tested in a quarter scale wind tunnel over a high speed moving belt. *Journal of Wind Engineering and Industrial Aerodynamics*, 22(2):245 – 270, 1986. Special Issue 6th Colloquium on Industrial Aerodynamics Vehicle Aerodynamics.

[103] H. Schlichting and K. Gersten. *Boundary-Layer Theory*. Springer Berlin Heidelberg, Berlin, Heidelberg, Germany, 2016.

[104] P. J. Schmid. Dynamic mode decomposition of numerical and experimental data. *Journal of Fluid Mechanics*, 656:5–28, 2010.

[105] L. Sirovich. Turbulence and the dynamics of coherent structures. I - Coherent structures. II - Symmetries and transformations. III - Dynamics and scaling. *Quarterly of Applied Mathematics*, 45:561–571, 1987.

[106] J. Smagorinsky. General circulation experiments with the primitive equations. *Monthly Weather Review*, 91(3):99–164, 1963.

[107] O. Stalnov, I. Fono, and A. Seifert. Closed-loop bluff-body wake stabilization via fluidic excitation. *Theoretical and Computational Fluid Dynamics*, 25(1):209–219, 2011.

[108] L. Temmerman. *Large Eddy Simulation of separating flows from curved surfaces.* PhD thesis, Queen Mary University of London, 2004.

[109] J. F. Thompson, B. K. Soni, and N. P. Weatherill. *Handbook of grid generation.* CRC press, 1998.

[110] Y. Utturkar, R. Mittal, P. Rampunggoon, and L. Cattafesta. *Sensitivity of synthetic jets to the design of the jet cavity.* American Institute of Aeronautics and Astronautics, 2002.

[111] G. Vinnicombe. Uncertainty and feedback: $\mathcal{H}_\infty$ loop-shaping and the ν-gap metric. 2001.

[112] R. Volpe, P. Devinant, and A. Kourta. Experimental characterization of the unsteady natural wake of the full-scale square back Ahmed body: flow bistability and spectral analysis. *Experiments in Fluids*, 56(5):99, 2015.

[113] E. Wassen, S. Eichinger, and F. Thiele. *Simulation of Active Drag Reduction for a Square-Back Vehicle*, pages 241–255. Springer Berlin Heidelberg, 2010.

[114] P. Welch. The use of fast Fourier transform for the estimation of power spectra: A method based on time averaging over short, modified periodograms. *IEEE Transactions on Audio and Electroacoustics*, 15(2):70–73, 1967.

[115] J. Weller, S. Camarri, and A. Iollo. Feedback control by low-order modelling of the laminar flow past a bluff body. *Journal of Fluid Mechanics*, 634:405–418, 2009.

[116] H. Werle. Simulation de l'effet due sol au tunnel hydrodynamique. Technical report, ONERA Report TP63, 1963.

[117] R.M. Wood. Impact of advanced aerodynamic technology on transportation energy consumption. *SAE Technical Paper*, (2004-01-1306), 2004.

[118] D. Zhao and A.S. Morgans. Tuned passive control of combustion instabilities using multiple Helmholtz resonators. *Journal of Sound and Vibration*, 320(4):744 – 757, 2009.

Appendix A

Linear Transfinite Interpolation

Linear transfinite interpolation allows to generate grid confirming to specified boundaries, making it the perfect tool to bridge the curved boundary of the O-grid and the rest of the domain. Overall is it a process of transforming a rectangular computational domain defined by a coordinate system (ξ, η, ζ) into a physical domain of (x, y, z) coordinates. The process starts by defining a mapping between the two domains as:

$$\chi(\xi, \eta, \zeta) = \begin{bmatrix} x(\xi, \eta, \zeta) \\ y(\xi, \eta, \zeta) \\ z(\xi, \eta, \zeta) \end{bmatrix}$$

where $0 \leq \xi \leq 1$, $0 \leq \eta \leq 1$ and $0 \leq \zeta \leq 1$. Based on this mapping the grid is interpolated from the physical boundaries with edges and corners defined a-priori. The univariate interpolations and tensor products are defined at:

$$\begin{aligned}
\mathbf{U}(\xi_I, \eta_J, \zeta_K) &= (1 - \xi_I)\mathbf{X}(0, \eta_J, \zeta_K) + \xi_I \mathbf{X}(1, \eta_J, \zeta_K) \\
\mathbf{V}(\xi_I, \eta_J, \zeta_K) &= (1 - \eta_J)\mathbf{X}(\xi_I, 0, \zeta_K) + \eta_J \mathbf{X}(\xi_I, 1, \zeta_K) \\
\mathbf{V}(\xi_I, \eta_J, \zeta_K) &= (1 - \zeta_K)\mathbf{X}(\xi_I, \eta_J, 0) + \zeta_K \mathbf{X}(\xi_I, \eta_J, 1) \\
\mathbf{UW}(\xi_I, \eta_J, \zeta_K) &= (1 - \xi_I)(1 - \zeta_K)\mathbf{X}(0, \eta_J, 0) + (1 - \xi_I\zeta_K)\mathbf{X}(0, \eta_J, 1) \\
&\quad + \xi_I(1 - \zeta_K)\mathbf{X}(1, \eta_J, 0) + \xi_I\zeta_K \mathbf{X}(1, \eta_J, 1)
\end{aligned} \tag{A.1}$$

$$
\begin{aligned}
\mathbf{UV}(\xi_I,\eta_J,\zeta_K) &= (1-\xi_I)(1-\eta_J)\mathbf{X}(0,0,\zeta_K) + (1-\xi_I)\eta_J\mathbf{X}(0,1,\zeta_K) \\
&\quad +\xi_I(1-\eta_J)\mathbf{X}(1,0,\zeta_K) + \xi_I\eta_J\mathbf{X}(1,1,\zeta_K) \\
\mathbf{VW}(\xi_I,\eta_J,\zeta_K) &= (1-\eta_J)(1-\zeta_K)(\xi_I,0,0) + (1-\eta_J)\zeta_K\mathbf{X}(\xi_I,1,0) \\
&\quad +\eta_J(1-\zeta_K)\mathbf{X}(\xi_I,0,1) + \eta_J\zeta_K\mathbf{X}(\xi_I,1,1) \\
\mathbf{UVW}(\xi_I,\eta_J,\zeta_K) &= (1-\xi_I)(1-\eta_J)(1-\zeta_K)\mathbf{X}(0,0,0) + (1-\xi_I)(1-\eta_J)\zeta_K\mathbf{X}(0,0,1) \\
&\quad +(1-\xi_I)\eta_J(1-\zeta_K)\mathbf{X}(0,1,0) + (1-\xi_I)\eta_J\zeta_K\mathbf{X}(0,1,1) \\
&\quad +\xi_I(1-\eta_J)(1-\zeta_K)\mathbf{X}(1,0,0) + \xi_I(1-\eta_J)\zeta_K\mathbf{X}(1,0,1) \\
&\quad +\xi_I\eta_J(1-\zeta_K)\mathbf{X}(1,1,0) + \xi_I\eta_J\zeta_K\mathbf{X}(1,1,1)
\end{aligned}
\tag{A.2}
$$

The equation for the transfinite grid is then

$$
\begin{aligned}
\mathbf{X}(\xi_I,\eta_J,\zeta_K) &= \mathbf{U}(\xi_I,\eta_J,\zeta_K) + \mathbf{V}(\xi_I,\eta_J,\zeta_K) + \mathbf{W}(\xi_I,\eta_J,\zeta_K) - \mathbf{UW}(\xi_I,\eta_J,\zeta_K) \\
&\quad -\mathbf{UV}(\xi_I,\eta_J,\zeta_K) - \mathbf{VW}(\xi_I,\eta_J,\zeta_K) + \mathbf{UVW}(\xi_I,\eta_J,\zeta_K)
\end{aligned}
\tag{A.3}
$$

This procedure is outlined in more detail in [109].